

**A Finite Element Segregated Method for Thermo-Chemical Equilibrium  
and Nonequilibrium Hypersonic Flows Using Adapted Grids**

**Djaffar Ait-Ali-Yahia**

**A Thesis  
in  
The Department  
of  
Mechanical Engineering**

**Presented in Partial Fulfillment of the Requirements  
for the Degree of Doctor of Philosophy at  
Concordia University  
Montréal, Québec, Canada**

**December 1996**

**© Djaffar Ait-Ali-Yahia, 1996**



National Library  
of Canada

Acquisitions and  
Bibliographic Services

395 Wellington Street  
Ottawa ON K1A 0N4  
Canada

Bibliothèque nationale  
du Canada

Acquisitions et  
services bibliographiques

395, rue Wellington  
Ottawa ON K1A 0N4  
Canada

Your file Votre référence

Our file Notre référence

The author has granted a non-exclusive licence allowing the National Library of Canada to reproduce, loan, distribute or sell copies of this thesis in microform, paper or electronic formats.

L'auteur a accordé une licence non exclusive permettant à la Bibliothèque nationale du Canada de reproduire, prêter, distribuer ou vendre des copies de cette thèse sous la forme de microfiche/film, de reproduction sur papier ou sur format électronique.

The author retains ownership of the copyright in this thesis. Neither the thesis nor substantial extracts from it may be printed or otherwise reproduced without the author's permission.

L'auteur conserve la propriété du droit d'auteur qui protège cette thèse. Ni la thèse ni des extraits substantiels de celle-ci ne doivent être imprimés ou autrement reproduits sans son autorisation.

0-612-25931-5

Canadá

# **Abstract**

## **A Finite Element Segregated Method for Hypersonic Thermo-Chemical Equilibrium and Nonequilibrium Flows Using Adapted Grids**

**Djaffar Ait-Ali-Yahia, Ph.D.**

**Concordia University, 1996**

This dissertation concerns the development of a loosely coupled, finite element method for the numerical simulation of 2-D hypersonic, thermo-chemical equilibrium and nonequilibrium flows, with an emphasis on resolving directional flow features, such as shocks, by an anisotropic mesh adaptation procedure. Since the flow field of such problems is chemically reacting and molecular species are vibrationally excited, numerical analyses based on an ideal gas assumption result in inaccurate if not erroneous solutions. Instead, hypersonic flows must be computed by solving the gasdynamic equations in conjunction with species transport and vibrational energy equations.

The number of species transport equations could be very high but is drastically reduced by neglecting the ionization, thus leaving one to represent the air by only five neutral species: O, N, NO, O<sub>2</sub> and N<sub>2</sub>. This system of equations is further simplified by considering an algebraic equation for conservation of the fixed nitrogen to oxygen ratio in air. The chemical source terms are computed according to kinetic models, with reaction rate coefficients given by Park's reaction models. All molecular species are characterized by a single vibrational temperature, yielding the well-known two-temperature thermal model which requires the solution of a single conservation equation for the total vibrational energy.

In this thesis, the governing equations are decoupled into three systems of PDEs – *gasdynamic*, *chemical* and *vibrational* systems– which are integrated by an implicit time-marching technique and discretized in space by a Galerkin-finite element method. This loosely-coupled formulation maintains the robustness of implicit techniques, while keeping the memory requirements to a manageable level. It also allows each system of PDEs to be integrated by the most appropriate algorithm to achieve the best global convergence. This particular feature makes a partially-decoupled formulation attractive for the extension of existing gasdynamic codes to hypersonic nonequilibrium flow problems, as well as for other applications having stiff source terms.

The hypersonic shocks are resolved in a cost-effective manner by coupling the flow solver to a directionally mesh adaptive scheme using an edge-based error estimate and an efficient mesh movement strategy. The accuracy of the numerical solution is continuously evaluated using a bound available from finite element theory. The Hessian (matrix of second derivatives) of a selected variable is numerically computed and then modified by taking the absolute value of its eigenvalues to finally produce a Riemannian metric. Using elementary differential geometry, the edge-based error estimate is thus defined as the length of the element edges in this Riemannian metric. This error is then equidistributed over the mesh edges by applying a mesh movement scheme made efficient by removing the usual constraints on grid orthogonality. The construction of an anisotropic mesh may thus be interpreted as seeking a uniform mesh in the defined metric.

The overall methodology is validated on various relevant benchmarks, ranging from supersonic frozen flows to hypersonic thermo-chemical nonequilibrium flows, and the results are compared against experimental data and, when not possible, to other computational approaches.

# Remerciements

Cette thèse est le fruit de 4 années de recherche dans le domaine des écoulements hypersoniques sous la direction du Professeur Wagdi G. Habashi (Fred pour les intimes). Je tiens à lui exprimer ma profonde gratitude et mes vifs remerciements pour ces précieux conseils qu'il m'a prodigué tout le long de la réalisation de cet ouvrage. Malgré ses nombreuses activités, scientifiques et administratives, il a toujours trouvé le temps de suivre l'évolution de mon travail et de me faire bénéficier de son expérience.

Je tiens aussi à remercier le Professeur R.W. MacCormack de l'Université de Stanford et les Professeurs F. Haghigat, G.H. Vatistas et R.A. Neemeh de l'Université de Concordia pour avoir accepté de critiquer ce travail et de faire partie de mon jury de thèse.

Je tiens à exprimer ma gratitude à tous ceux qui m'ont aidé dans mes travaux de recherche et en particulier au Professeur M. Fortin de l'Université Laval et au couple Dr. M.-G. Vallet et Dr. J. Dompierre pour m'avoir permis l'utilisation de la librairie d'optimisation des maillages LIBOM.

Je remercie également tous mes collègues du groupe CFD Laboratory avec qui j'ai eu des échanges fructueux sur la simulation numérique en mécanique des fluides. Ainsi, je voudrais remercier sincèrement Dr. Dutto, Dr. Guévremont (présentement chez P&WC), Dr. Baruzzi, Dr. Bourgault, Dr. Cronin, Tam (présentement chez P&WC), Ben Salah, Lepage, Stanescu, Aubé et Guillaume, qui ont rendu mon séjour agréable parmi eux et auxquels je souhaite une bonne continuation dans leur travaux de recherche.

Pour leur soutien financier, je remercie aussi CRSNG (Conseil de Recherche en Sciences Naturelles et en Génie) du Canada et FCAR (Fonds pour la Formation de Chercheurs et l'Aide à la Recherche) du Québec.

Enfin, je voudrais exprimer toute ma gratitude à mon épouse Sabrina dont le soutien moral a été essentiel durant la réalisation de cet ouvrage.

À mes parents Abdelkader et Dahbia,

À mon épouse Sabrina,

À mes frères et soeurs,

À toutes les personnes qui luttent pour la paix en Algérie.

# Contents

<b>List of Figures</b>	<b>xi</b>
<b>List of Tables</b>	<b>xv</b>
<b>Nomenclature</b>	<b>xvii</b>
<b>Chapter 1 Introduction</b>	<b>1</b>
1.1 Motivation . . . . .	1
1.2 High-Temperature Phenomena . . . . .	5
1.2.1 Thermal Nonequilibrium Gas . . . . .	5
1.2.2 Chemical Nonequilibrium Gas . . . . .	6
1.2.3 Chemical Models . . . . .	8
1.3 Low-Density Effects . . . . .	9
1.4 Review of Numerical Methods for Hypersonic Flows . . . . .	10
1.5 Grid Adaptation Methods . . . . .	15
1.5.1 Introduction . . . . .	15
1.5.2 Error Estimates . . . . .	17
1.5.3 Adaptive Strategies . . . . .	19

1.5.4	Optimal-Mesh Criterion . . . . .	23
1.6	Directionally-Adaptive Methods . . . . .	23
1.7	Objectives and Thesis Overview . . . . .	25
<b>Chapter 2</b>	<b>Numerical Discretization of Euler Equations for Divariant Gases</b>	<b>29</b>
2.1	Introduction . . . . .	29
2.2	Governing Equations . . . . .	31
2.3	Non-Dimensional Form . . . . .	32
2.4	Weak-Galerkin Formulation . . . . .	33
2.5	Temporal Discretization . . . . .	34
2.6	Derivation of Jacobian Matrices . . . . .	35
2.6.1	Exact Form . . . . .	35
2.6.2	Approximate Form . . . . .	37
2.7	Finite Element Space Discretization . . . . .	37
2.8	Artificial Dissipation . . . . .	39
2.9	Boundary Conditions . . . . .	42
<b>Chapter 3</b>	<b>Grid Adaptation</b>	<b>44</b>
3.1	Introduction . . . . .	44
3.2	Edge-Based Error Estimate . . . . .	45
3.3	Mesh Movement Scheme . . . . .	51
3.4	Numerical Results . . . . .	54
3.4.1	Analytical test case . . . . .	54

3.4.2	Hypersonic flow over a cylinder . . . . .	55
3.4.3	Supersonic compression corner . . . . .	57
3.4.4	Hypersonic flow over a double ellipse . . . . .	58
<b>Chapter 4</b>	<b>Governing Equations for Thermo- Chemical Nonequilibrium Flows</b>	<b>84</b>
4.1	Introduction . . . . .	84
4.2	Mass Conservation Equations . . . . .	85
4.3	Chemical Source Terms . . . . .	86
4.4	Conservation Equation of Species Vibrational Energy . . . . .	90
4.5	Vibrational Source Term . . . . .	92
4.6	Equation of State . . . . .	94
4.7	Total Internal Energy Expression . . . . .	94
4.8	Summary of the Governing Equations . . . . .	96
4.9	Simplification of the Governing Equations . . . . .	97
<b>Chapter 5</b>	<b>Numerical Simulation of Thermo- Chemical Nonequilibrium Flows</b>	<b>99</b>
5.1	Introduction . . . . .	99
5.2	Numerical Scheme . . . . .	100
5.3	Relaxation of Chemical Source Terms . . . . .	103
5.4	Solution Procedure . . . . .	104
5.5	Numerical Results . . . . .	106
5.5.1	Hypersonic Nitrogen Flow over a Cylinder . . . . .	106
5.5.2	Hypersonic Air Flow over a Cylinder . . . . .	109
5.5.3	Hypersonic Air Flow over a Double Ellipse . . . . .	110

<b>Chapter 6 Conclusions and Future Research</b>	<b>127</b>
6.1 Summary and Conclusions . . . . .	127
6.2 Future Research . . . . .	129
<b>Appendix A Chemical Models</b>	<b>132</b>
1.1 Park Reaction Model (1985) . . . . .	132
1.2 Park Reaction Model (1992) . . . . .	133
<b>Appendix B Jacobian Matrices for Chemical Nonequilibrium Flow Solver</b>	<b>136</b>
2.1 Jacobian Matrix of the Chemical Source Vector . . . . .	137
<b>Appendix C Jacobian Matrices for Thermo-Chemical Nonequilibrium Flow Solver</b>	<b>142</b>
3.1 Jacobian Matrix of the Chemical Source Vector . . . . .	143
3.2 Jacobian Matrix of the Vibrational Source Term . . . . .	145
3.2.1 Translational-Vibrational Exchange Contribution . . . . .	146
3.2.2 Chemical-Vibrational Exchange Contribution . . . . .	149
<b>Bibliography</b>	<b>152</b>

# List of Figures

1.1	Initial grid . . . . .	19
1.2	Adapted grid produced by an $r$ -method . . . . .	20
1.3	Adapted grid produced by an $h$ -method . . . . .	21
1.4	Adapted grid produced by a $p$ -method . . . . .	21
1.5	Adapted grid produced by a remeshing method . . . . .	22
2.1	Quadrilateral element in the global coordinates (left) and the corresponding master element in the natural coordinates (right). . . . .	39
2.2	Computational domain for a blunt-body problem . . . . .	43
3.1	Solution as approximated by a piecewise finite element method . . . . .	47
3.2	Transformation of a unit circle by $\mathbf{S}$ where $a =  \lambda_1 ^{-1/2}$ and $b =  \lambda_2 ^{-1/2}$ . . . . .	50
3.3	Spring analogy for a patch of elements . . . . .	52
3.4	Initial (a) and adapted (b) meshes and the corresponding iso-contours, (á) and (b), of $g$ . . . . .	61
3.5	Histogram of the error over the edges . . . . .	62
3.6	Node-displacement convergence history . . . . .	62

3.7	Maximum edge-error convergence history . . . . .	63
3.8	Definition of the Mach 6 flow over a half cylinder test case . . . . .	64
3.9	Adapted grids and the corresponding Mach number contours for cycles (a-c) . . . . .	65
3.10	Adapted grids and the corresponding Mach number contours for cycles (d-f) . . . . .	66
3.11	Enhancement of the Mach number distribution on the stagnation line with grid adaptation cycles . . . . .	67
3.12	Total enthalpy distributions for conservative and non-conservative artificial dissipations models. . . . .	67
3.13	Comparison of the present approach, on the stagnation line, to other numerical results . . . . .	68
3.14	Convergence history of the flow solver . . . . .	69
3.15	Convergence history of the adaptation procedure . . . . .	69
3.16	Comparison between adapted grids for error estimate based on variables: (1) density, (2) velocity, (3) Mach number . . . . .	70
3.17	Comparison between Mach number contours for error estimate based on variables: (1) density, (2) velocity, (3) Mach number . . . . .	71
3.18	Comparison between pressure contours for error estimate based on variables: (1) density, (2) velocity, (3) Mach number . . . . .	72
3.19	Definition of compression corner test case . . . . .	73
3.20	Adapted grids and the corresponding density contours for cycles (a-c) . . . . .	74
3.21	Adapted grids and the corresponding density contours for cycles (d-f) . . . . .	75
3.22	Pressure contours . . . . .	76

3.23	Mach number contours . . . . .	76
3.24	Magnification of the adapted grid in the shock region . . . . .	77
3.25	Distribution of the Mach number at $y = 0.5$ . . . . .	77
3.26	Convergence history of the flow solver . . . . .	78
3.27	Convergence history of the adaptation procedure . . . . .	78
3.28	Definition of Mach 8 flow over a double ellipse test case . . . . .	79
3.29	Adapted grids and the corresponding Mach number contours for cycles (a-c) . . . . .	80
3.30	Adapted grids and the corresponding Mach number contours for cycles (d-f) . . . . .	81
3.31	Enhancement of the $C_p$ distribution on the wall with grid adaptation cycles . . . . .	82
3.32	Convergence history of the flow solver . . . . .	82
3.33	Convergence history of the adaptation procedure . . . . .	83
5.1	Definition of a Mach 6 partially-dissociated nitrogen flow over a half cylinder test case. . . . .	113
5.2	Initial and final adapted grids with the corresponding Mach number contours. . . . .	114
5.3	Comparison between the interferogram of the flow field (top) and the computed density contours (bottom). . . . .	115
5.4	Enhancement of the Mach number distribution, along the stagnation line, with grid adaptation cycles. . . . .	115
5.5	Temperature distributions along the stagnation line (Ch. refers to chemical and Th. to thermal). . . . .	116
5.6	Species mass fraction distributions along the stagnation line. . . . .	116
5.7	Convergence history of the flow solver. . . . .	117

5.8 Convergence history of the mesh adaptation. . . . .	117
5.9 Definition of a Mach 12.7 air flow over a half-cylinder test case. . . . .	118
5.10 Initial and final adapted grid with the corresponding temperature contours. .	119
5.11 Temperature distributions along the stagnation line. . . . .	120
5.12 Species mass fraction distributions along the stagnation line. . . . .	120
5.13 Pressure coefficient distribution on the cylinder. . . . .	121
5.14 Convergence history of the flow solver. . . . .	121
5.15 Convergence history of the mesh adaptation. . . . .	122
5.16 Initial and final adapted grids with the corresponding temperature contours.	123
5.17 Monatomic oxygen mass-fraction contours. . . . .	124
5.18 Temperature distributions along the stagnation line. . . . .	124
5.19 Pressure coefficient on the body surface. . . . .	125
5.20 Convergence history of the flow solver. . . . .	125
5.21 Convergence history of the mesh adaptation. . . . .	126

# List of Tables

A.1	Arrhenius coefficients for forward rate coefficients. . . . .	133
A.2	Constants for computing equilibrium reaction constants . . . . .	133
A.3	Characteristic vibrational temperatures and heats of formation. . . . .	134
A.4	Arrhenius coefficients for forward rate coefficients. . . . .	134
A.5	Constants for computing equilibrium reaction constants . . . . .	134
A.6	Characteristic vibrational temperatures and heats of formation. . . . .	135

# Nomenclature

## Roman Symbols

$a$	Speed of sound
$A_{lr}$	Constants in equilibrium reaction coefficient
$A_{sr}$	Constant in Millikan and White's vibrational relaxation formula
$A_i$	Jacobian of the convection flux $\mathbf{F}_i$ with respect of $\mathbf{U}$
$B$	Jacobian of the source vector $\mathbf{S}$ with respect of $\mathbf{U}$
$c$	Mass fraction vector
$c_s$	Mass fraction of species $s$
$\tilde{c}_s$	Thermal speed of species $s$
$c_{vs}$	Translational-rotational specific heat at constant volume of species $s$
CFL	Courant-Friedrichs-Lowy number
$C_{rs}$	Rate constant for reaction $r$ and third body $s$ , $m^3/kmole\ sec$
$C_i$	Jacobian of the artificial dissipation vector $\mathbf{G}_i$ with respect of $\mathbf{U}$
$C_p$	Pressure coefficient
$D_a$	Damkhöhler number
$D_{ij}$	Jacobian of the artificial dissipation vector $\mathbf{G}_i$ with respect of $\mathbf{U}_j$

$e$	Total internal energy per unit mass of mixture, $J/kg$
$e_{vs}$	Vibrational energy per unit mass of species $s$ , $J/kg$
$e_{vs}^*$	Vibrational energy per unit mass of species $s$ at the local $T$
$\mathbf{F}_i$	Flux vector in the $i^{th}$ direction
$h$	Total enthalpy, $J/kg$
$h_e$	Element length
$h_s^\circ$	Heat of formation of species $s$ , $J/kg$
$H$	Hessian matrix
$L$	Jacobian of the conservative vector $\mathbf{Q}$ with respect of $\mathbf{U}$
$k$	Boltzmann constant = $1.38 \cdot 10^{26} m^2 kg/sec^2 K$
$k_{fr}$	Forward reaction rate coefficient
$k_{br}$	Backward reaction rate coefficient
$K_{eqr}$	Equilibrium constant of reaction $r$
$K$	Stiffness matrix
$M$	Mach number
$M$	Mass Matrix
$M_s$	Molecular weight of species $s$ , $kg/kmole$
$N$	Avogadro's number = $6.02 \cdot 10^{26} particles/kg\text{-mole}$
$n_i$	$i^{th}$ component of the outward unit normal to the surface
$N_s$	Number of chemical species
$N_r$	Number of chemical reactions

$N_2$	Diatomc Nitrogen
NO	Nitric oxide
$O_2$	Diatomc Oxygen
O	Atomic Oxygen
$p$	Pressure of mixture
$p_s$	Partial pressure of the species $s$
$Q$	Conservative variables
$R$	Residual vector
$\mathcal{R}$	Universal gas constant = $8.3144 \text{ kJ/kg-mole K}$
$R_s$	Gas constant of species $s$
$\bar{R}$	Mass-averaged gas constant
$S$	Source vector
$t$	Time, sec
$T$	Translational-Rotational temperature, $K$
$T_v$	Vibrational temperature, $K$
$T_a$	Rate controlling temperature, $K$
$x$	Cartesian coordinate vector
$Y_s$	Number density of species $s$ , $\text{kmole}/\text{m}^3$
$U$	Vector of primitive variables
$v$	Velocity vector
$W$	Finite element weight functions

## Greek Symbols

$\alpha$	Angle of attack, deg
$\gamma$	Ratio of specific heats
$\Gamma$	Boundary of the domain $\Omega$
$\delta_{ij}$	Kronecker symbol
$\Delta t$	Time step
$\Delta \mathbf{U}$	Iterative correction of the solution $\mathbf{U}$
$\theta_{vs}$	Vibrational characteristic temperature of species $s$
$\Lambda$	Diagonal matrix of eigenvalues of $\mathbf{H}$
$\Phi_I$	Shape function associated with node $I$
$\rho$	Density of mixture, $kg/m^3$
$\rho_s$	Density of species $s$ , $kg/m^3$
$\varepsilon$	Internal energy per unit mass, $J/kg$
$\epsilon$	Artificial dissipation coefficient
$\sigma_{sl}$	Collisional cross-section for species $s$ and $l$ , $m^2$
$\tau_s^{L-T}$	Vibrational relaxation time in Landau–Teller model, sec
$\tau_s^P$	Collision-limited vibrational relaxation time, sec
$\chi_l$	Molar concentration of species $s$
$\xi_s$	Average molecular speed of species $s$
$\omega$	Relaxation coefficient
$\Omega$	Computational domain

$\Sigma$  Summation symbol

$\Pi$  Product symbol

## Subscripts

$b$  Backward reaction

$e$  Element index

$f$  Forward reaction

$i, j$  Axes index of Cartesian coordinate system

$I, J$  Grid node indices

$r$  Reaction index

$s$  Species index ( $1 = \text{O}$ ,  $2 = \text{N}$ ,  $3 = \text{NO}$ ,  $4 = \text{O}_2$ ,  $5 = \text{N}_2$ )

$v$  Vibrational

,

Partial differentiation

$\infty$  Free-stream conditions

## Superscripts

$c$  Chemical

$g$  Gasdynamic

$L - T$  Landau-Teller model

$n$  Time level

$P$  Park model

$v$  Vibrational

\*     **Equilibrium state**

+     **Ion**

# Chapter 1

## Introduction

### 1.1 Motivation

In 1946, Tsien became the first researcher to introduce the words 'Hypersonic Flows' in a landmark paper titled: *Similarity Laws of Hypersonic Flows* [117]. Tsien clearly mentioned that a very high speed flow was being studied without specifically define the term, nor focus special attention to the fact that he was coining a new flow regime which contains some particular phenomena.

More than decade later, Hayes and Probstein described in their textbook [58] the existence of very high-speed flows, labeled *hypersonic flows*, which behave differently from supersonic flows. To justify the creation of this new category of flows, the authors stated:

*Within recent years, the development of aircraft and guided missiles has brought a number of new aerodynamic problems into prominence. Most of these problems arise because of extremely high flight velocities, and are characteristically different in some way from the problems which arise in supersonic flight. The term hypersonic is used to distinguish flow fields, phenomena, and problems appearing at flight speeds far greater than the speed of sound*

*from their counterparts appearing at flight speeds which are at most moderately supersonic. The appearance of new characteristic features in hypersonic flow fields justifies the use of a new term different from the well established term supersonic.*

Thus, the major reason for studying hypersonic flows independently of other supersonic flows is that at very high Mach numbers, a flow field is dominated by certain physical phenomena that do not exist, or are not as significant, at supersonic speeds.

The first interest in the study of hypersonic flow problems can be traced back to the 1950's and early 1960's, during the design of intercontinental ballistic missiles. After a period of inactivity in the 1970's, research in the field of hypersonic flows resumed to technically support the development of American space shuttles. This emergence was also supported by the need for advanced aerothermal design tools for the Hermes program in France [56], and both the AOTV (Aero-assisted Orbital Transfer Vehicle) [126, 127] and NASP (National Aero-Space Plane) [116, 129] in the USA. These design tools were mainly used for devising thermal protection, propulsion and control systems, but their development depends on accurate predictions of severe aerothermal loadings that the hypersonic vehicles experience during their flight and the reentry phase.

For typical hypersonic flows over blunt bodies, there is always a formation of a strong detached shock; the flow is compressed and then decelerated to subsonic speed in the nose region. The massive amount of kinetic energy that is stored in the free-stream flow is transformed, after the shock, into internal energy. Therefore, the flow field between the shock wave and the body, also called the *shock layer*, is dominated by high temperatures. The numerical simulation of such flows, using a calorically ideal gas assumption, usually yields extremely high temperature distributions in the shock layer. The measured temperature values are, however, much lower than the predicted results from a perfect gas model. This

inadequacy can be explained by hypersonic thermo-chemical nonequilibrium phenomena, whose theory represents a basis for the modeling of this type of flows.

Gas mixtures are principally composed of atoms and molecules. Each molecule is a collection of atoms bound together by rather complex intermolecular forces. According to statistical mechanics, these molecules have four modes of energy. The first mode is the translational energy resulting from the translation of the molecule center of mass. Secondly, a molecule can also rotate around its center of mass, and hence it has a rotational energy. The third mode results from the vibration of the atoms with respect to an equilibrium location within the molecule. The last mode, the so-called electronic energy, is due to the electrons' motion around the nucleus.

Results from quantum mechanics have shown that each of the above energies is quantified, i.e. the energies can only have certain discrete values. The total energy stored in a molecule is the sum of these four energies mentioned above, namely, translational, rotational, vibrational, and electronic energies. However, for a monatomic species, the vibrational mode does not exist, and the rotational mode can be excited by collisions only with difficulty, and hence is negligible.

As the temperature of a gas is increased above a certain value, the vibrational motion of molecules will become important, absorbing some of the energy which otherwise would go into the translational and rotational molecular motions. As the gas temperature is further increased, the molecules will begin to dissociate and even ionize. Under these conditions, the gas becomes vibrationally excited and chemically reacting. These physical effects are the major reasons that cause a high-temperature gas to deviate from calorically perfect gas behavior.

The thermo-chemical phenomena described above are termed *high-temperature effects*, but are frequently referred to in the literature as *real gas effects*. The major consequence of

real gas effects is a high heat transfer rate to the surface body. Thus, aerodynamic heating largely dominates the design of all hypersonic systems, be it that of a flight vehicle or of a hypersonic wind tunnel.

The design of hypersonic vehicles must therefore call upon theoretical, experimental and numerical tools. Traditionally, the wind tunnel has been the principal tool for design advancement, with shapes selected, tested and then optimized through careful analysis of measured data and flow visualization results. However, wind tunnel experiments are expensive, time consuming and may not be possible at very high Mach numbers. In addition, experimental studies are still limited due to the difficulty of reproducing high atmospheric equilibrium conditions in ground-based test facilities. In fact, hypersonic wind tunnel working flows are usually produced by a rapid expansion through a divergent duct which serves as an accelerator device. Therefore, the resulting gas flows are in a highly thermo-chemical nonequilibrium state with non-uniform velocity profiles due to the development of a boundary layer on the duct walls.

This situation has led to an increasing interest in the development of Computational Fluid Dynamics (CFD) codes (“*numerical wind tunnels*”) for predicting aero-thermal loads over hypersonic vehicles. This is made feasible by the constant advances in computer hardware and algorithms which make the use of more realistic mathematical models possible. Among the approximations that were made in the modeling of hypersonic flows, a lot of them are no longer justified or necessary in the era of supercomputing. A more comprehensive analysis of many physical aspects of the flow are now within reach of researchers, permitting substantial improvements in the prediction of high-temperature effects.

## 1.2 High-Temperature Phenomena

### 1.2.1 Thermal Nonequilibrium Gas

All rotational and vibrational excitation processes take place by molecular collisions and/or radiative interactions, but the present work is restricted to molecular collisions. In *equilibrium systems*, the gas is assumed to have sufficient time for the necessary collisions to occur, and the properties of the system at a fixed pressure and temperature are assumed constant, independent of time. However, there are many situations in high-speed flows where the gas may not be given the required time to reach an equilibrium state. A typical example is hypersonic flow across a shock wave.

When a fluid element passes through a shock front, its thermal equilibrium properties will change. The fluid element starts to seek its new equilibrium properties, but this requires the occurrence of molecular collisions, and hence time. By the time a sufficient number of collisions have taken place and equilibrium properties are approached, the fluid element would have moved a certain distance downstream of the shock front. Thus, there is a certain region immediately behind the shock wave where *thermal nonequilibrium* conditions prevail.

The temperature characterizing the rotational population distribution of molecular species  $s$  during this nonequilibrium transient period can be identified as the *rotational temperature*,  $T_{rs}$ . Experimental data [103] reveal that rotational relaxation occurs very rapidly for heavy molecules and since rotational constants differ only slightly among the three neutral molecules of air ( $\text{NO}$ ,  $\text{O}_2$ ,  $\text{N}_2$ ), one expects their rotational relaxation to take place almost equally as fast. The rotational excitation process of all species may be, therefore, accurately modeled by a single rotational temperature,  $T_r$ . In addition, rotational equilibration requires approximately the same number of collisions as translational equilibration, permitting the rotational and translational relaxations to occur simultaneously. It is

therefore common to assume that these two modes are in equilibrium at the translational-rotational temperature  $T$ .

In contrast to the rotational mode, the vibrational relaxation of air species is usually characterized by multiple vibrational temperatures,  $T_{vs}$ , resulting in what is referred to as a *multi-temperature model*. This is mainly due to significant differences in excitation rates of the three neutral molecules. Indeed, the rates for NO are faster than those of O<sub>2</sub> by several orders of magnitude, while those of N<sub>2</sub> are several orders of magnitude slower than those of O<sub>2</sub>.

A multi-temperature model requires the solution of a vibration energy equation for each molecular species, yielding a prohibitively large system of partial differential equations (PDEs) for a gas mixture with high number of molecular species. Although this model has been adopted in numerous studies [22, 56, 72], the large uncertainty in the modeling of chemistry-vibration coupling [73] often eclipses the advantages of this more complete model.

For temperatures above 3000 K, coupling among the vibrational modes of the molecular species are strong forcing the vibrational temperatures of the three neutral molecules to be nearly identical. In such a simpler *two-temperature model* [101, 102], the vibrational relaxation of all species may be characterized by a single vibrational temperature,  $T_v$ . This model is widely used in the numerical simulation of thermo-chemical nonequilibrium flows [2, 3, 8, 38, 104] since it only requires the solution of a single PDE for the total vibrational energy.

### 1.2.2 Chemical Nonequilibrium Gas

Many reacting flow problems may be adequately approximated by assuming an *equilibrium* real gas model. In this case, all time scales of chemical reactions are assumed to be small enough relative to the fluid motion time scale, so that the gas everywhere is in local

chemical equilibrium. At this state, both thermal and chemical properties of the gas can be completely defined by two thermodynamic variables such as temperature and pressure. This assumption (chemical equilibrium) is usually used in the simulation of low altitude flow problems.

At the other extreme, reactions can be so slow that the gas can be considered *frozen* in a particular chemical state. In this regime, the time scale of chemical reactions is quite large compared to the fluid dynamic time scale. Such a flow typically occurs in regions of rapid expansion such as jets or base regions of hypersonic bodies and is usually modeled by a perfect gas.

Finally, when the chemical time scale is of the same order as the fluid dynamic time scale, finite rate chemical (*chemical nonequilibrium*) processes must be considered. This is accomplished by adding species transport equations to the governing equations where the source terms represent the species rate of production/destruction.

The rate at which equilibration occurs is essentially dependent on the free-stream density and speed, or altitude and Mach number. The degree of chemical nonequilibrium is usually quantified by a dimensionless parameter known as the Damköhler number, that is

$$Da = \frac{\mathcal{L}S^c}{\rho_\infty V_\infty}, \quad (1.1)$$

where  $S^c$  is the production rate due to chemical reactions,  $V_\infty$  is the free-stream velocity, and  $\mathcal{L}$  is a geometrical length scale. It should be noted that a different Damköhler number may be derived for the vibrational relaxation of each molecular species.

The Damköhler number is defined as the ratio of the chemical reaction rate to the fluid motion rate,  $Da = \frac{S^c}{(\rho_\infty V_\infty / \mathcal{L})}$ , or the ratio of the fluid dynamic to the chemical reaction time scales,  $Da = \frac{\mathcal{L}/V_\infty}{\rho_\infty / S^c}$ . In the case of chemical equilibrium, the chemical rates are infinitely fast, and hence  $Da$  tends to infinity. At the other extreme, when  $Da$  tends to zero,

chemical reactions are very slow and frozen flow becomes the appropriate assumption. For conditions between these two limits, the flow is, to a proportional degree, in chemical nonequilibrium.

### 1.2.3 Chemical Models

At high temperatures, chemical reactions occur in a gas flow resulting in changes of each chemical species concentration. The modeling of this mass transfer process depends strongly on the selected chemical species as well as chemical reactions [11]. Indeed, a chemical model with a few species may lead to inaccurate results if a neglected species acts as a catalyst element which enhances certain chemical reactions. On the other hand, a chemical model with a large number of species complicates the mathematical model and requires a large computing time.

For air reacting flows which involve only dissociation phenomena, it is common to consider only atomic nitrogen N, atomic oxygen O, nitrogen monoxide NO, diatomic nitrogen N<sub>2</sub> and diatomic oxygen O<sub>2</sub>, while neglecting argon, carbon dioxide and water-vapor. This five species model is valid for temperatures below 9000 K and has been also used by Park *et al.* [105] for the calculation of real-gas effects on blunt-body trim angles in a suborbital flight-speed range. This choice is justified by the fact that the maximum molar concentration of NO<sup>+</sup> so produced is below 0.1, and consequently it has a minor effect on the chemical reaction rates. For this type of studies, *dissociation* and *shuffle* reactions are usually considered.

As the flow velocity increases, the ionization process becomes more important. For reentry problems up to 6000 m/s, the nitrogen monoxide produces the major part of electrons and, the ionized nitrogen monoxide and the electron (NO<sup>+</sup>, e<sup>-</sup>) should thus be added to the above species set. For flow velocities larger than 9000 m/s, the ionization is mainly due to atomic nitrogen and oxygen. Moreover, the molecular nitrogen ion, N<sub>2</sub><sup>+</sup>, is involved

in extremely fast reactions and must be taken into account, even at very low concentrations.

A more sophisticated model can then be constructed by considering all the single charged ions corresponding to the dissociation model, to arrive at an eleven species model ( $O$ ,  $N$ ,  $NO$ ,  $O_2$ ,  $N_2$ ,  $O^+$ ,  $N^+$ ,  $NO^+$ ,  $O_2^+$ ,  $N_2^+$ ,  $e^-$ ). In this chemical model, the reaction set for the dissociation phenomenon should be completed by charge exchange and associative ionization reactions.

### 1.3 Low-Density Effects

Most aerodynamic problems are properly addressed by assuming a continuous medium. There are however certain hypersonic applications which involve densities low enough that the continuum assumption breaks down. For altitudes above 92 km, flow in the nose region of the Space Shuttle cannot be properly treated by purely continuum assumptions [88]. As the Space Shuttle flies above this altitude, the standard no-slip conditions at the wall, i.e. zero velocity at the wall and continuity of the temperature at the gas-wall interface, no longer holds. These boundary conditions should be replaced by slip effects, in which velocity and temperature jumps should be assumed at the wall.

With increasing altitude, there will be a certain limit beyond which the continuum flow equations themselves are no longer valid, and kinetic theory should be used in the flow analysis. The air density can be low enough that the mean free path of molecules,  $\lambda$ , can become as large as the scale of the body itself and the probability of collisions between molecules is extremely weak. This regime is termed free molecular flow.

The similarity parameter that governs these different regimes is the Knudsen number. This parameter is defined as  $Kn = \lambda/L$ , where  $L$  represents a geometrical length scale of the body. The continuum Euler and Navier-Stokes (N-S) equations hold in the region limited by  $Kn < 0.2$ . However, slip effects should be included in the N-S equations when  $Kn > 0.03$ . Free molecular flow begins around a value of  $Kn = 1.0$  and the transitional

regime is thus essentially contained within  $0.03 < Kn < 1.0$ .

It should be noted that low-density effects should be not considered as a consequence of high-temperature effects, but rather as high-altitude effects. However, they are introduced in this chapter since some classes of hypersonic vehicles fly at, or through, the outer regions of the atmosphere, and therefore may experience such high-altitude effects.

## 1.4 Review of Numerical Methods for Hypersonic Flows

The history of modern numerical methods for hypersonic flows with a complete modeling of thermo-chemical nonequilibrium phenomena goes only back to the late 1980's, with the first adapted version of the Steger and Warming scheme by Candler and MacCormack [23]. Since that time, a very large number of classical schemes [67, 111, 114, 120], which were primarily designed for frozen flows of perfect gases, have been extended to include high-temperature effects.

These achievements were made through several steps of physical modeling advancements. Chemical equilibrium flows [27, 31, 43, 51, 123] were first tackled by including additional procedures for the calculation of species concentration. With the emergence of supercomputers, approximations in the physical modeling were gradually eliminated leading to the numerical simulation of chemical nonequilibrium flows [19, 30, 37, 124] by solving the gasdynamic equations (Euler or Navier-Stokes) in conjunction with species transport equations.

CFD schemes are principally distinct in their manner of *spatially discretizing* the inviscid fluxes which represent the convective terms of the governing equations. They may be classified into two major types of spatial discretizations: *central* and *upwind* differencing methods.

Central differencing methods are based on purely mathematical concepts (Taylor expansions), while the upwind differencing methods utilize information on signal propagations

provided by the theory of characteristics. Although other information, such as the local direction of the flow in the finite-element Streamline Upwinding Petrov-Galerkin (SUPG) method [61] could be used in the differencing, all upwind schemes have at least one feature in common and that is to include some physical flow information in the spatial discretization operation.

Until the early 1980's, most work in computational fluid dynamics on the Euler equations involved central differencing of the inviscid fluxes and dissipation operators to damp numerical oscillations. Some early Euler solutions were obtained by Magnus and Yoshihara [85] and Grossman and Moretti [50]. In 1981, Jameson *et al.* [67] introduced a four step Runge-Kutta solver using a finite-volume formulation. The artificial dissipation was constructed as a blend of second and fourth order differences of the conservative variables. The first dissipation operator acts as a high frequency damping term and prevents odd-even point decoupling, while the second operator is used as a shock capturing term, necessary to suppress numerical oscillations produced by shock waves. The convergence of this solver was greatly enhanced, first by Ni [90] and later by Jameson [64], by introducing a multi-grid acceleration technique, leading to a very efficient inviscid flow solver.

Although, this solver gained a lot of confidence among the CFD community and it is widely used in the aeronautic industry, the extension of this scheme to hypersonic reacting flows has only been made by few authors [104, 113]. One reason given by Yoon and Kwak [130] is that the classical Jameson scheme becomes unstable for hypersonic flow problems and a flux limited dissipation model should be introduced to overcome this drawback.

In the early 1980's, *characteristics-based* schemes for the Euler equations became prevalent. This covers the flux-vector splitting methods and the flux-difference splitting methods which are also known as Godunov-type schemes. In contrast to central differencings which damp numerical oscillations by adding artificial dissipation terms, upwind

schemes introduce essential physical properties of the governing equations in the spatial discretization, preventing the occurrence of such oscillations [59].

In 1981, Steger and Warming [114] introduced the first flux-vector splitting scheme which is based on the sign of the Jacobian eigenvalues. Physically, these eigenvalues represent both the speed and direction of propagation of a perturbation. This scheme uses the homogeneous feature of the inviscid fluxes to split each one of them into two components that are upwinded according to the sign of the associated propagation speeds.

One version of this scheme was extended by MacCormack and his co-workers to the computation of weakly ionized [20] and low density [49] hypersonic flows in thermo-chemical nonequilibrium. In the MacCormack method, originally developed for the Navier-Stokes equations [84], less dissipation is introduced in smooth regions by evaluating the upwind and downwind Jacobian matrices at the same point, while the original Steger and Warming scheme is used in strong pressure gradient regions. Such a method yields better boundary layer predictions and maintains numerical stability near physical discontinuities. This method was recently applied by Zeitoun *et al.* [131] for investigating the vibration-dissociation coupling in hypersonic thermo-chemical nonequilibrium flows.

The Steger and Warming splitting, however, gives rise to fluxes that are not continuously differentiable at sonic points in the flow causing the occurrence of a discontinuity in the slope of a computed solution at a sonic' point. In 1982, Van Leer [120] removed this drawback by imposing the split fluxes to be continuous functions of Mach number and expressed as polynomials of the lowest order possible.

This improved flux-vector splitting was extended to hypersonic chemical nonequilibrium by the group of Désideri [30, 31, 44] at INRIA, France. Their work consists of solving the 2-D Euler equations augmented by chemical species equations in a decoupled manner over structured and unstructured meshes. This scheme was further extended by Gross-

man and co-workers [25, 26, 128] to include thermal nonequilibrium effects in 3-D hypersonic flows. Recently, the Van Leer flux-splitting was also used by Edwards [39] and by Drouin *et al.* [33], where the second order accuracy in space is achieved by a Monotonic Upwind Scheme of Conservation Laws (MUSCL) algorithm.

Introducing more physical properties into upwind schemes can be achieved through the pioneering work of Godunov [48]. In Godunov's method, the solution is considered piecewise constant over each mesh cell and the evolution of the flow to the next time step results from the solution of a local, exact Riemann (shock tube) problem at each cell interface. Since this scheme required the resolution of a nonlinear algebraic equation at each time step, which can be quite time consuming, Roe [110] developed an approximate Riemann solver by linearizing the Riemann problem. This scheme has become quite popular due to its shock capturing capability and has been first extended to real gas flows in equilibrium [43, 51], and then to hypersonic nonequilibrium flows, by numerous authors [26, 34, 38, 46, 69, 128].

Overall, hypersonic reacting flow prediction procedures have almost been exclusively based on finite difference methods (FDMs) or finite volume methods (FVMs). In fact, all the schemes cited above were developed in the context of finite difference or finite volume formulations. Finite element methods (FEMs), however, have the ability to accurately represent complex domains and offer a strong mathematical basis for the development of a wide variety of error estimates [15, 96]. They also provide a natural and unique environment for implementing advanced adaptive strategies such as  $h\text{-}p$  methods [29, 109]. In addition, they have been successfully used for Euler and Navier-Stokes solutions [61, 81, 106, 118].

Similarly to other numerical formulations, research in the application of FEMs to CFD problems leads to a wide variety of methods which differ essentially through their stabilization techniques. Among the most used finite element formulations we can cite:

- Galerkin formulation [17, 82, 118] results in central differencing form that is usually stabilized by adding Laplacian operators of flow variables to the governing equations.
- SUPG formulation [18, 61, 62] produces an upwind effect by adding a perturbation term, that depends on the numerical solution, to the standard Galerkin test functions.
- Least-squares formulation [40, 68, 77] contains inherent dissipative terms and leads to symmetric and positive-definite matrices.

Most numerical solutions for hypersonic reacting flows are computed by marching the unsteady governing equations in pseudo-time until a steady state is reached. The use of time-dependent equations for steady-state computations is mainly driven by the fact that the initial-boundary value problem remains hyperbolic or parabolic in the time-space plane, independently from the flow regime (Mach number). This feature makes an appropriate numerical solution valid for a broad range of applications.

Basically, the steady-state solution of unsteady governing equations may be achieved by the two principal time-marching techniques: *explicit* and *implicit*.

The most used explicit techniques include Forward Euler and multi-step Runge-Kutta schemes. In the mid 80's, these time-marching approaches were quite popular in the field of nonequilibrium hypersonic flows, due to their moderate demands on computer resources. In addition, these techniques decouple the governing equations at each node/cell mesh and therefore led to highly vectorizable and parallelizable algorithms. For steady-state applications, however, the stiffness of the chemical source terms may limit the permissible time step to very small values, resulting in large computational times.

Bussing and Murman [19] have improved this numerical stability limitation by treating the chemical source terms in an *implicit* manner, and the convective terms by an explicit scheme. It has been shown that this has the effect of rescaling the governing equations

in time such that all gasdynamic and chemical phenomena evolve at comparable pseudo-time scales. This formulation leads to a *point-implicit* scheme where block matrices must be inverted at each point. Later, Eberhardt and Imlay [38] eliminate the matrix inversion operation by replacing the chemical Jacobian matrix by an approximate diagonal form which results from taking the  $L_2$ -norm of the Jacobian coefficients along each row.

Among modern alternatives, *implicit* methods have achieved significant success due to their robustness [22, 69, 104, 128]. In these types of schemes, the gasdynamic, species transport and vibrational energy equations are assembled over the domain or part of it and solved in a coupled fashion. For typical hypersonic reacting problems, such a formulation allows a much larger time-step than an explicit technique, but usually results in a larger system of equations that is more demanding in terms of memory.

## 1.5 Grid Adaptation Methods

### 1.5.1 Introduction

The field of CFD has seen many milestones achieved since it was first introduced by Von Neumann. From a specialty niche, it has inched its way into the design process to finally flourish as an independent science that has become well embedded in the modeling of a vast number of processes as a major design tool. Convinced by the potential of CFD, aerospace companies have played a major role in stimulating the emergence of commercial codes, believing that they could ultimately be used in a black-box manner.

Code developers, by necessity, have first to address the production of bug-free codes, while other sources of inaccuracy were left in. Such software do not provide any user error-control tools, but rather let him rely only on his experience. If one considers the arbitrariness of most generated meshes (e.g. grid size, mesh distribution, ...), the number of tuning parameters (e.g. artificial dissipation coefficients, relaxation factors, time step,

...) and the various hidden assumptions of mathematical modeling, it is no surprising that “similar” codes may yield different answers and that even different users of the the same code may get slightly different solutions.

Analyzing the role of the CFD in a design process, Habashi [55] stated during the World User Association in Applied CFD meeting (1996) that;

*... before CFD can be more widely accepted as the design tool (for flow problems), a few key questions must still be answered, namely those of accuracy control (level and distribution) and repeatability (solutions are dependent on grids, dissipation parameters and limiters, as well as users' preferences and biases) ...*

The answer to the first question depends on the development of error indicators [91, 96] capable of giving consistent estimates of the accuracy of the solution. The second question is mostly answered by the introduction of grid adaptation [91, 96], which consists of adjusting the domain discretization to the requirements of the evolving solution. The combination of these two techniques is slowly becoming the basis of the development of modern CFD codes and may also lead to the definition of new concepts in CFD, namely those of *grid-independent* and *scheme-independent solutions* and, hence indirectly *user-independent solutions* [41].

The basic idea underlying most adaptive methods is to assess the quality of an initial numerical solution by employing some form of *a posteriori* error estimate and to then dynamically change the mesh and/or the interpolation space, in a systematic manner, to improve the quality of the solution. The ultimate goal of mesh adaptation methods is the production of the best numerical simulation of a given problem, for the least computational cost. Adaptation methods usually make the difference between being or not being able to solve a certain problem to an acceptable accuracy, in a reasonable time. Without them,

one would be forced to use much coarser grids, with lower accuracy, for the same expense. Furthermore, they free the user from the tedious task of intuitively constructing a suitable mesh, which would give an accurate and efficient solution of a given problem. With adaptation, any initial grid may systematically be transformed into a near-optimal mesh for the solved problem.

Most grid adaptation methods are composed of an *error estimate*, an *adaptive strategy* and an *optimal-mesh criterion*.

### 1.5.2 Error Estimates

The aim of an error estimate is to give an indication of the accuracy of the solution. In the general case, the only data available for the derivation of such estimates is, however, the approximate solution itself. Therefore, the challenge is to develop *a posteriori* error estimates, that is, after an initial approximate solution has been computed.

The different techniques, which are used in *a posteriori* error estimation, may be classified into three major groups:

- Interpolation methods
- Post-processing methods
- Element residual methods

#### Interpolation Methods

These methods are directly derived from the interpolation theory of finite elements and aim to produce inexpensive estimates of the local error over individual elements. They consist of estimating the highest derivative dropped from the solution when expanded as a Taylor series and the highest order terms neglected [5, 79, 108]. These terms are generally computed by various recovery methods.

Interpolation methods are popular among developers of grid adaptation methods due to their ease of implementation and low cost of their evaluation. They are essentially operator-independent (i.e. independent of the governing equations of the solved problem) and their computational algorithms are characterized by a high portability among solvers. In fact, such error estimates depend only on the calculated solution and the interpolation functions used to obtain it, and therefore, can be applied to a large variety of CFD problems.

### **Post-Processing Methods**

In this approach, an estimate of the error is obtained by comparing an enhanced post-processed approximate solution with the regularly calculated solution. The construction of an enhanced version of an approximate solution is essentially based on projection [133, 134, 135] or extraction methods [12, 13, 14]. For instance, the solution of a second order PDE by finite element methods with linear interpolation functions results in a solution with discontinuous first derivatives. The jump in the first derivatives, at element interfaces, may thus serve as an error indicator. More accurate derivatives may be recovered using various projections techniques and an error estimate can be defined as a norm of the difference between the approximate derivative and the corresponding recovered one. Since the projection operation is not usually performed on an element basis, the post-processing approach often requires more computer resources than the interpolation methods .

### **Element Residual Methods**

The residual of a numerical solution is defined as the measure of how much the approximate solutions fails to satisfy the governing differential equations and their associated boundary conditions. This property represents a quality indicator of an approximate solution and can be used as an error estimate by evaluating the upper bound of the residual over each element [16, 93]. This is usually done by solving local boundary-value problems. The residual methods are always operator-dependent and generally lead to very accurate error estimates.

On the other hand, this accuracy means that a significant amount of computational time is required in the evaluation of these estimates.

### 1.5.3 Adaptive Strategies

An adaptive strategy is a mechanism to enrich the grid and/or the interpolation space under the guidance of an error estimate, in order to improve the quality of a numerical solution. The adaptive strategies can be classified into four categories: node-moving schemes ( $r$ -methods), mesh refinement/coarsening schemes ( $h$ -methods), subspace enrichment schemes ( $p$ -methods), remeshing methods, and hybrid techniques combining these four methods. In order to describe each strategy, let us illustrate them through a 2-D inviscid shock-tube problem, where the normal shock resolution is to be improved by the application of the above strategies on the initial grid, Fig. 1.1.

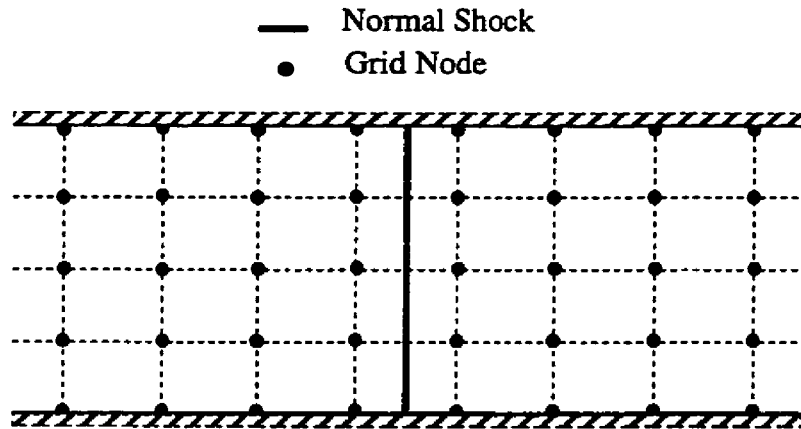


Figure 1.1: Initial grid

#### $r$ -Method

In this method, also called *node redistribution*, a new adapted mesh is produced by moving the nodes of an initial grid. The grid nodes are relocated so that the grid is dense in

regions of high error and coarser in regions of smoother solution (see Fig. 1.2). Node-moving schemes are easy to implement and do not require any elaborate data-structure management. However, the quality of the adapted solution could be highly dependent on the density of the initial mesh. In fact, for any grid with a fixed number of points and fixed order of interpolation within each element, there is an inherent threshold under which the error cannot be further reduced. A detailed review of such methods can be found in the paper by Hawken *et al.* [57].

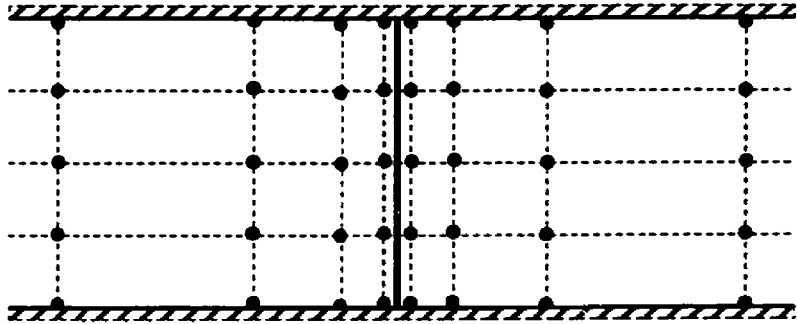


Figure 1.2: Adapted grid produced by an  $r$ -method

### *h*-Method

This method automatically refines/coarsens a mesh whenever the local error indicator exceeds a user-prescribed tolerance (as illustrated in Fig. 1.3). Such schemes modify the connectivity table after each adaptation process and therefore demand an elaborate data management. In addition, the hanging nodes (i.e. nodes that are extraneous to the interpolation level) that are generated during the refinement process of a structured grid require special treatment. However, an  $h$ -method can be very effective in producing nearly optimal meshes [81, 95].

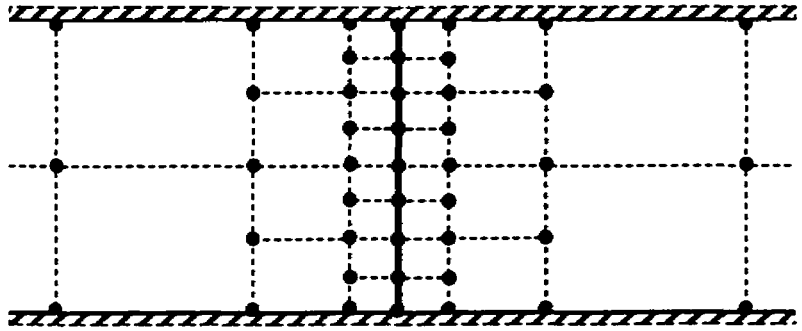


Figure 1.3: Adapted grid produced by an  $h$ -method

### $p$ -Method

The  $p$ -method attempts to reduce the error by enriching the interpolation space [52, 109]. As shown in Fig. 1.4, the order of interpolation of each element is increased wherever the local error indicator exceeds a preassigned tolerance. Such approach requires the implementation of an imposing data structure in order to manage the degrees of freedom of each element. Although the concept of hierarchical elements were developed to facilitate the construction and the management of the necessary shape functions, the satisfaction of the Ladyzenskaya, Babuška and Brezzi (LBB) stability condition, in certain formulations, significantly restricts the use of this method.

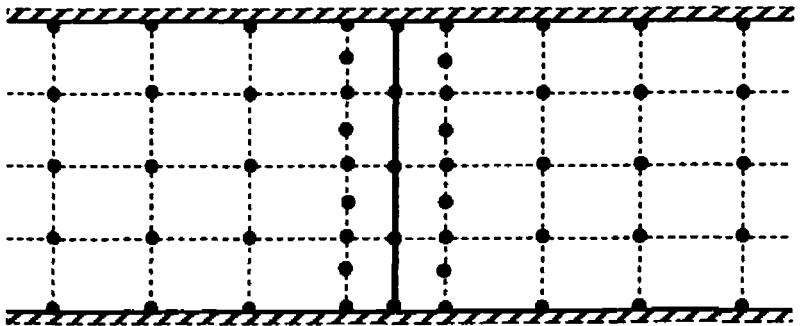


Figure 1.4: Adapted grid produced by a  $p$ -method

## Remeshing Method

This method possesses several common points with  $h$ -methods and may be viewed as a combination of several techniques such as refinement, coarsening, edge-swapping and smoothing. A new mesh is regenerated using the error indicator that is provided on a background mesh (see the Fig. 1.5). The new grid will contain more nodes in regions with high error, while regions with smooth solution will be meshed with relatively coarse elements. Such schemes are tightly coupled to certain grid generators and consequently may not be portable. A description of some versions of this method can be found in references [80, 107, 108].

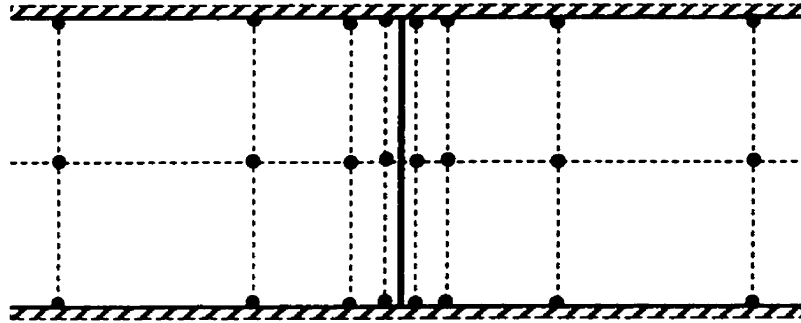


Figure 1.5: Adapted grid produced by a remeshing method

## Combined Methods

Although the above methods were initially designed to be applied in a separate manner, the combination of such strategies may lead to very effective schemes. For instance, a hybrid  $h$ - $p$  method may result in an exponential rate of convergence [53, 54, 52], for certain type of problems, by optimally decreasing the mesh size  $h$  and increasing polynomial degree  $p$ . This method was successfully used in the solution of incompressible viscous flows [92, 94, 97] but one may encounter serious difficulties in predicting compressible flows with shocks.

Another combined method consists of coupling an  $r$ -method with an  $h$ -method. The resulting  $r$ - $h$  scheme might be used effectively in problems involving the resolution of some directional flow features (shocks, contact discontinuities and boundary layers) where the  $r$ -method is first introduced to align and stretch the mesh along those directions prior to a mesh refinement [42, 99].

#### 1.5.4 Optimal-Mesh Criterion

The definition of an optimal mesh is not necessarily unique [107]. It can be defined as a mesh with a minimum number of degrees of freedom required to achieve a specified level of error, or it can be interpreted as the mesh in which a given number of degrees of freedom are distributed in such a manner that the error is minimal. It is obvious that both definitions can be achieved by  $h$ - or  $p$ -methods where a certain tolerance may be prescribed. For an  $r$ -method, where no additional degrees of freedom are introduced, the second definition is usually adopted.

It should be noted that the concept of optimality is intimately linked to that of accuracy, which is also not uniquely defined [107]. In fact, optimality of a mesh should be defined with respect to a certain norm of the error. For elliptic problems, the development of *a posteriori* error estimates has already reached a high level of maturity. Detailed theoretical basis have been derived and error indicators for such problems have been shown to be bounded and to converge asymptotically with successive refinements. For gasdynamic problems with shocks, most of these developments are, however, not applicable and a more heuristic approach is usually adopted.

### 1.6 Directionally-Adaptive Methods

An accurate prediction of a typical hypersonic flow includes the resolution of very strong shocks, followed by extremely fast vibrational relaxations and intense chemical reactions.

The regions containing these important phenomena are characterized by steep *directional* gradients of flow variables and are *a priori* unknown and embedded in regions where the solution varies more smoothly. Hence, an accurate numerical simulation of such flows should theoretically require a fine meshing of the whole computational domain, compounding the complexity of the problem. One efficient alternative would consist of seeking solutions on *directionally-adapted grids*.

Even when the same error estimate is used to assess the accuracy of a solution, the resulting adapted grid strongly depends on the selected adaptation strategy. Classical techniques such as standard  $h$ -methods [83, 95] produce isotropic meshes in which the length-scales of each element are essentially the same. These techniques are optimal only for those flow field regions possessing nearly equal variations in all spatial directions. As a result, *directional flow features* are not necessarily adapted efficiently and the number of elements needed to represent those may increase disproportionately with each isotropic refinement.

An alternative approach would be to build *anisotropic meshes* where selective resolution is introduced along those directions with rapidly changing flow variables. This idea was introduced by Peraire *et al.* [108], who used an adaptive remeshing procedure that incorporated directional stretching for the solution of the 2-D Euler equations on triangular grids. Anisotropic grids may also be produced by coupling a mesh movement strategy with local isotropic refinement ( $r$ - $h$  method) [99]. Kornhuber *et al.* [74] proposed an anisotropic strategy based on directed refinement of pairs of triangular elements to resolve boundary layers. Recently, Fortin *et al.* [42] used a metric as a measure of error, coupled to an  $r$ - $h$  strategy, to achieve directionally adapted unstructured grids with high aspect ratios.

The above approaches have primarily been used on unstructured meshes because of the intrinsic ability of triangular elements in 2-D and tetrahedral elements in 3-D to deal with arbitrary complex geometries. In addition, such meshes provide a natural setting for

the implementation of adaptive grid techniques. Unstructured adaptation algorithms can yield highly stretched grids, as well as locally refined/coarsened meshes. In contrast, most refinement techniques for structured grids [28, 70, 95] avoid propagating the refinement to the boundaries by allowing sides to have hanging nodes.

Despite these advantages for unstructured meshes, structured grids of quadrilateral elements in 2-D and hexahedral elements in 3-D are still used with great success in CFD [10, 28, 65]. One reason is their ability to include multigrid acceleration techniques in a straightforward manner, while unstructured grids may encounter some difficulties in generating multi-level grids [75, 86]. Moreover, integration of PDEs on a structured grid requires less CPU time than on an unstructured one, for the same number of nodes. Structured grids are also more suitable for turbulence modeling, particularly near solid walls where normals to walls may be necessary.

Furthermore, a certain degree of grid anisotropy [5, 6] may also be introduced for structured grids through an improved mesh movement scheme to be presented in Chapter 3. The classical mesh movement technique was originally introduced by Gnoffo [47], generalized by Nakahashi [89] in the context of finite volume methods and applied to a finite element method by Löhner [83]. All these mesh movement schemes are based on a spring analogy where the grid is viewed as a network of springs whose stiffness constants represent a measure of error. The grid vertices are displaced until the equilibrium state of the spring forces is reached. Such classical techniques are characterized by their low cost and the conservation of nodal connectivity, but can often stall or diverge and tolerate only a limited range of nodal movement.

## 1.7 Objectives and Thesis Overview

In this thesis, a finite element, segregated, implicit method is developed for two-dimensional, inviscid, hypersonic, thermo-chemical equilibrium and nonequilibrium flows,

with an emphasis on resolving directional flow features such as shocks by an anisotropic mesh adaptation technique.

This methodology is valid for a large variety of CFD problems including frozen, chemical equilibrium/nonequilibrium and thermal equilibrium/nonequilibrium flows, and also covers a wide range of speeds, from subsonic internal flows to hypersonic external flows. All these CFD problems are efficiently tackled by a unified code in which easy deletion or addition of chemical species or extra physical modeling is possible. This was made feasible by adopting a segregated approach which decouples the governing equations to several systems of PDEs according to their physical category.

The second chapter of this thesis deals with the numerical discretization of the Euler equations in the case of thermo-chemical equilibrium flows. A finite element weak-Galerkin formulation is derived using two different approaches for computing the flux Jacobian matrices. The first approach assumes that the equation of state is given by a general analytical form for a divariant gas and leads to an exact evaluation of the Jacobian matrices. In the second approach, an equivalent ratio of specific heats (*equivalent- $\tilde{\gamma}$* ) is introduced in the perfect gas law to reproduce the behavior of the considered thermo-chemical equilibrium gas. Such a formulation is widely adopted in the extension of existing gasdynamic codes to reacting flows as it requires no modification of the flux Jacobian matrices.

The computational domain is subdivided into quadrilateral elements on which the flow variables are approximated by bilinear shape functions. An artificial dissipation, necessary to prevent instabilities, is added in the form of Laplacians of conservative variables, but the isoenthalpic steady flow solutions is recovered by substituting the total internal energy by the total enthalpy in the dissipative terms of the energy equation.

Chapter three describes the two major ingredients of a directionally-adaptive method, namely edge-based error estimate and mesh movement scheme, with validations on several

relevant benchmarks. The quality of the numerical solution is assessed through its Hessian (matrix of second derivatives) which is then modified by taking the absolute value of its eigenvalues to finally produce a Riemannian metric. Using elementary differential geometry, the edge-based error estimate is thus defined as the length of the element edges in this Riemannian metric. This error is then equidistributed over the mesh edges by applying a mesh movement scheme similar to [89], but made vastly more efficient by removing the constraints on grid orthogonality.

Chapter four is devoted to the mathematical modeling of hypersonic thermo-chemical nonequilibrium flows. The chemical phenomena are modeled by a set of coupled species transport equations, wherein the source terms represent the rate of mass transfer among species (production or destruction of any species) during chemical reactions. Thermal effects are introduced by considering a set of coupled PDEs for the conservation of vibrational energy for every molecular species.

The number of species transport equations is drastically reduced by neglecting the ionization phenomenon, thus leaving one to represent the air by the five neutral species: O, N, NO, O<sub>2</sub> and N<sub>2</sub>. This system of equations is further simplified by considering an algebraic equation for conservation of elemental nitrogen to oxygen ratio in air. The chemical source terms are computed according to kinetic models where reaction rate coefficients are given by Park's reaction models [100, 105].

In the present study, the translational and rotational modes are assumed to be in equilibrium and, they can, hence, be characterized by a single temperature. All molecular species are also characterized by a unique vibrational temperature yielding a *two-temperature thermal model* which requires the solution of a single conservation equation for the total vibrational energy.

Chapter five presents a numerical solution of the thermo-chemical nonequilibrium gov-

erning equations with validation against experimental results. The present numerical approach is also based on a Galerkin-finite element method coupled to the mesh adaptation procedure described for Chapter 3.

In the entire work, the governing equations are subdivided into three systems of PDEs –*gasdynamic*, *chemical* and *vibrational* systems– and marched in pseudo-time to steady-state by an implicit technique. This *loosely coupled* approach enjoys the robustness of an implicit formulation while keeping the memory requirements to a manageable level. It also allows each system of PDEs to be integrated by the appropriate algorithm in an attempt to achieve the best global convergence. This particular feature makes the present approach quite attractive for the extension of existing gasdynamic codes to hypersonic flow problems, as well as for applications having stiff source terms, such as reacting flows.

Finally, Chapter 6 states the major conclusions and briefly presents an outline of potential future research themes.

# Chapter 2

## Numerical Discretization of Euler Equations for Divariant Gases

### 2.1 Introduction

Many of numerical techniques for the Euler and Navier-Stokes equations are stabilized by algorithms that fall into the category of *upwind* schemes. These schemes, which include *flux-vector splitting* [114, 120] and *flux-difference splitting* [48, 111], relate numerical space differencings to the physical propagation properties of the solutions. The flux-vector splitting is totally dependent on the homogeneous feature of the inviscid fluxes and discretize these fluxes with respect to the sign of the associated propagation speeds. More physical properties are, however, introduced in the definition of the second splitting where the exact solution of the exact/approximate Riemann problem is used in the calculation of the fluxes at cell interfaces.

These two type of splittings were primarily developed for perfect gases and do not directly extend to general divariant gases [43, 51]. In this case, *equivalent- $\gamma$*  approximation [45] is usually used to recover the homogeneity feature of the inviscid fluxes in the

Steger and Warming scheme and to facilitate the computation of the Roe flux upwinding at the intermediate states [51].

On the other hand, central differencing schemes [17, 66, 82], including Galerkin-finite element methods, are fully independent of the direction of disturbance propagations. As matter of fact, these schemes are usually stabilized by adding dissipative operators, such as Laplacians of conservative variables, to the governing equations and assume no approximation on the equation of state.

This Chapter describes an implicit Galerkin-finite element method for the Euler equations within the context of divariant gases. This approach permits real gas effects to be included in several ways and results in a very flexible and portable code. It is also valid for a large variety of CFD problems ranging from subsonic to hypersonic flows of frozen and thermo-chemical equilibrium gases.

An analytical divariant gas law or a curve fit to thermodynamic data may be used as a closure equation for frozen flows. For reacting flow problems, however, an equilibrium procedure should be included in order to update the species concentration and the remaining thermodynamic variables such as pressure, temperature or the ratio of the specific heats. This procedure may be in the form of curve fits or a free-energy minimization routine for general gas mixtures.

Here, two formulations based on an exact and an approximate (*equivalent- $\tilde{\gamma}$* ) flux Jacobian matrix are presented. In the first approach, an exact form of the Jacobian matrix is developed by assuming that the equation of state is given by a general function for a divariant gas. Although, this formulation yields a robust solution method, the evaluation of the Jacobian matrices prohibitively expensive.

In the second approach, the perfect gas law with an equivalent ratio of specific heats,  $\tilde{\gamma}$ , is used to reproduce the behavior of the considered real gas. Such a formulation, also

called *variable-effective-gamma*, has been introduced by Gnoffo [45] and is highly suitable for extending the existing gasdynamic codes due to the rather minor modifications involved in its computer implementation.

## 2.2 Governing Equations

The conservation form of the mass, momentum and energy equations describing an inviscid compressible flow may be written as

$$\mathbf{Q}_{,t} + \mathbf{F}_{i,i} = \mathbf{S}, \quad (2.1)$$

where  $\mathbf{Q}$  represents the vector of the conservative variables,  $\mathbf{F}_i$  is the vector of convective fluxes and  $\mathbf{S}$  is the vector of source terms. Indices  $i$  in the above formula refer to the axes of Cartesian coordinate system, a comma denotes partial differentiation and the Einstein summation convention is applied. In 2-D problems, the components of vectors  $\mathbf{Q}$  and  $\mathbf{F}_i$  are given by

$$\mathbf{Q} = \begin{bmatrix} \rho \\ \rho v_1 \\ \rho v_2 \\ \rho e \end{bmatrix}, \quad \mathbf{F} = \begin{bmatrix} \rho v_i \\ \rho v_1 v_i + p \delta_{1i} \\ \rho v_2 v_i + p \delta_{2i} \\ (\rho e + p) v_i \end{bmatrix}, \quad (2.2)$$

where  $\rho$  is the density,  $v_i$  the two components of the velocity vector  $\mathbf{v}$ ,  $p$  the pressure,  $\delta_{ij}$  the Kronecker delta symbol and  $e$  the specific total internal energy per unit mass. Here, the source vector  $\mathbf{S}$  is identically zero and is only introduced in the governing equations to keep the numerical formulation as general as possible.

The solution of the conservation laws (2.1) requires an additional closure relation, namely *the equation of state*, to express the thermodynamic state of the fluid. The expression of this equation depends on the type of flow, namely, perfect gases (frozen flow), mixtures of perfect gases in chemical equilibrium/ nonequilibrium or mixtures of perfect

gases in thermo-chemical non-equilibrium.

We recall that all the thermodynamic properties of a divariant gas including its chemical composition in the case of a reacting gas-mixture, are completely defined in terms of two thermodynamic quantities [132], such as temperature,  $T$ , and density,  $\rho$ . A gas flow can be described by as divariant gas under the following conditions:

- (i) The gas is in a thermal equilibrium state.
- (ii) The gas mixture is either frozen or in a chemical equilibrium.

For a general divariant gas, the pressure function may be expressed as

$$p = p(\varepsilon, \rho), \quad (2.3)$$

where  $\varepsilon$  denotes the internal energy per unit mass and is given by

$$\varepsilon = e - \frac{1}{2} v_i v_i. \quad (2.4)$$

In the case of an ideal gas, the equation of state (2.3) takes the simple following form

$$p = (\gamma - 1)\rho\varepsilon, \quad (2.5)$$

where  $\gamma$  denotes the ratio of specific heats of the fluid.

## 2.3 Non-Dimensional Form

The Euler equations (2.1) are presented in dimensional form. In order to minimize the roundoff errors that are generated by differences in flow-variable scales, a non-dimensionalization of those variables is introduced. In addition, the use of non-dimensional

variables eliminates the problem of units and makes the resulting code applicable for general problems. In the present study, the flow variables are non-dimensionalized as follows

$$\begin{aligned}\tilde{x} &= \frac{x}{\mathcal{L}}, & \tilde{v} &= \frac{v}{|v_\infty|}, & \tilde{p} &= \frac{p}{\rho_\infty v_\infty^2}, \\ \tilde{\rho} &= \frac{\rho}{\rho_\infty}, & \tilde{e} &= \frac{e}{v_\infty^2},\end{aligned}\tag{2.6}$$

where the tilde symbol  $\tilde{\cdot}$  refers to non-dimensional variables, the subscript  $\infty$  denotes the freestream state and  $\mathcal{L}$  is a characteristic length of the problem.

In contrast to Navier-Stokes equations, the Euler equations have a particular feature of remaining invariant after a non-dimensionalization operation. For simplicity, the tilde symbol will be omitted in the rest of the numerical formulation.

## 2.4 Weak-Galerkin Formulation

The weak formulation is obtained by minimizing the residuals of equation (2.1) over the solution domain. The system (2.1) is multiplied by a weight function and integrated over the domain, yielding

$$\int_{\Omega} (\mathbf{Q}_{,t} + \mathbf{F}_{i,i} - \mathbf{S}) \mathbf{W} \, d\Omega = 0,\tag{2.7}$$

where the weight functions  $\mathbf{W}$  are identical, in a Galerkin finite element formulation, to the interpolation functions of the variables. By making use of the Gauss-divergence theorem, the following weak statement is obtained

$$\int_{\Omega} \mathbf{Q}_{,t} \mathbf{W} \, d\Omega - \int_{\Omega} \mathbf{F}_i \mathbf{W}_{,i} \, d\Omega + \int_{\Gamma} \mathbf{F}_i n_i \mathbf{W} \, d\Gamma - \int_{\Omega} \mathbf{S} \mathbf{W} \, d\Omega = 0,\tag{2.8}$$

where  $\Gamma$  denotes the boundary of the domain  $\Omega$  and  $n_i$  is the  $i^{th}$  component of the outward unit normal to the boundary  $\Gamma$ .

## 2.5 Temporal Discretization

The steady-state solution of system (2.8) is obtained by an implicit time-marching technique, with the discretization of the time-dependent term based on a backward first-order difference. Accordingly, equation (2.8) is expressed as

$$\int_{\Omega} \frac{\Delta Q}{\Delta t} W \, d\Omega - \int_{\Omega} F_i^{n+1} W_{,i} \, d\Omega + \int_{\Gamma} F_i^{n+1} n_i W \, d\Gamma - \int_{\Omega} S^{n+1} W \, d\Omega = 0, \quad (2.9)$$

where  $\Delta Q$  denotes the increment of the solution after a period of time  $\Delta t$ .

To solve the nonlinear semi-discrete form (2.9), a linearization in time about the time level  $n$  is applied [4], yielding

$$\begin{aligned} Q^{n+1} &\cong Q^n + L^n \Delta U, \\ F_i^{n+1} &\cong F_i^n + A_i^n \Delta U, \\ S^{n+1} &\cong S^n + B^n \Delta U, \end{aligned} \quad (2.10)$$

where  $U = [\rho, v_1, v_2, e]^T$  represents the vector of primitive variables. The Jacobian matrices defined by

$$L = \frac{\partial Q}{\partial U}, \quad A_i = \frac{\partial F_i}{\partial U}, \quad B = \frac{\partial S}{\partial U}, \quad (2.11)$$

are derived in the next section.

Upon the substitution of the linearization given by equations (2.10), the equation (2.9) can be expressed as follows:

$$\begin{aligned} \int_{\Omega} L \frac{\Delta U}{\Delta t} W \, d\Omega - \int_{\Omega} (A_i \Delta U W_{,i} + B \Delta U W) \, d\Omega + \int_{\Gamma} A_i n_i \Delta U W \, d\Gamma = \\ \int_{\Omega} (F_i W_{,i} + S W) \, d\Omega - \int_{\Gamma} F_i n_i W \, d\Gamma. \end{aligned} \quad (2.12)$$

where the superscript  $n$  is dropped for simplicity.

## 2.6 Derivation of Jacobian Matrices

### 2.6.1 Exact Form

The Jacobian matrix of the inviscid flux may be derived as

$$\mathbf{A}_i = \begin{bmatrix} v_i & \rho\delta_{1i} & \rho\delta_{2i} & 0 \\ v_1v_i + p_{,\rho}^*\delta_{1i} & \rho(v_i + v_1\delta_{1i}) + p_{,v_1}^*\delta_{1i} & \rho v_1\delta_{2i} + p_{,v_2}^*\delta_{1i} & p_{,e}^*\delta_{1i} \\ v_2v_i + p_{,\rho}^*\delta_{2i} & \rho v_2\delta_{1i} + p_{,v_1}^*\delta_{2i} & \rho(v_i + v_2\delta_{2i}) + p_{,v_2}^*\delta_{2i} & p_{,e}^*\delta_{2i} \\ v_i(e + p_{,\rho}^*) & (\rho e + p)\delta_{1i} + v_i p_{,v_1}^* & (\rho e + p)\delta_{2i} + v_i p_{,v_2}^* & v_i(\rho + p_{,e}^*) \end{bmatrix}, \quad (2.13)$$

where the complete derivation of the inviscid flux Jacobian requires the knowledge of the following pressure derivatives

$$p_{,\rho}^* = \left[ \frac{\partial p}{\partial \rho} \right]_{\mathbf{v},e}, \quad p_{,v_i}^* = \left[ \frac{\partial p}{\partial v_i} \right]_{\rho,v_j,e}, \quad p_{,e}^* = \left[ \frac{\partial p}{\partial e} \right]_{\rho,\mathbf{v}}. \quad (2.14)$$

By the chain rule for partial derivatives, however, we have:

$$\begin{aligned} \left[ \frac{\partial p}{\partial \rho} \right]_{\mathbf{v},e} &= \left[ \frac{\partial p}{\partial \rho} \right]_\epsilon + \left[ \frac{\partial p}{\partial \epsilon} \right]_\rho \left[ \frac{\partial \epsilon}{\partial \rho} \right]_{\mathbf{v},e}, \\ \left[ \frac{\partial p}{\partial v_i} \right]_{\rho,v_j,e} &= \left[ \frac{\partial p}{\partial \epsilon} \right]_\rho \left[ \frac{\partial \epsilon}{\partial v_i} \right]_{\rho,v_j,e}, \\ \left[ \frac{\partial p}{\partial e} \right]_{\rho,\mathbf{v}} &= \left[ \frac{\partial p}{\partial \epsilon} \right]_\rho \left[ \frac{\partial \epsilon}{\partial e} \right]_{\rho,\mathbf{v}}, \end{aligned} \quad (2.15)$$

where  $\epsilon$  derivatives are computed from the general equation for a divariant gas (2.3) as

$$\left[ \frac{\partial \epsilon}{\partial \rho} \right]_{\mathbf{v},e} = 0, \quad \left[ \frac{\partial \epsilon}{\partial v_i} \right]_{\rho,v_j,e} = -v_i, \quad \left[ \frac{\partial \epsilon}{\partial e} \right]_{\rho,\mathbf{v}} = 1. \quad (2.16)$$

Substituting the equation (2.16) into the equation (2.15) leads to

$$\begin{aligned} \left[ \frac{\partial p}{\partial \rho} \right]_{v,\epsilon} &= \left[ \frac{\partial p}{\partial \rho} \right]_\epsilon = p_{,\rho}, \\ \left[ \frac{\partial p}{\partial v_i} \right]_{\rho,v_j,\epsilon} &= \left[ \frac{\partial p}{\partial \epsilon} \right]_\rho (-v_i) = -v_i p_{,\epsilon}, \\ \left[ \frac{\partial p}{\partial e} \right]_{\rho,v} &= \left[ \frac{\partial p}{\partial \epsilon} \right]_\rho = p_{,\epsilon}. \end{aligned} \quad (2.17)$$

By substituting the derivatives given by (2.17) into Jacobian matrix (2.17), one obtains

$$A_i = \begin{bmatrix} v_i & \rho \delta_{1i} & \rho \delta_{2i} & 0 \\ v_1 v_i + p_{,\rho} \delta_{1i} & \rho v_i + v_1 (\rho - p_{,\epsilon}) \delta_{1i} & \rho v_1 \delta_{2i} - v_2 p_{,\epsilon} \delta_{1i} & p_{,\epsilon} \delta_{1i} \\ v_2 v_i + p_{,\rho} \delta_{2i} & \rho v_2 \delta_{1i} - v_1 p_{,\epsilon} \delta_{2i} & \rho v_i + v_2 (\rho - p_{,\epsilon}) \delta_{2i} & p_{,\epsilon} \delta_{2i} \\ v_i (e + p_{,\rho}) & (\rho e + p) \delta_{1i} - v_i v_1 p_{,\epsilon} & (\rho e + p) \delta_{2i} - v_i v_2 p_{,\epsilon} & v_i (\rho + p_{,\epsilon}) \end{bmatrix}. \quad (2.18)$$

For the particular case of a perfect gas, the equation of state is

$$p = (\gamma - 1) \rho \epsilon, \quad (2.19)$$

giving

$$\begin{cases} p_{,\epsilon} = (\gamma - 1) \rho \\ p_{,\rho} = (\gamma - 1) \epsilon \end{cases} \quad (2.20)$$

and thus, the Jacobian (2.18) becomes

$$A_i = \begin{bmatrix} v_i & \rho \delta_{1i} & \rho \delta_{2i} & 0 \\ v_1 v_i + \gamma_1 \epsilon \delta_{1i} & \rho v_i + (1 - \gamma_1) \rho v_1 \delta_{1i} & \rho v_1 \delta_{2i} - \gamma_1 \rho v_2 \delta_{1i} & \gamma_1 \rho \delta_{1i} \\ v_2 v_i + \gamma_1 \epsilon \delta_{2i} & \rho v_2 \delta_{1i} - \gamma_1 \rho v_1 \delta_{2i} & \rho v_i + (1 - \gamma_1) \rho v_2 \delta_{2i} & \gamma_1 \rho \delta_{2i} \\ v_i (e + \gamma_1 \epsilon) & (\rho e + p) \delta_{1i} - \gamma_1 \rho v_i v_1 & (\rho e + p) \delta_{2i} - \gamma_1 \rho v_i v_2 & \gamma \rho v_i \end{bmatrix}, \quad (2.21)$$

where  $\gamma_1 = \gamma - 1$ .

## 2.6.2 Approximate Form

Another easy alternative to include real gas effects into a perfect gas solver is based on the *equivalent- $\tilde{\gamma}$*  concept. In this formulation, the equation of state of a real gas is cast into the ideal gas form

$$p = (\tilde{\gamma} - 1)\rho\varepsilon, \quad (2.22)$$

permitting the reuse of the Jacobian matrices that were developed for a perfect gas (2.21). Here  $\tilde{\gamma} = \tilde{\gamma}(e, \rho)$  is a function that varies more slowly than the other thermodynamic variables and its value remains between 1 and 5/3 even when the values of  $e$  and  $\rho$  vary over several orders of magnitude [27].

The value of  $\tilde{\gamma}$  is deduced from equation (2.22) as

$$\tilde{\gamma} = 1 + \frac{p}{\rho\varepsilon}, \quad (2.23)$$

so the value of the pressure matches the one given by the real gas. In practical situations, the pressure is determined from an equilibrium curve fit  $p = p(\rho, \varepsilon)$  and then the *equivalent- $\tilde{\gamma}$*  is evaluated according to equation (2.23).

It must be pointed out that the influence of Jacobian matrices is limited to the left-hand-side (LHS) of the semi-discrete system (2.12), independently of the approach used in their evaluations. This LHS term is viewed as a preconditioning operator that have no influence on the steady solution as far as accuracy is concerned. For upwind schemes, however, the flux splitting depends highly on the *equivalent- $\tilde{\gamma}$*  approximation and so it will be for the resulting solutions.

## 2.7 Finite Element Space Discretization

In finite element methods, the computational domain is subdivided into a number of elements,  $\Omega = \cup_{e=1}^{N_e} \Omega_e$ , where the solution vector  $\mathbf{U}$  is approximated by shape functions,

usually polynomials, leading to

$$\mathbf{U} \cong \mathbf{U}^h = \sum_{J=1}^{N_n} \hat{\mathbf{U}}_J(t) \Phi_J(\mathbf{x}). \quad (2.24)$$

Here,  $\hat{\mathbf{U}}_J$  represents nodal values of the approximate solution  $\mathbf{U}^h$ ,  $\Phi_J$  is the shape function associated with node  $J$  and  $N_n$  is the total number of nodes.

Substituting equation (2.24) into the variational statement (2.12), one obtains the following algebraic system of equations:

$$(\mathbf{M} + \mathbf{K})\Delta\hat{\mathbf{U}} = -\mathbf{R}, \quad (2.25)$$

where the mass matrix  $\mathbf{M}$ , the stiffness matrix  $\mathbf{K}$  and the residual vector  $\mathbf{R}$  are given by

$$\begin{cases} \mathbf{M}_{IJ} &= \int_{\Omega} \frac{1}{\Delta t} \mathbf{L} \Phi_I \Phi_J \, d\Omega, \\ \mathbf{K}_{IJ} &= \int_{\Gamma} \mathbf{A}_i n_i \Phi_I \Phi_J \, d\Gamma - \int_{\Omega} [\mathbf{A}_i \Phi_{I,i} + \mathbf{B} \Phi_I] \Phi_J \, d\Omega, \\ \mathbf{R}_I &= \int_{\Gamma} \mathbf{F}_i n_i \Phi_I \, d\Gamma - \int_{\Omega} [\mathbf{F}_i \Phi_{I,i} + \mathbf{S} \Phi_I] \, d\Omega. \end{cases} \quad (2.26)$$

In the present formulation, the computational domain is subdivided into isoparametric quadrilateral elements with four nodes. Isoparametric elements are those defined as having equivalent variation of both the geometry and the solution variables.

In order to facilitate the computation of the coefficients of the global matrix and the residual vector (2.26), the surface integrals are broken up at the element level and then mapped to a master element  $\tilde{\Omega}$  of simple shape. These integrals are then evaluated numerically by applying the Gauss quadrature technique. As shown in Figure 2.1, the master element is a square whose coordinates vary from -1 to +1. For 2-D bilinear interpolation,

the polynomial shape functions in the master element are given by

$$\begin{cases} \phi_1 = \frac{1}{4}(1 - \xi)(1 - \eta), \\ \phi_2 = \frac{1}{4}(1 - \xi)(1 + \eta), \\ \phi_3 = \frac{1}{4}(1 + \xi)(1 + \eta), \\ \phi_4 = \frac{1}{4}(1 + \xi)(1 - \eta). \end{cases} \quad (2.27)$$

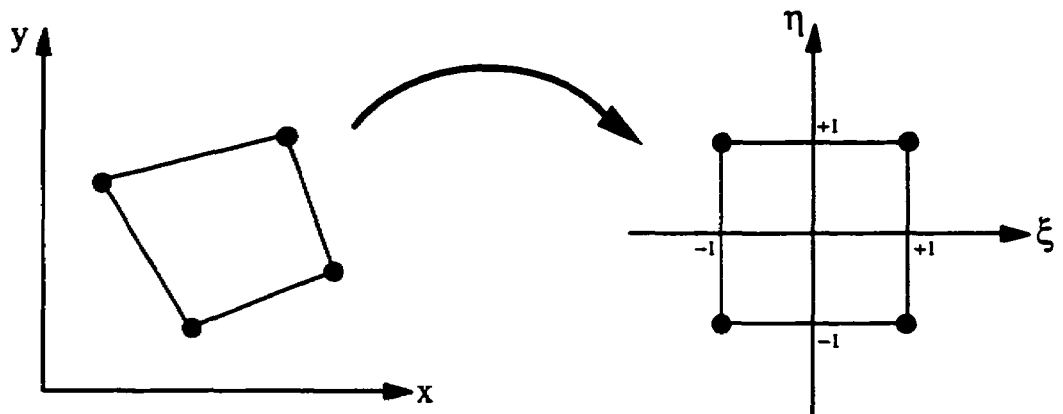


Figure 2.1: Quadrilateral element in the global coordinates (left) and the corresponding master element in the natural coordinates (right).

## 2.8 Artificial Dissipation

A Galerkin-FEM gives rise to central difference approximations of differential operators, which are nondissipative by themselves. In order to suppress the tendency for odd-even decoupling of the solution, and to prevent unphysical oscillations near discontinuities, artificial dissipation operators are added to the governing equations. These dissipative terms have no physical meaning, but are merely used as a tool to control numerical oscillations. The governing equations (2.1) are modified to include artificial dissipation as additional fluxes in the form

$$Q_{,t} + F_{i,i} = S + G_{i,i}, \quad (2.28)$$

where  $G_{i,i}$  denote dissipative terms.

The terms  $\mathbf{G}_i$  should be constructed in such a manner that it be successful in eliminating all physically meaningless oscillations, but must remain small enough in order to not pollute the approximate solution. Since the dissipative operator is calculated at each time-step iteration, along with the convective operator, the dissipative term should, furthermore, be constructed to be as inexpensive as possible. The dissipative terms are usually added in the form of Laplacians of conservative variables where the artificial dissipation fluxes  $\mathbf{G}_i$  are defined as in references [82, 98, 118] by:

$$\mathbf{G}_i = \epsilon Q_{,i}, \quad (2.29)$$

where  $\epsilon$  is a positive coefficient.

A desirable feature of a numerical scheme for the solution of the Euler equations is its capability to reproduce an isoenthalpic steady-state flow. That is, the value of the predicted total enthalpy should remain constant over the entire flow field if conditions dictate it. This property is an essential condition in order to obtain accurate stagnation temperatures. It is obvious that the use of the above artificial dissipation fluxes does not guaranty such property. To recover this feature, we introduce instead the following dissipative fluxes

$$\mathbf{G}_i = \epsilon \begin{bmatrix} \rho \\ \rho v_1 \\ \rho v_2 \\ \rho h \end{bmatrix}_{,i}, \quad (2.30)$$

where  $h$  represents the specific total enthalpy.

By comparing the above equation with standard dissipative terms that are given by (2.29), one may observe that only the total internal energy is replaced by the total enthalpy in the energy equation. With this modification, the energy equation reduces to the continuity equation multiplied by  $h_\infty$  in the case of an isoenthalpic steady-state flow.

Therefore,  $h = h_\infty$  may be admitted as a solution for the energy equation.

For the general case in which the artificial dissipation fluxes depend on both solution variables and their gradients, one can expand these fluxes as

$$\mathbf{G}_i^{n+1} \cong \mathbf{G}_i^n + \mathbf{C}_i^n \Delta \mathbf{U} + \mathbf{D}_{ij}^n \Delta \mathbf{U}_{,j}, \quad (2.31)$$

where the artificial dissipation Jacobians are defined by

$$\mathbf{C}_i = \frac{\partial \mathbf{G}_i}{\partial \mathbf{U}}, \quad \mathbf{D}_{ij} = \frac{\partial \mathbf{G}_i}{\partial \mathbf{U}_{,j}}. \quad (2.32)$$

In the present approach, the artificial dissipation coefficient  $\epsilon$  is lagged at the previous time step and hence, the Jacobian matrices  $\mathbf{C}_i$  and  $\mathbf{D}_{ij}$  may be expressed as

$$\mathbf{C}_i = \epsilon \begin{bmatrix} 0 & 0 & 0 & 0 \\ v_{1,i} & \rho_{,i} & 0 & 0 \\ v_{2,i} & 0 & \rho_{,i} & 0 \\ h_{,i} + \rho_i p_{,\rho\rho} + \epsilon_i p_{,\epsilon\rho} - & p_{,\epsilon}(v_{1,i} - \rho_{,i} \frac{v_1}{\rho}) & p_{,\epsilon}(v_{2,i} - \rho_{,i} \frac{v_2}{\rho}) & \rho_{,i}(p_{,\rho\epsilon} + 1) \\ \frac{1}{\rho}(\rho_{,i} p_{,\rho} + \epsilon_{,i} p_{,\epsilon}) + \rho_{,i} \frac{p}{\rho^2} & & & + \epsilon_{,i} p_{,\epsilon\epsilon} \end{bmatrix} \quad (2.33)$$

and

$$\mathbf{D}_{ij} = \epsilon \delta_{ij} \begin{bmatrix} 1 & 0 & 0 & 0 \\ v_1 & \rho & 0 & 0 \\ v_2 & 0 & \rho & 0 \\ h + p_{,\rho} - p/\rho & -p_{,\epsilon} v_1 & -p_{,\epsilon} v_2 & (\rho + p_{,\epsilon}) \end{bmatrix}. \quad (2.34)$$

For a perfect gas the above Jacobian matrices simplify to

$$C_i = \epsilon \begin{bmatrix} 0 & 0 & 0 & 0 \\ v_{1,i} & \rho_{,i} & 0 & 0 \\ v_{2,i} & 0 & \rho_{,i} & 0 \\ h_{,i} & (\gamma - 1)(\rho v_{1,i} - \rho_{,i} v_1) & (\gamma - 1)(\rho v_{2,i} - \rho_{,i} v_2) & \gamma \rho_{,i} \end{bmatrix} \quad (2.35)$$

and

$$D_{ij} = \epsilon \delta_{ij} \begin{bmatrix} 1 & 0 & 0 & 0 \\ v_1 & \rho & 0 & 0 \\ v_2 & 0 & \rho & 0 \\ h & -(\gamma - 1)\rho v_1 & -(\gamma - 1)\rho v_2 & \gamma \rho \end{bmatrix}. \quad (2.36)$$

The Galerkin-finite element formulation of equation (2.28) is obtained by modifying the discrete form (2.25) in the following manner,

$$(\tilde{\mathbf{M}} + \tilde{\mathbf{K}}) \Delta \hat{\mathbf{U}} = -\tilde{\mathbf{R}}, \quad (2.37)$$

where

$$\begin{cases} \tilde{\mathbf{M}}_{IJ} = \mathbf{M}_{IJ}, \\ \tilde{\mathbf{K}}_{IJ} = \mathbf{K}_{IJ} + \int_{\Omega} (\mathbf{C}_i \Phi_J + \mathbf{D}_{ij} \Phi_{J,i}) \Phi_{I,j} d\Omega - \int_{\Gamma} (\mathbf{C}_i \Phi_J + \mathbf{D}_{ij} \Phi_{J,i}) n_i \Phi_I d\Gamma, \\ \tilde{\mathbf{R}}_I = \mathbf{R}_I + \int_{\Omega} \mathbf{G}_i \Phi_{I,i} d\Omega - \int_{\Gamma} \mathbf{G}_i n_i \Phi_I d\Gamma. \end{cases} \quad (2.38)$$

## 2.9 Boundary Conditions

A typical computational domain for hypersonic flow problems around a blunt-body is shown in Figure 2.2. It is bounded by three types of boundaries: inflow  $\Gamma_{in}$ , outflow  $\Gamma_{out}$  and body surface  $\Gamma_b$ . Along the inflow boundary (i.e. freestream),  $\Gamma_{in}$ , all the properties of the flow should be known by specifying four variables such as  $(\rho, v_1, v_2, T)$  or  $(p, Mach, \alpha, T)$ . At a supersonic outflow boundary,  $\Gamma_{out}$ , no specifications are made.

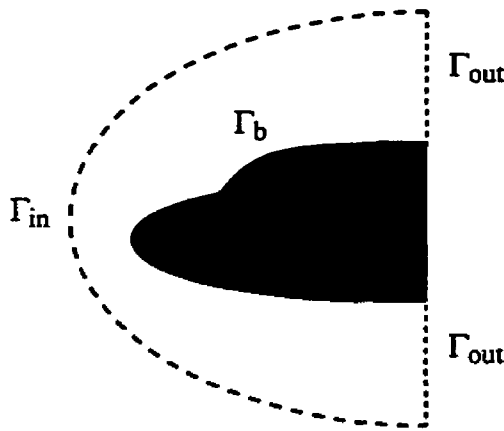


Figure 2.2: Computational domain for a blunt-body problem

Along the body surface,  $\Gamma_b$ , the no-penetration condition is imposed, that is

$$\mathbf{v} \cdot \mathbf{n} = 0. \quad (2.39)$$

This condition is enforced by neglecting the line integral of mass flux in the continuity equation.

# **Chapter 3**

## **Grid Adaptation**

### **3.1 Introduction**

In this chapter, a directionally-adaptive method, using an edge-based error estimate, is presented and implemented for quadrilateral grids. The use of an appropriate error estimate (directional estimate), combined with the vector nature (magnitude and direction) of spring forces in the mesh movement scheme, permits one to design a convergent adaptive procedure capable of achieving wide nodal movement and a high degree of grid anisotropy even on structured grids.

The quality of the numerical solution is evaluated using finite element interpolation theory. The error indicator is first derived for 1-D problems and then extended to the 2-D cases by introducing the Hessian matrix. The 4-component Hessian of a selected solution variable is computed and then modified to produce a positive-definite matrix, allowing one to define a measure of error, namely a Riemannian metric. The edge-based error estimate is thus expressed as the length of the edges of the elements in this Riemannian metric. The construction of an anisotropic mesh may thus be interpreted as seeking a uniform mesh in the defined metric. This metric introduces and controls the magnitude, as well as the

direction of the grid anisotropy.

Once the error estimate is evaluated, a nearly optimal mesh is sought by equidistributing this error. Following the classical approach, the optimal mesh for a fixed number of elements may be defined as one in which the error is equidistributed over each element [91]. The adaptive strategy presented in this work aims specifically to equidistribute the error over the edges of the elements. A mesh movement scheme is applied as the adaptive strategy, which in contrast to Nakahashi spring-analogy technique [89], forces no constraints on grid orthogonality. The scheme is also based on an explicit (node by node) approach, rather than line-relaxation, and hence requires no sophisticated relaxation technique to prevent degenerate elements [99]. This leads to a simple and efficient nodal redistribution algorithm, offering a greater range of grid point displacements.

This work is part of an ongoing research at the CFD Lab-GIREF groups to develop a library of routines [5, 6, 7, 32, 41, 42, 115, 119] for the optimization of 2-D and 3-D, structured and unstructured grids. To achieve this goal efficiently, the three principal components of the adaptive procedure should be characterized by a high degree of portability. For this purpose, the error estimate, adaptation criterion and grid operations were based on *element edges* which represent the elementary common feature to all considered meshes in FDMs, FVMs and FEMs. In the current study, we restrict ourselves to the application of an  $r$ -method on structured meshes although, it can be easily combined with any standard  $h$ -method, to satisfy a prescribed tolerance.

## 3.2 Edge-Based Error Estimate

Ideally, one would like to use a sharp estimate of the error during an adaptation process. Such error estimates, with an effectivity index close to unity, are usually difficult to derive for highly complex problems and quite costly to evaluate. Thus, it is not uncommon to use less precise, but easily computable, estimates as a basis for adaptive improvements. It is

important to keep in mind that an error estimate serves only to give a correct indication of relative error between successive meshes or approximations orders and its calculation should only take a small percentage of the global resolution time.

In the present section, an efficient and simple error estimate is derived using finite element interpolation theory. The solution is expanded in Taylor series and the higher-order terms, which have been neglected in the interpolation functions, are retained as an error indicator. For linear elements, these terms are proportional to second derivatives, as it will be shown later. For the sake of simplicity, the derivation of the error estimate is first carried out for the one-dimensional case and then extended to two-dimensional cases.

Consider a 1-D problem in which the solution  $g(x)$  is approximated by  $g^h(x)$ , with piecewise linear interpolation, as shown in Fig. 3.1. A local approximation error,  $E_e$ , is defined over an element  $e$  to be:

$$E_e(\bar{x}) = g(\bar{x}) - g_e^h(\bar{x}), \quad (3.1)$$

where  $\bar{x}$  belongs to the interval  $[0, h_e]$ .

The approximate solution,  $g_e^h$ , may be expressed as a function of its nodal values in the form

$$g_e^h(\bar{x}) = \left(1 - \frac{\bar{x}}{h_e}\right)g_I + \frac{\bar{x}}{h_e}g_{I+1}, \quad (3.2)$$

where here the origin of  $\bar{x}$  is placed at node  $I$ .

By expanding  $g_{I+1}$  into a Taylor series around node  $I$ , one obtains

$$g_{I+1} = g_I + h_e g_I' + \frac{h_e^2}{2} g_I'' + \dots \quad (3.3)$$

After substituting the equation (3.3) into (3.2) and making some simplifications, the solu-

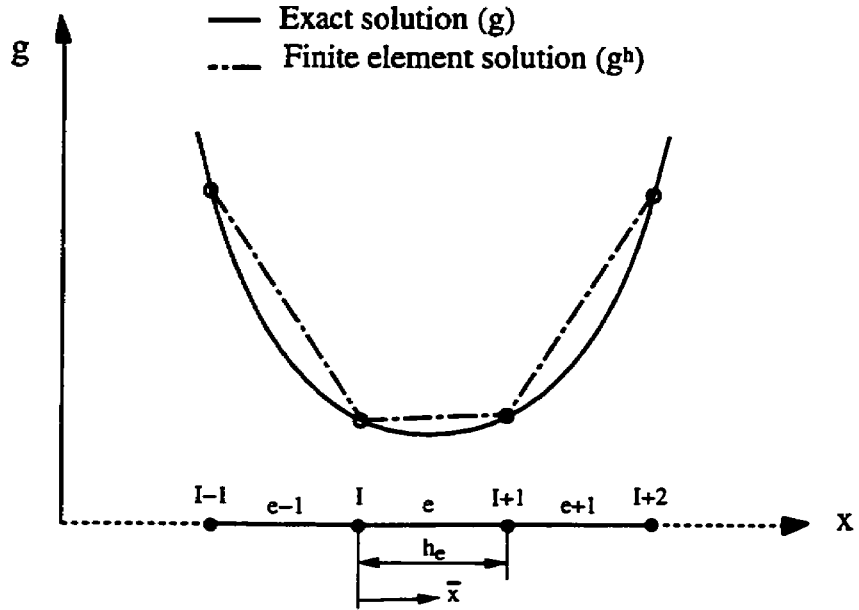


Figure 3.1: Solution as approximated by a piecewise finite element method

tion  $g_e^h$  may be rewritten as

$$g_e^h(\bar{x}) = g_I + \bar{x}g'_I + \frac{\bar{x}h_e}{2}g''_I + \dots \quad (3.4)$$

Provided that the error at the nodes is zero, the exact solution may also be expanded in the neighborhood of the node  $I$  as (Taylor series)

$$g(\bar{x}) = g_I + \bar{x}g'_I + \frac{\bar{x}^2}{2}g''_I + \dots \quad (3.5)$$

The elemental error at any point  $\bar{x}$  is obtained by substituting the two expansions (3.4) and (3.5) into the equation (3.1) and neglecting third order terms, that gives

$$E_e(\bar{x}) = \left( \frac{\bar{x}^2}{2} - \frac{\bar{x}h_e}{2} \right) g''_I, \quad (3.6)$$

which can be seen as a departure of a quadratic interpolation from a linear one.

Following the work of Peraire *et al.* [108], the Root-Mean-Square (*RMS*) interpolation error over an element spanning the interval  $[0, h_e]$  can then be evaluated as

$$\begin{aligned} E_e^{RMS} &= \left\{ \int_0^{h_e} \frac{E_e^2}{h_e} dx \right\}^{1/2} \\ &= \frac{1}{\sqrt{120}} h_e^2 \left| \frac{d^2 g^h}{dx^2} \right|_e. \end{aligned} \quad (3.7)$$

Thus, an edge-based element measure of the interpolation error for this 1-D problem is proportional to the product of the second derivative and the square of the length of the element,  $h_e$ .

An optimal mesh can thus be defined as a mesh in which the *RMS* error is equidistributed over the elements, that is one for

$$h_e^2 \left| \frac{d^2 g^h}{dx^2} \right|_e = C, \quad (3.8)$$

over each element, where  $c$  denotes a user-specified tolerance.

Extending this adaptation criterion to the 2-D case, the second derivative of  $g^h$  is now taken with respect to a given unit vector  $\mathbf{V}$  as follows:

$$\frac{\partial^2 g^h}{\partial \mathbf{V}^2} = \mathbf{V}^T \mathbf{H} \mathbf{V}, \quad (3.9)$$

where  $\mathbf{H}$  represents the Hessian matrix of  $g^h$  and is expressed as:

$$H_{ij} = g_{,ij}^h = \begin{pmatrix} \frac{\partial^2 g^h}{\partial x^2} & \frac{\partial^2 g^h}{\partial x \partial y} \\ \frac{\partial^2 g^h}{\partial y \partial x} & \frac{\partial^2 g^h}{\partial y^2} \end{pmatrix}. \quad (3.10)$$

Since  $g^h$  is linear for each element in the current formulation, the second derivatives vanish. A weak formulation combined with mass lumping can, however, be applied to recover a continuous estimate of the second derivatives. This yields the following expression

$$g_{,ij}^h|_I = \frac{\int_{\Omega_I} g_{,ij}^h \Phi_I d\Omega}{\int_{\Omega_I} \Phi_I d\Omega}, \quad (3.11)$$

where  $\Omega_I$  represents the elements sharing node  $I$ . After integration by parts of equation (3.11), the nodal values of the Hessian reduce to:

$$g_{,ij}^h|_I = \frac{\int_{\Gamma_I} g_{,i}^h \Phi_I n_j d\Gamma - \int_{\Omega_I} g_{,i}^h \Phi_{I,j} d\Omega}{\int_{\Omega_I} \Phi_I d\Omega}. \quad (3.12)$$

If the Hessian matrix, given by the equation (3.10), is diagonalized as

$$\mathbf{H} = \mathbf{R}(\alpha) \Lambda \mathbf{R}^T(\alpha), \quad (3.13)$$

$\Lambda$  would be the diagonal matrix of eigenvalues of  $\mathbf{H}$  and  $\mathbf{R}$  would be the corresponding matrix of the eigenvectors. The transformation  $|\Lambda|$  can be interpreted as a scaling in the axes directions and  $\mathbf{R}$  as a rotation with angle  $\alpha$ , that the eigenvector corresponding to the smallest eigenvalue,  $\lambda_1$ , makes with the  $x_1$ -axis.

In order to transform it into a symmetric positive-definite matrix, the Hessian can then be modified by taking the absolute value of its eigenvalues [119], resulting in:

$$\overline{\mathbf{H}} = \mathbf{R}(\alpha) |\Lambda| \mathbf{R}^T(\alpha) = \mathbf{S}(\alpha) \mathbf{S}^T(\alpha), \quad (3.14)$$

where  $\mathbf{S} = \mathbf{R} \sqrt{|\Lambda|}$ . The transformation  $\mathbf{S}$ , for a unit circle for example, would be an ellipse, rotated through an angle  $\alpha$ , whose semi-major and -minor axes are reciprocals of

the square roots of the eigenvalues  $|\lambda_1|$  and  $|\lambda_2|$ , respectively (see figure 3.2). Therefore, one may obtain a directionally stretched grid by mapping a uniform mesh using the transformation  $S$ .

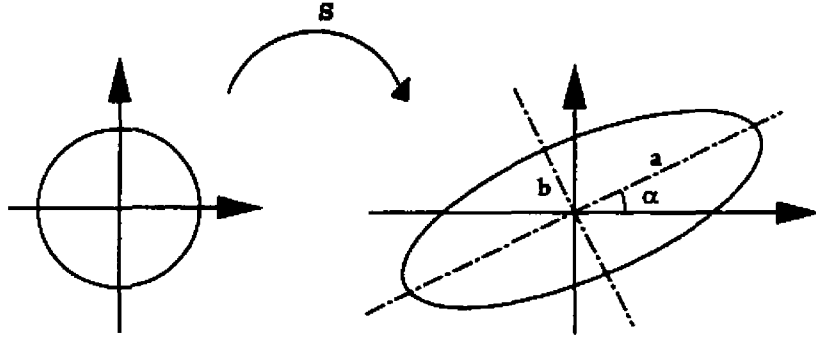


Figure 3.2: Transformation of a unit circle by  $S$  where  $a = |\lambda_1|^{-1/2}$  and  $b = |\lambda_2|^{-1/2}$ .

By introducing the modified Hessian  $\bar{H}$ , the above second derivative in any direction  $V$  is bounded by:

$$\left| \frac{\partial^2 g^h}{\partial V^2} \right| = |V^T \bar{H} V| \leq V^T \bar{H} V. \quad (3.15)$$

Hence, the 1-D adaptation criterion may be rewritten for the 2-D problems as

$$h^2 V^T \bar{H} V = C. \quad (3.16)$$

In Peraire's approach [108], the *RMS* error is equidistributed in the direction of the eigenvectors where  $h = h_k$ , with  $k = 1, 2$ , are two local spacings and  $V = V_k$  are the two unit eigenvectors of the  $\bar{H}$  matrix. Accordingly, the optimal mesh criterion (3.16) simplifies to:

$$h_k^2 |\lambda_k| = C \quad \text{with } k = 1, 2. \quad (3.17)$$

This equation serves to compute two local spacings,  $h_k = \sqrt{C/|\lambda_k|}$ , in two orthogonal

directions, at any point in the domain. Then, a new adapted grid is regenerated based on these parameters and principal directions of  $\bar{\mathbf{H}}$ .

In the current approach the error is equidistributed over the edges of elements where  $h = \|\mathbf{x}_J - \mathbf{x}_I\|$  represents the Euclidean length of an element edge  $[\mathbf{x}_I, \mathbf{x}_J]$  and  $\mathbf{V} = (\mathbf{x}_J - \mathbf{x}_I)/h$  is the unit vector which supports the edge. The equation (3.16) takes the following form:

$$(\mathbf{x}_I - \mathbf{x}_J)^T \bar{\mathbf{H}} (\mathbf{x}_I - \mathbf{x}_J) = C. \quad (3.18)$$

An optimal mesh is thus defined as the mesh in which the length of all edges, in the defined metric  $\bar{\mathbf{H}}$ , is equal to  $\sqrt{C}$ .

Since  $\bar{\mathbf{H}}$  is a function of the space coordinates, the LHS term of the equation (3.18) defines a Riemannian metric. Elementary differential geometry dictates that the length of an edge  $[\mathbf{x}_I, \mathbf{x}_J]$  in this metric is defined by:

$$d(\mathbf{x}_I, \mathbf{x}_J) = \int_0^1 \sqrt{(\mathbf{x}_I - \mathbf{x}_J)^T \bar{\mathbf{H}}(l) (\mathbf{x}_I - \mathbf{x}_J)} \, dl. \quad (3.19)$$

The matrix  $\bar{\mathbf{H}}$  is computed and stored on a background mesh, and thus the value of  $\bar{\mathbf{H}}$  at any position of the domain can be interpolated during the adaptive process on this mesh. The edge-based error estimate can then be numerically evaluated from equation (3.19) for each edge of an element.

### 3.3 Mesh Movement Scheme

The adaptive strategy modifies the grid under the guidance of the error estimate to improve the quality of the numerical solution. The proposed strategy relies on an  $r$ -method illustrated in Figure 3.3, wherein the mesh may be viewed as a network of springs whose stiffness constants represent the edge-based error estimate. The position of the central grid vertex may be obtained from the solution of an energy minimization problem. For each

vertex  $I$ :

$$\min_{\mathbf{x}_I} P_I = \min_{\mathbf{x}_I} \sum_J (\mathbf{x}_I - \mathbf{x}_J)^2 k_{IJ}, \quad (3.20)$$

where  $P_I$  denotes the potential energy of the four active springs sharing a node  $I$ , and  $k_{IJ}$  are their associated stiffness constants. These constants may then be specifically written as the scaled value of the associated edge in the Riemannian metric,

$$k_{IJ} = \frac{d(\mathbf{x}_I, \mathbf{x}_J)}{\|\mathbf{x}_I - \mathbf{x}_J\|}, \quad (3.21)$$

where  $\|\cdot\|$  indicates the Euclidean norm and  $d(\mathbf{x}_I, \mathbf{x}_J)$  is the length of the edge  $[\mathbf{x}_I, \mathbf{x}_J]$  in the Riemannian metric defined by equation (3.19).

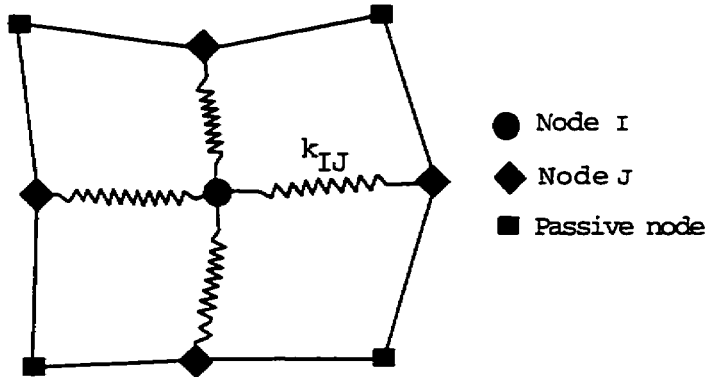


Figure 3.3: Spring analogy for a patch of elements

After simplification, equation (3.20) reduces to the system describing the equilibrium state of a spring network

$$\sum_J (\mathbf{x}_I^{m+1} - \mathbf{x}_J^{m+1}) k_{IJ}^m = 0, \quad (3.22)$$

where  $k_{IJ}$  is lagged at the previous iteration  $m$ . The position of the vertex  $I$  is updated

according to the expression:

$$\mathbf{x}_I^{m+1} = \mathbf{x}_I^m + \omega \frac{\sum_J (\mathbf{x}_J^m - \mathbf{x}_I^m) k_{IJ}^m}{\sum_J k_{IJ}^m}, \quad (3.23)$$

where  $\omega$  is a relaxation factor. The convergence of this scheme can be enhanced by using a Gauss-Seidel algorithm with the latest values of  $\mathbf{x}_J$  and  $k_{IJ}$  in equation (3.23).

In this procedure, the boundary nodes are also free to move along their respective curves. The same algorithm as for the internal nodes is applied to compute their new positions, but they are projected back to their corresponding boundary curves.

The grid adaptation procedure may be summarized in the following steps:

- read a background mesh and the corresponding solution
- compute  $\bar{H}$  on the background mesh
- current mesh is initialized by an initial mesh
- move the nodes of the current mesh as follows:

DO  $m = 1, MAXITER$

DO  $inod = 1, NNODE$

DO  $iedge = 1, NEDGE$

- determine  $\bar{H}$  by interpolating on the background mesh
- compute spring constants by numerical integration of Eq. (3.21)

ENDDO

- find new position of  $inod$
- check quality of resulting elements sharing  $inod$
- move  $inod$  to its new position

ENDDO

If ( $MAXDISP .LE. tolerance$ ) exit the  $m$  loop

ENDDO

where  $NEDGE$  represents the number of edges sharing the node  $i_{nod}$  and  $MAXDISP$  is the maximal displacement of all nodes for a particular iteration  $m$ .

In the general case, the background mesh serves only to compute and store the error estimate and hence could be different from the initial mesh. For the first few cycles of adaptation, one can thus develop a crude error estimate on a coarse mesh to adapt a finer grid.

Both flow solver and grid adaptation procedures are placed in an iterative loop which is repeated until the lowest value of a user-specified artificial dissipation coefficient is reached. In the following, each iteration of this loop will be called an adaptive cycle or level and is identified by an alphabetical letter.

## 3.4 Numerical Results

For all the test cases investigated in this section, the background mesh is taken to be identical to the adapted mesh of the previous cycle for all adaptation cycles.

### 3.4.1 Analytical test case

Since the grid adaptation procedure contains some new aspects, it is important to investigate its effectiveness on an analytical test case. The aim of the first example is, therefore, to demonstrate the capability of this procedure to equidistribute the interpolation error of a given function over the edges. A function, with strong gradients, of the form:

$$g(x_1, x_2) = \arctan [10^3(x_1^4x_2^4 - 0.25)] \quad (3.24)$$

is chosen over the domain  $[0,2] \times [0,1]$ .

The initial mesh (35x20 nodes) with the corresponding iso-contours of  $g$  are presented in Figs. 3.4-(a) and 3.4-(á). After 300 iterations of the mesh movement scheme, the adapted

mesh shown in Fig. 3.4-(b) is obtained. This mesh is resulting from the strong migration of nodes from smoother regions to regions with steep variations. As illustrated in Fig. 3.4-(b), the adapted mesh permits a vastly improved representation of the function  $g$ . It also eliminates the step forms of the iso-contours that are observed in Fig. 3.4-(a) by a proper alignment of the elements.

Fig. 3.5 represents a histogram of the number of edges versus the error over these edges. In the ideal case, all the edges would have the same error. In practice, a nearly Gaussian distribution is obtained where the maximum error is reduced five-fold. This demonstrates the ability of the mesh movement scheme to equidistribute the error over the edges.

The plot of the average value and the  $L_\infty$  norm of node displacements in Fig. 3.6 shows that the correction of position vertices drops by 2 orders of magnitude after 700 iterations. In contrast, the  $L_\infty$  norm of the edge error, Fig. 3.7, asymptotically stalls at the value of 0.55 after 170 iterations meaning that no additional maximum-edge-error improvement is possible. In this test case, no relaxation operation is needed.

### 3.4.2 Hypersonic flow over a cylinder

In this example, the methodology is applied to a hypersonic flow over a cylinder (see Fig. 3.8) at a freestream Mach number of 6 and zero angle of attack. The initial mesh, shown in Fig. 3.9-(a), is composed of 33x53 nodes distributed uniformly in both radial and circumferential directions. The Mach number contours of the corresponding partially-converged solution are depicted in Fig. 3.9-(a). The final adapted mesh in Figs. 3.10-(f) requires 5 levels of adaptation. The corresponding flow field contours, Fig. 3.10-(f), demonstrate the benefits of the grid adaptation in resolving a detached bow shock. Here, the density solution is the flow variable used for the error estimate.

Fig. 3.11 illustrates the enhancement of the Mach number distribution on the stagnation line with grid adaptation cycles. The enhancement of the node density in the shock region

with a more appropriate alignment of the elements along the shock, drastically diminishes the amount of artificial dissipation needed in stabilizing the flow solver.

The present artificial dissipation model<sup>1</sup>, also referred to as the conservative dissipation model, is compared in Fig. 3.12 to the non-conservative dissipation model that is based on Laplacians of the primitive variables  $[\rho, v_1, v_2, e]$ , by plotting the total enthalpy along the stagnation line. One may clearly observe that only the conservative dissipation model can conserve the total enthalpy and therefore have the ability of recovering isoenthalpic flow solutions as a particular case.

The profiles of temperature and pressure along the stagnation streamline are compared in Fig. 3.13 to the results of Wada *et al.* [125]. Overall, this figure reveals good agreement between the adapted solution and Wada's results. Slight discrepancies in pressure distributions are, however, observed near the wall due to the different manner of implementing the wall boundary conditions. It must be pointed that Wada's solution was predicted on a finer grid with an Advection Upwind Splitting Method (AUSM), proven superior to most standard flux-difference splitting and flux-vector splitting schemes.

The convergence history of both flow solver and adaptation grid procedures are presented in Figs. 3.14 and 3.15, where the jumps in the curves represent the beginning of each new artificial dissipation cycle. For a given value of the artificial dissipation coefficient, the  $L_2$  norm of the flow residual, at that cycle, is lowered by three orders of magnitude and then the mesh nodes are displaced 500 times. Fig. 3.14 shows that the use of a local time stepping technique, with high CFL number of 350, permits to reach machine accuracy in relatively small number of iterations. A relaxation factor of 0.6 is used in the mesh movement scheme.

In order to study the influence of the selected flow variable used in the error estimate

---

<sup>1</sup>This model is based on Laplacians of the modified conservative variables,  $[\rho, \rho v_1, \rho v_2, \rho h]$ .

on the quality of solutions, a comparative study is conducted for density (1), velocity (2) and the Mach number (3). Fig. 3.16 shows that an adaptation method based on density or velocity variable results in almost the same adapted grid while the Mach number in plot (3) tends to concentrate less nodes in the stagnation region. The plot of the adapted solution for the three error estimates in term of Mach number contours in Fig. 3.17 reveals almost no differences between them, except at the exit of case (2) where tiny oscillations may be observed. Fig. 3.18 displays the same comparison in terms of pressure contours where all error estimates produce nearly identical solutions.

It should be noted that all these observations are valid for the Euler flows and cannot be extended to other CFD problems such as viscous flows. For inviscid flows, an adaptation procedure is mainly applied to permit a better resolution of shocks. Since this physical phenomenon is felt by all flow variables, the adapted solution would be almost independent with respect to these variables. So the selection of a flow variable is mainly motivated by its smoothness and this justifies the use of density in most mesh adaptation literature.

Viscous flows, however, contain additional physical phenomena, such as boundary layers and vortices, that should also be efficiently resolved. It is then important that the used flow variable should be furthermore sensitive to the presence of these phenomena and permits an appropriate evaluation of the error in their regions. For these reasons, velocity or Mach number solution is usually chosen as the key variable in the evaluation of the error estimates.

### 3.4.3 Supersonic compression corner

The second test case is that of flow at Mach 3 over a  $16^\circ$  ramp (see Fig. 3.19). This example tests certain features of the algorithm, including the resolution of the oblique shock and its proper angle.

The initial coarse mesh of  $44 \times 27$  nodes is shown in Fig. 3.20-(a) and the resulting den-

sity contours are presented in Fig. 3.20-(a). After 5 levels of adaptations, the resulting grid and solution are depicted in Figs. 3.21-(f) and -(f), respectively. A comparison of Figs. 3.20-(a) and 3.21-(f) demonstrates the important role of the grid adaptation in capturing a sharp shock at the correct angle. The final solution is also illustrated in the form of pressure and Mach number contours in Figs. 3.22 and Figs. 3.23.

A magnification of the mesh in the shock region in Fig. 3.24 shows that the quadrilateral elements are oriented in the direction of the shock, with aspect ratios as high as 50. Fig. 3.25 clearly illustrates the superiority of the adapted solution in approximating the exact solution. In fact, the use of an appropriate grid also allows the reduction of the artificial dissipation coefficient by a factor of 10. The convergence history of the flow solver is presented in Fig. 3.26 and the node displacement convergence of the adaptive procedure is displayed in Fig. 3.27.

### 3.4.4 Hypersonic flow over a double ellipse

In this test case, a double ellipse profile is placed into a Mach 8 flow at  $30^\circ$  angle of attack. Since it was introduced in the Workshop on Hypersonic Flows for Reentry Problems in 1990 [1], this benchmark has proven a great challenge for testing compressible flow solvers. As depicted in Fig. 3.28, the flow field is characterized by a strong detached shock wave followed by a moderate canopy shock. Therefore, the use of standard flow solvers on a uniform grid tends to produce smeared shocks.

The computations were initiated on  $45 \times 124$  (5580) grid nodes, Fig. 3.29-(a), and the corresponding solution is shown in Fig. 3.29-(a). The adapted grid, displayed in Fig. 3.30-(g), is obtained after 6 levels of adaptations. The adapted solution is presented in Fig. 3.30-(g) and it can be clearly seen that the detached and canopy shocks are well resolved. It can also be observed that the canopy shock is not captured in the first cycles of adaptations due to the inadequacy of the grid.

The body pressure coefficient distributions,  $C_p$ , of initial and adapted solutions are compared to Chalot's results [24] in Fig. 3.31. This plot demonstrates the important role of the adapted grid in shock capturing through mesh alignment and the ensuing reduction of the required artificial dissipation in the flow solver. Chalot's computation was carried out by a FEM on an adapted triangular mesh of 6721 nodes.

As displayed in Fig. 3.32, the full convergence of the flow solver requires 150 iterations with a CFL number of 300. The convergence history of the adaptation procedure is depicted in Fig. 3.33 for a relaxation factor of 0.45. In addition, 700 iterations are used for each adaptation cycle.

# **FIGURES**

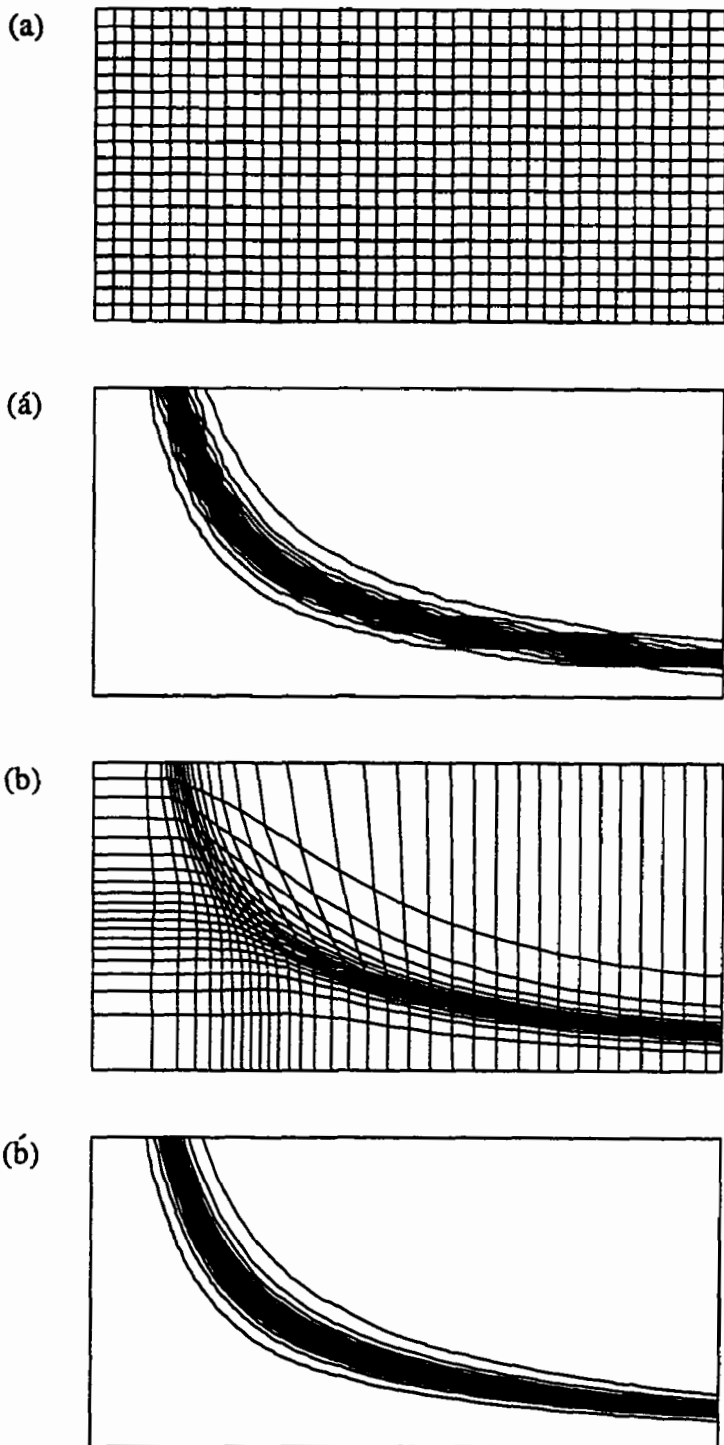


Figure 3.4: Initial (a) and adapted (b) meshes and the corresponding iso-contours, (á) and (b), of  $g$

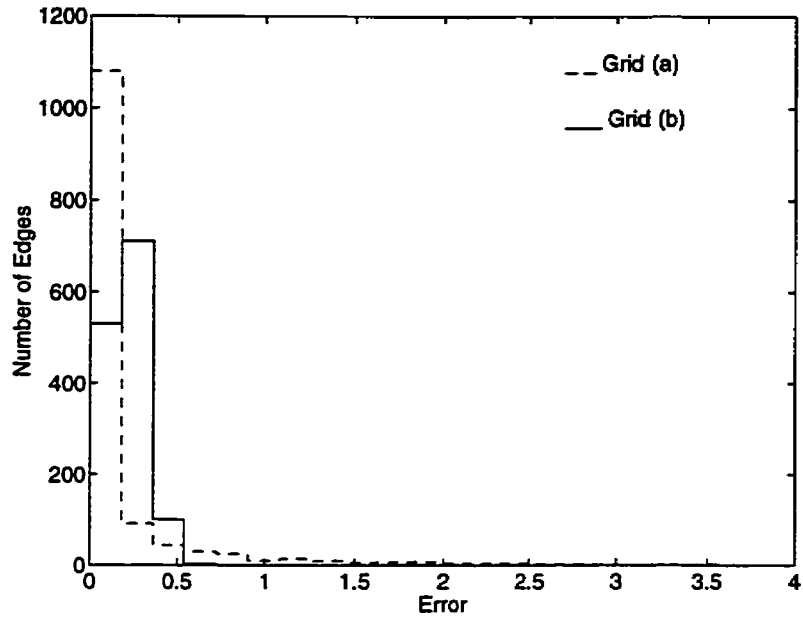


Figure 3.5: Histogram of the error over the edges

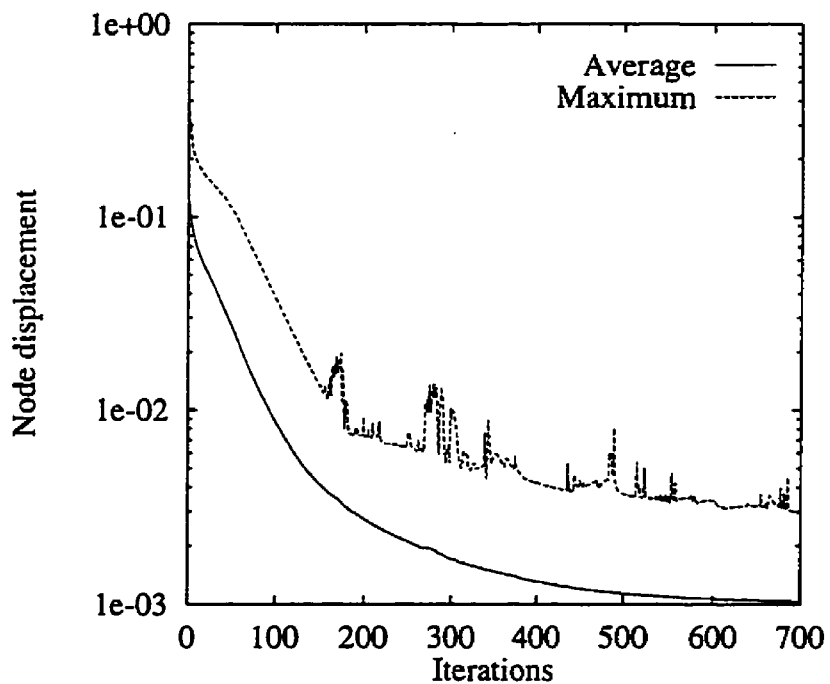


Figure 3.6: Node-displacement convergence history

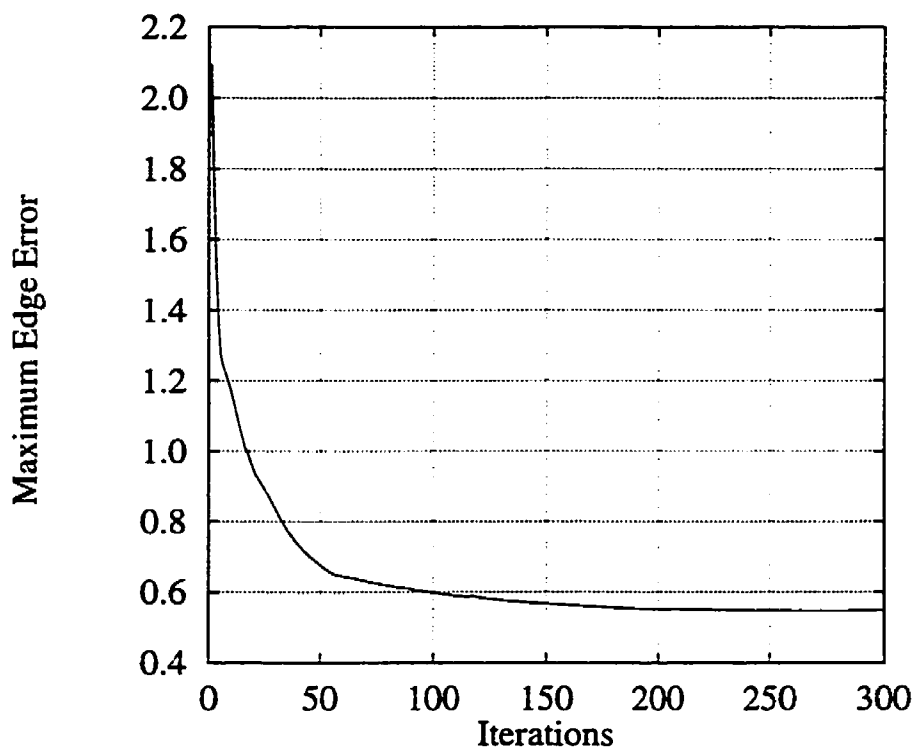


Figure 3.7: Maximum edge-error convergence history

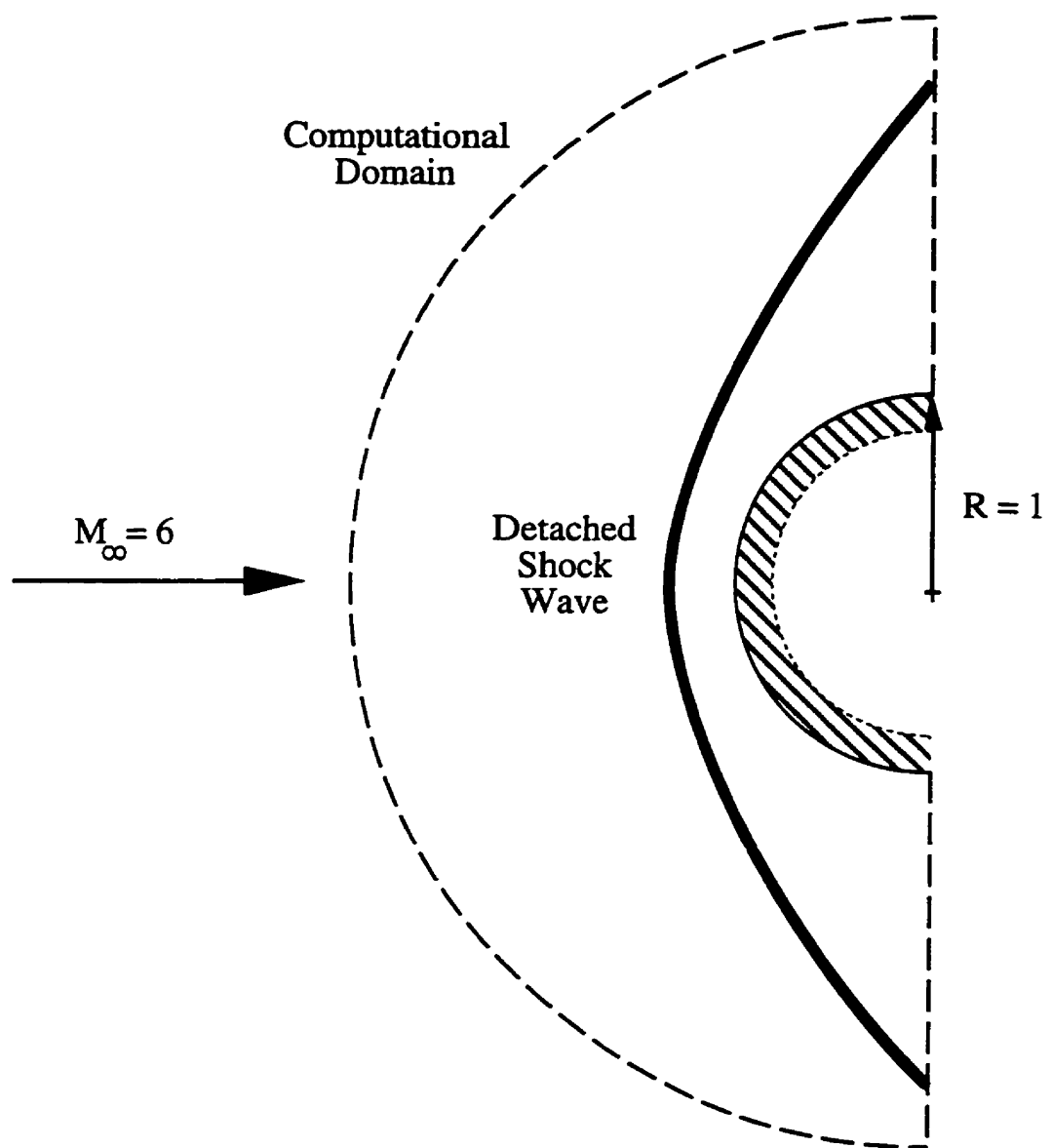


Figure 3.8: Definition of the Mach 6 flow over a half cylinder test case

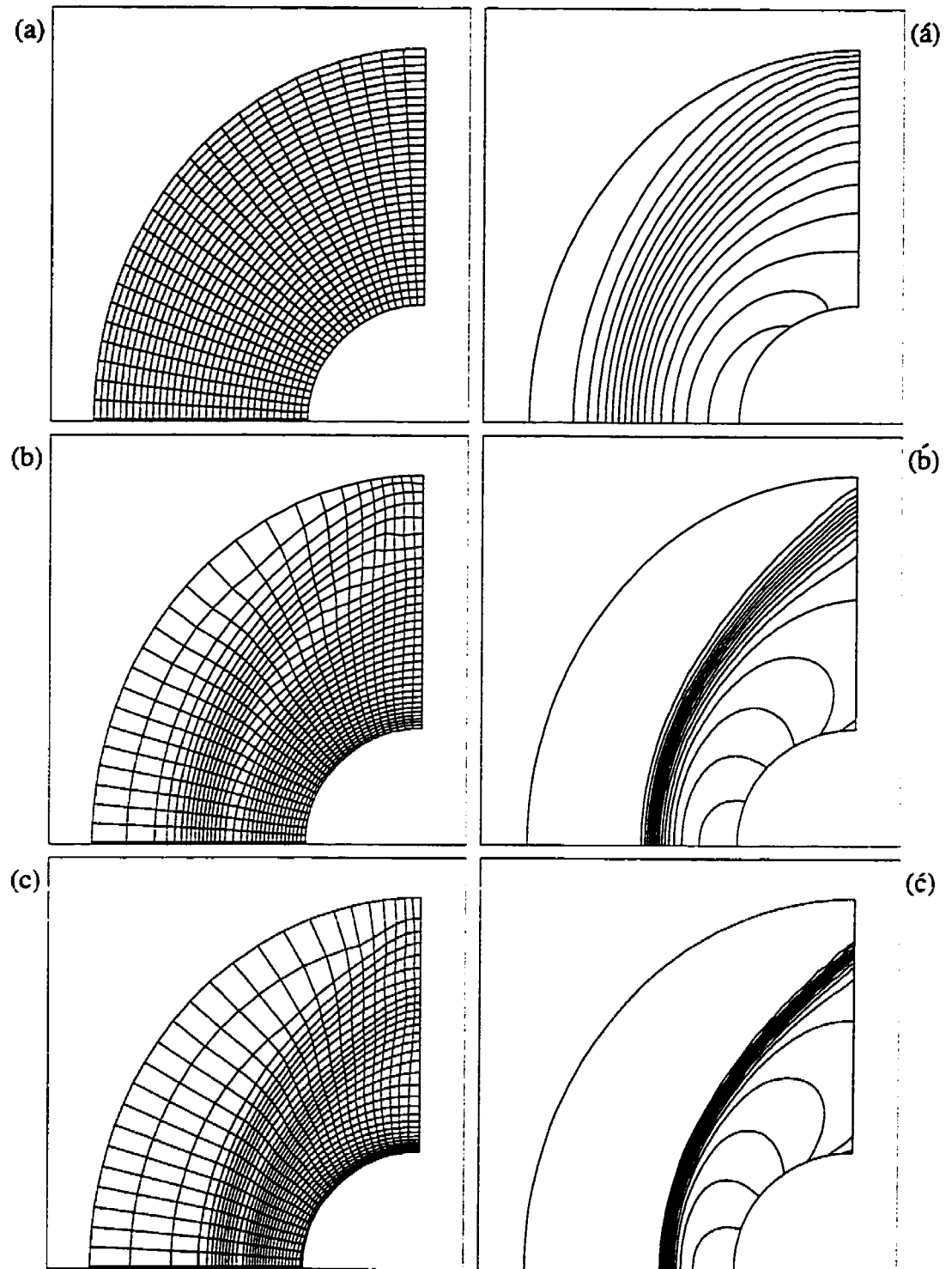


Figure 3.9: Adapted grids and the corresponding Mach number contours for cycles (a-c)

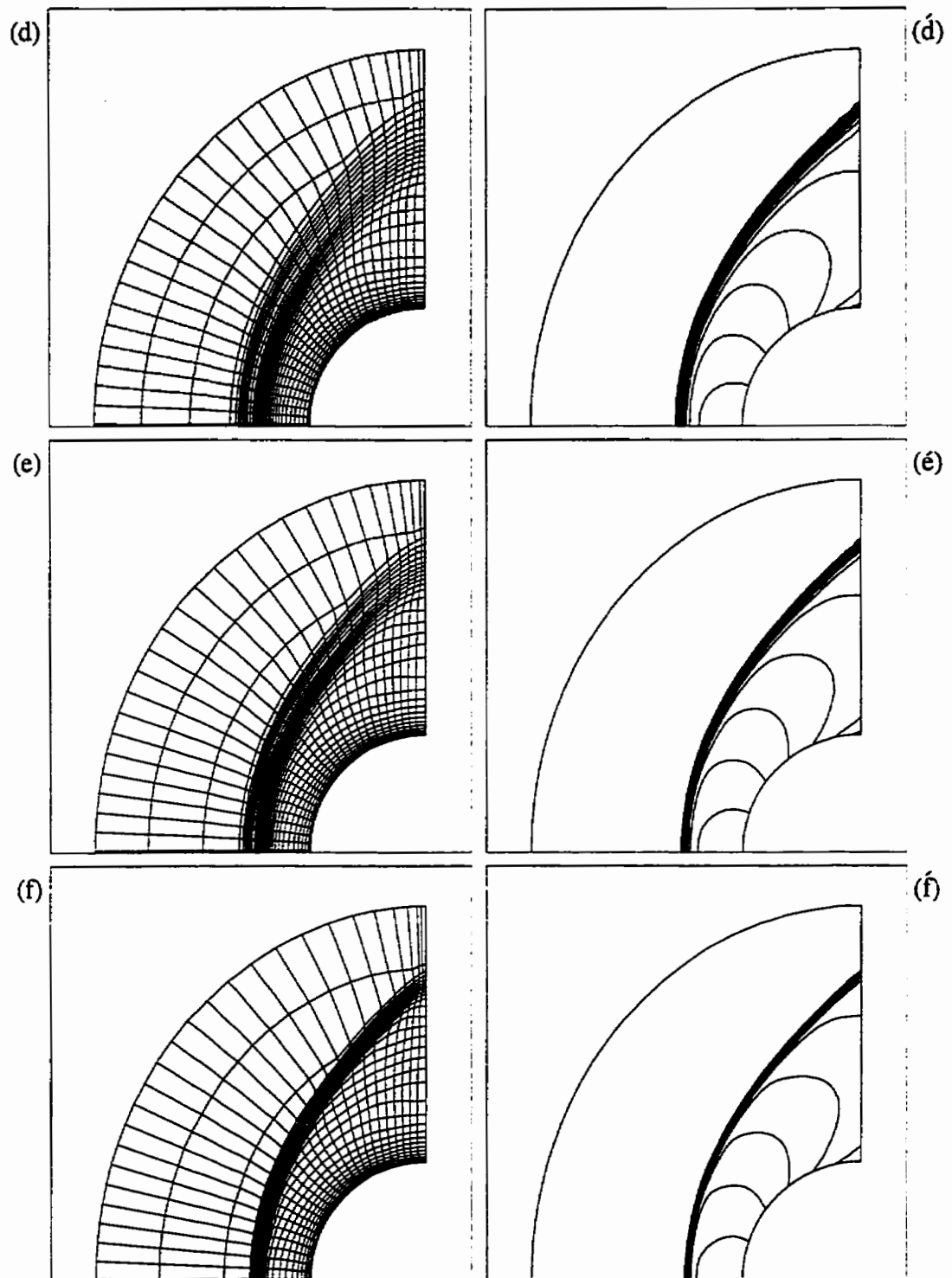


Figure 3.10: Adapted grids and the corresponding Mach number contours for cycles (d-f)

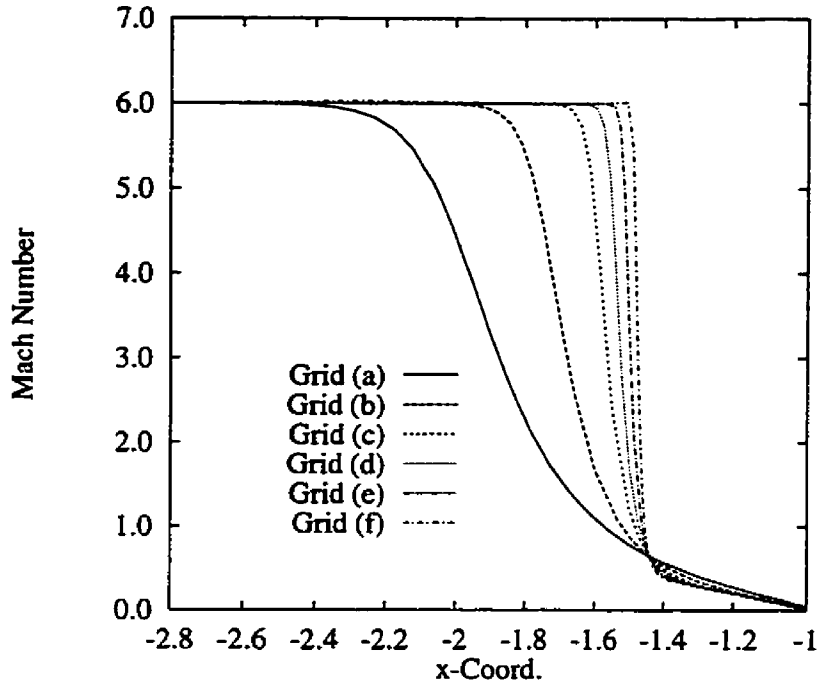


Figure 3.11: Enhancement of the Mach number distribution on the stagnation line with grid adaptation cycles

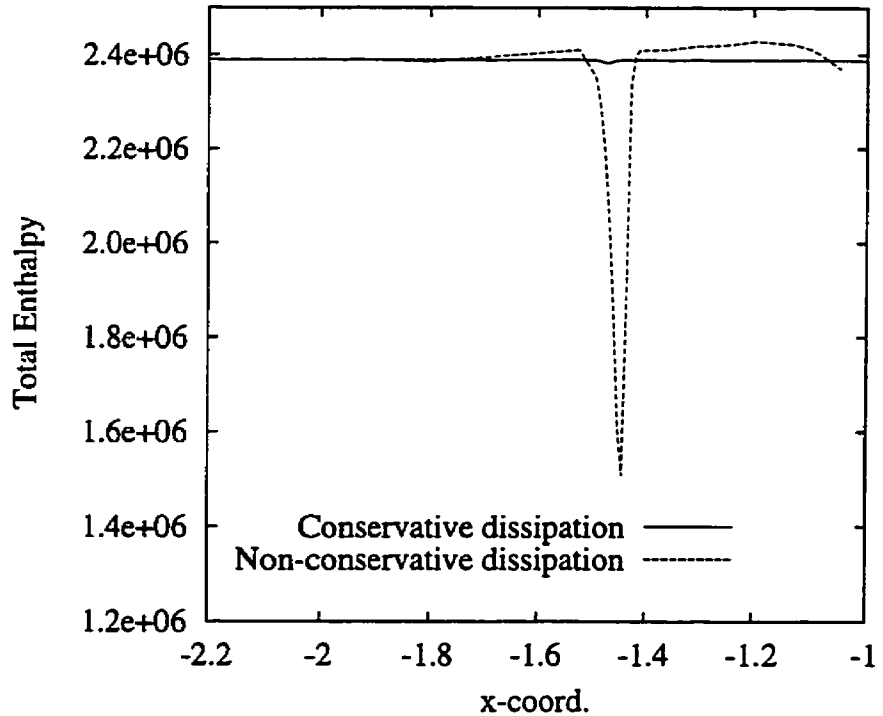


Figure 3.12: Total enthalpy distributions for conservative and non-conservative artificial dissipations models.

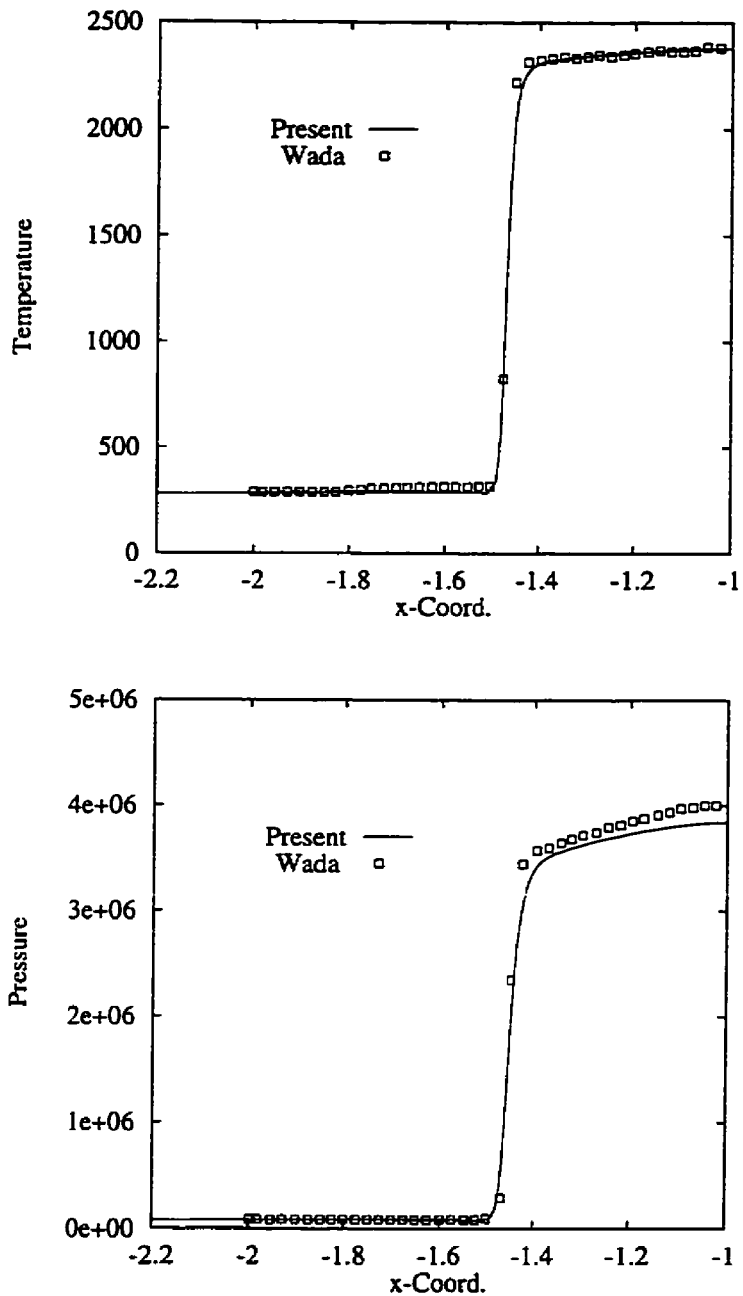


Figure 3.13: Comparison of the present approach, on the stagnation line, to other numerical results

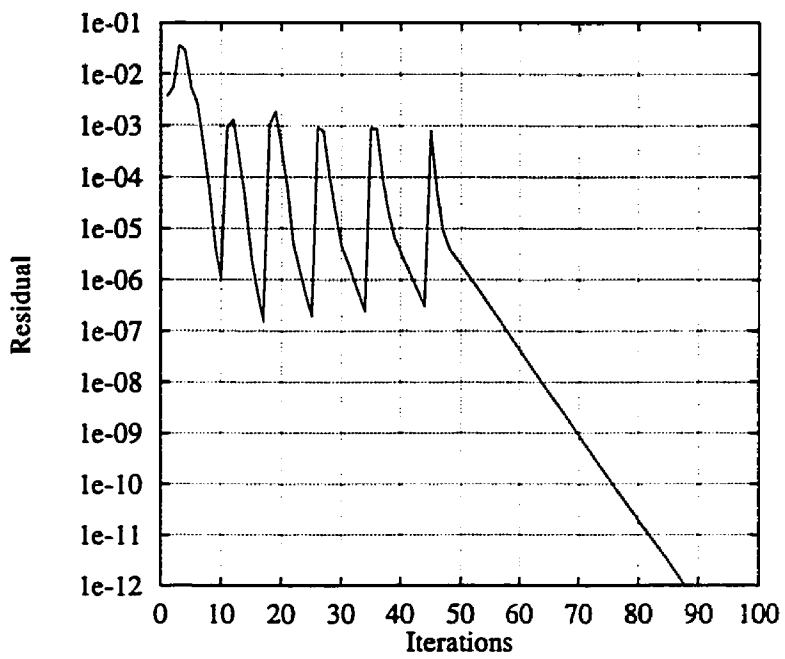


Figure 3.14: Convergence history of the flow solver

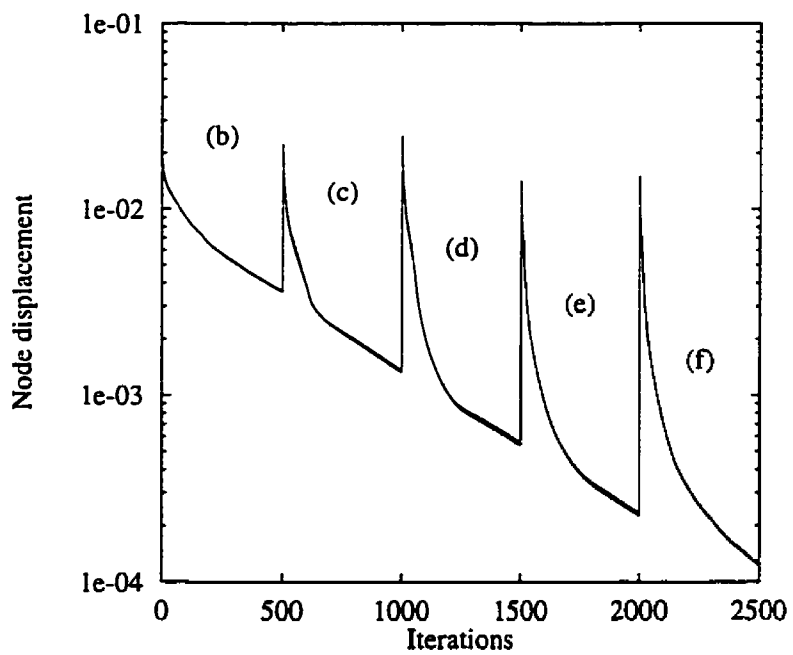


Figure 3.15: Convergence history of the adaptation procedure

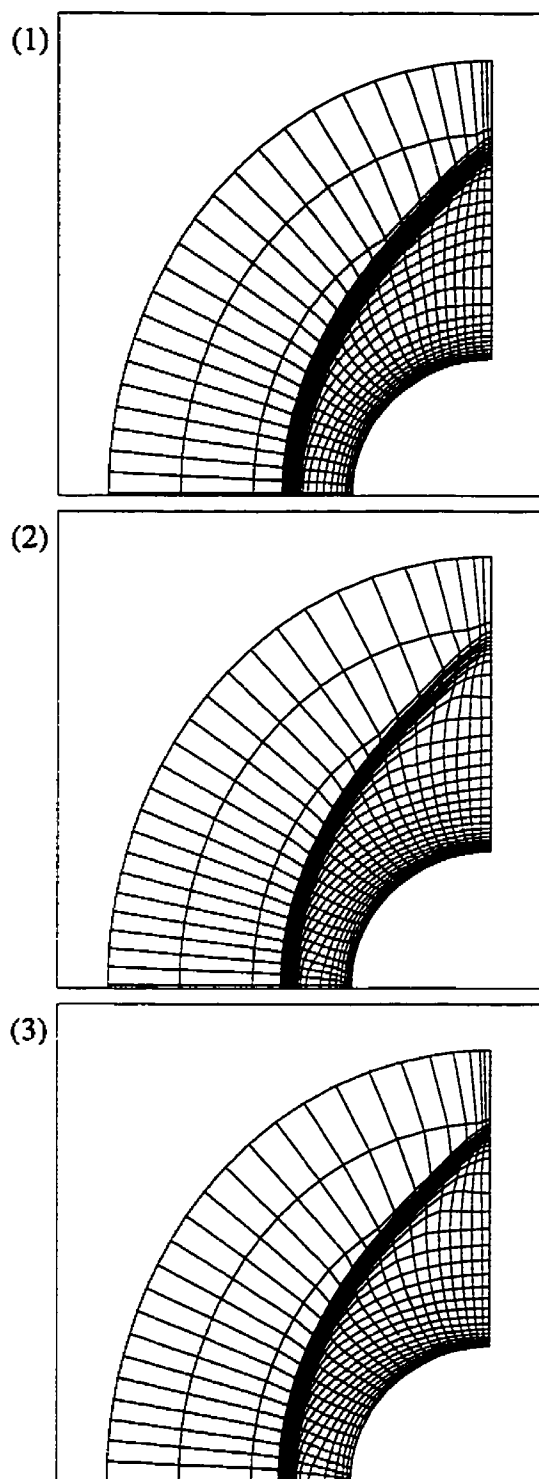


Figure 3.16: Comparison between adapted grids for error estimate based on variables: (1) density, (2) velocity, (3) Mach number

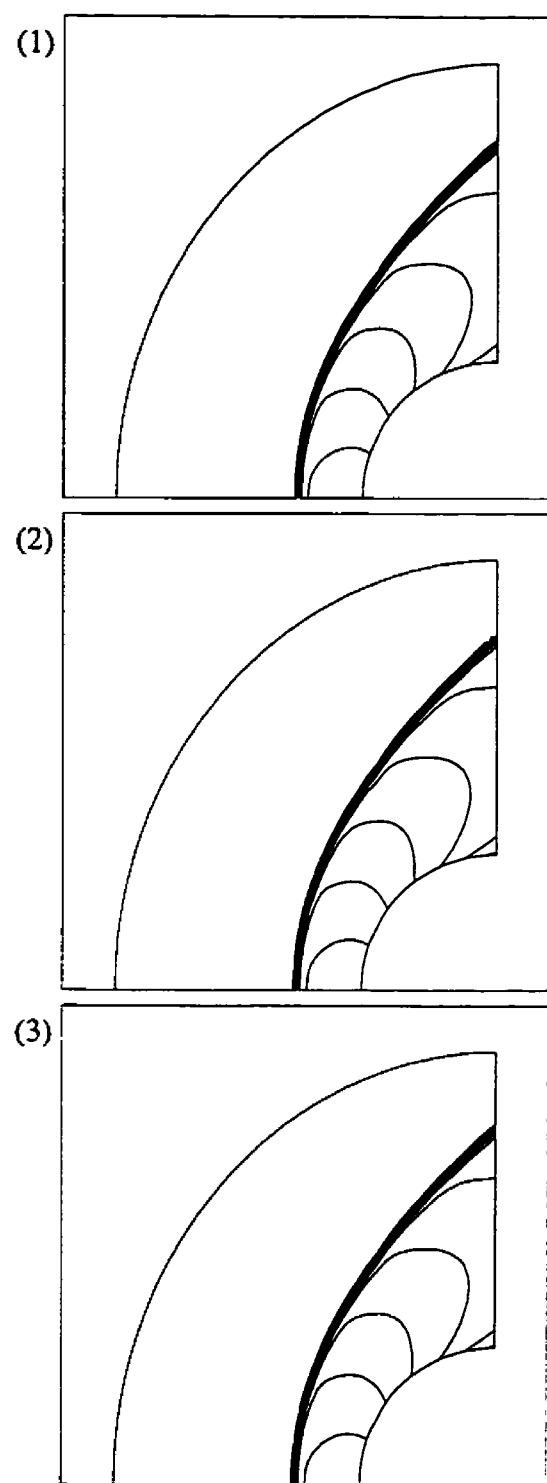


Figure 3.17: Comparison between Mach number contours for error estimate based on variables: (1) density, (2) velocity, (3) Mach number

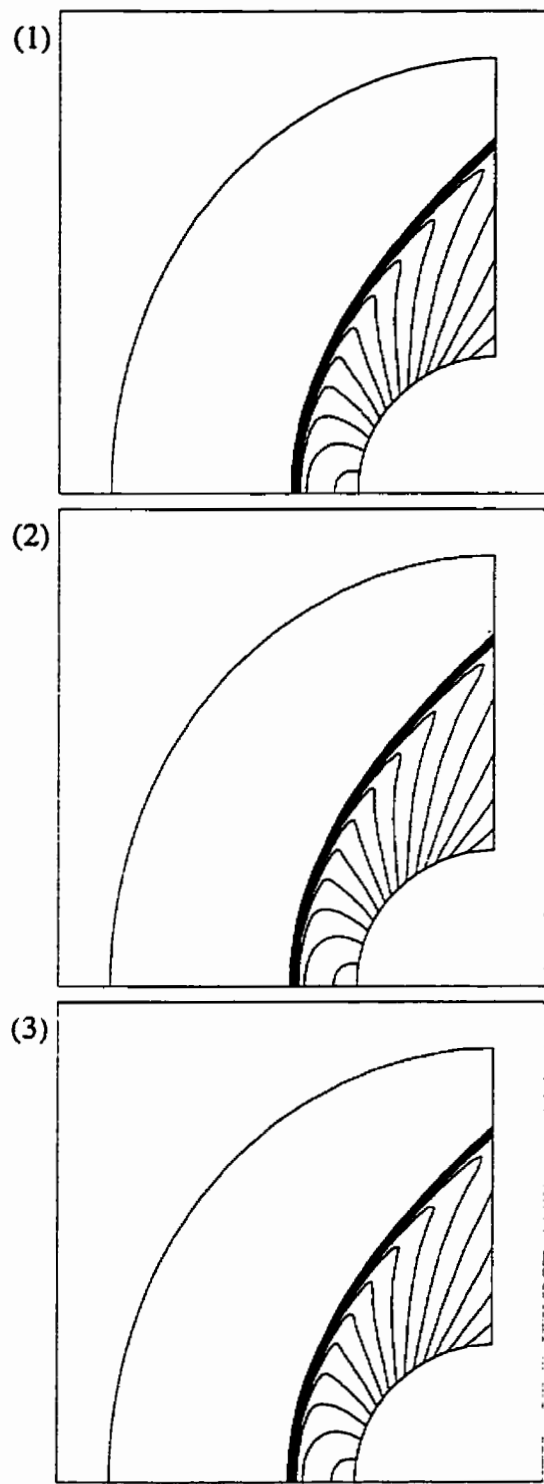


Figure 3.18: Comparison between pressure contours for error estimate based on variables: (1) density, (2) velocity, (3) Mach number

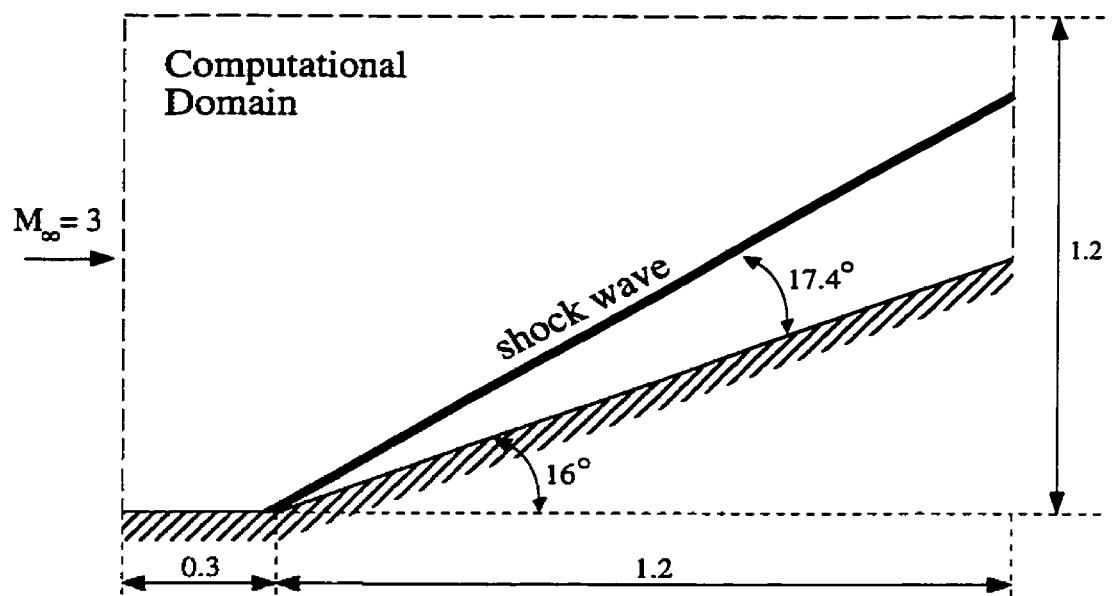


Figure 3.19: Definition of compression corner test case

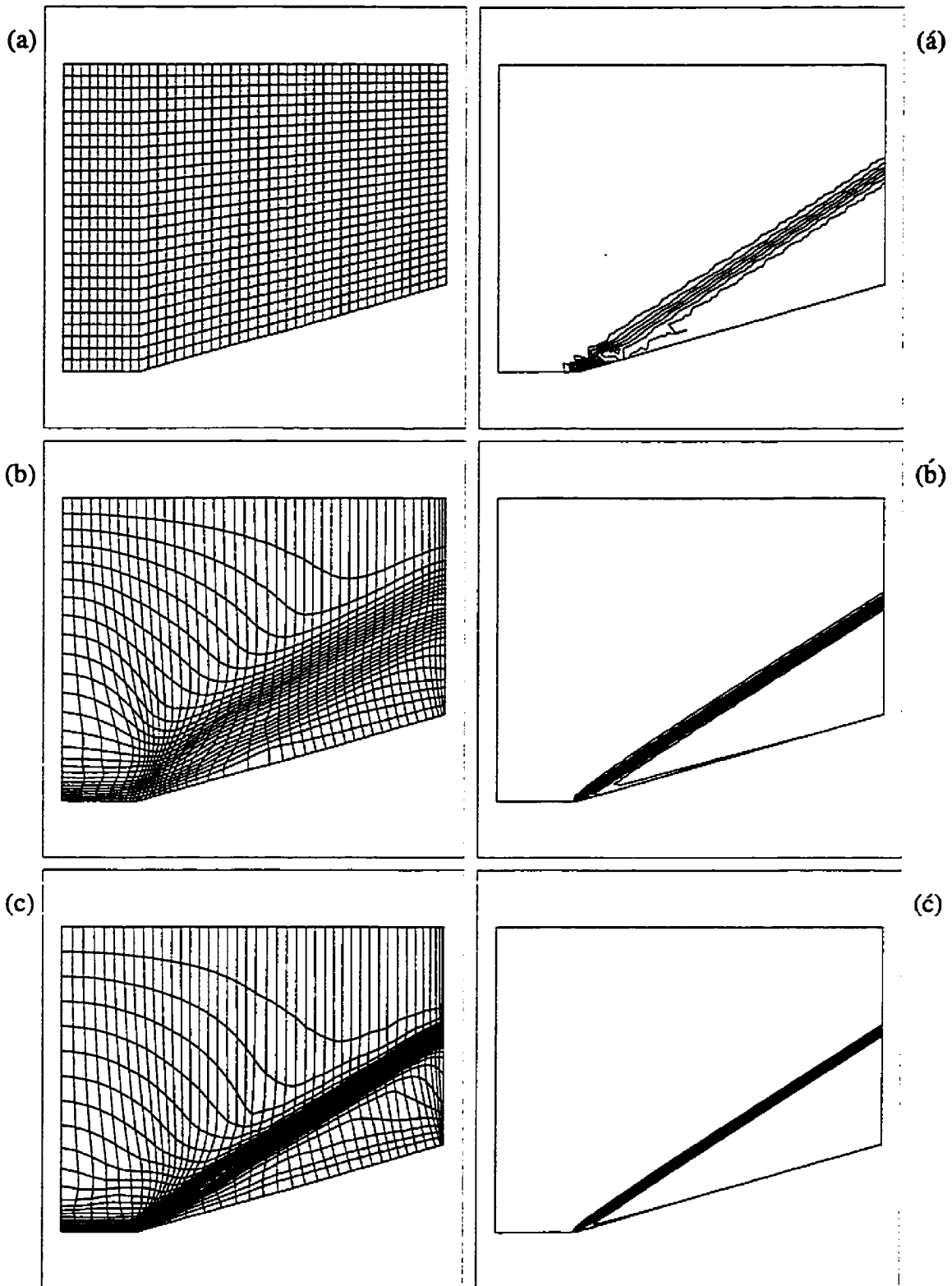


Figure 3.20: Adapted grids and the corresponding density contours for cycles (a-c)

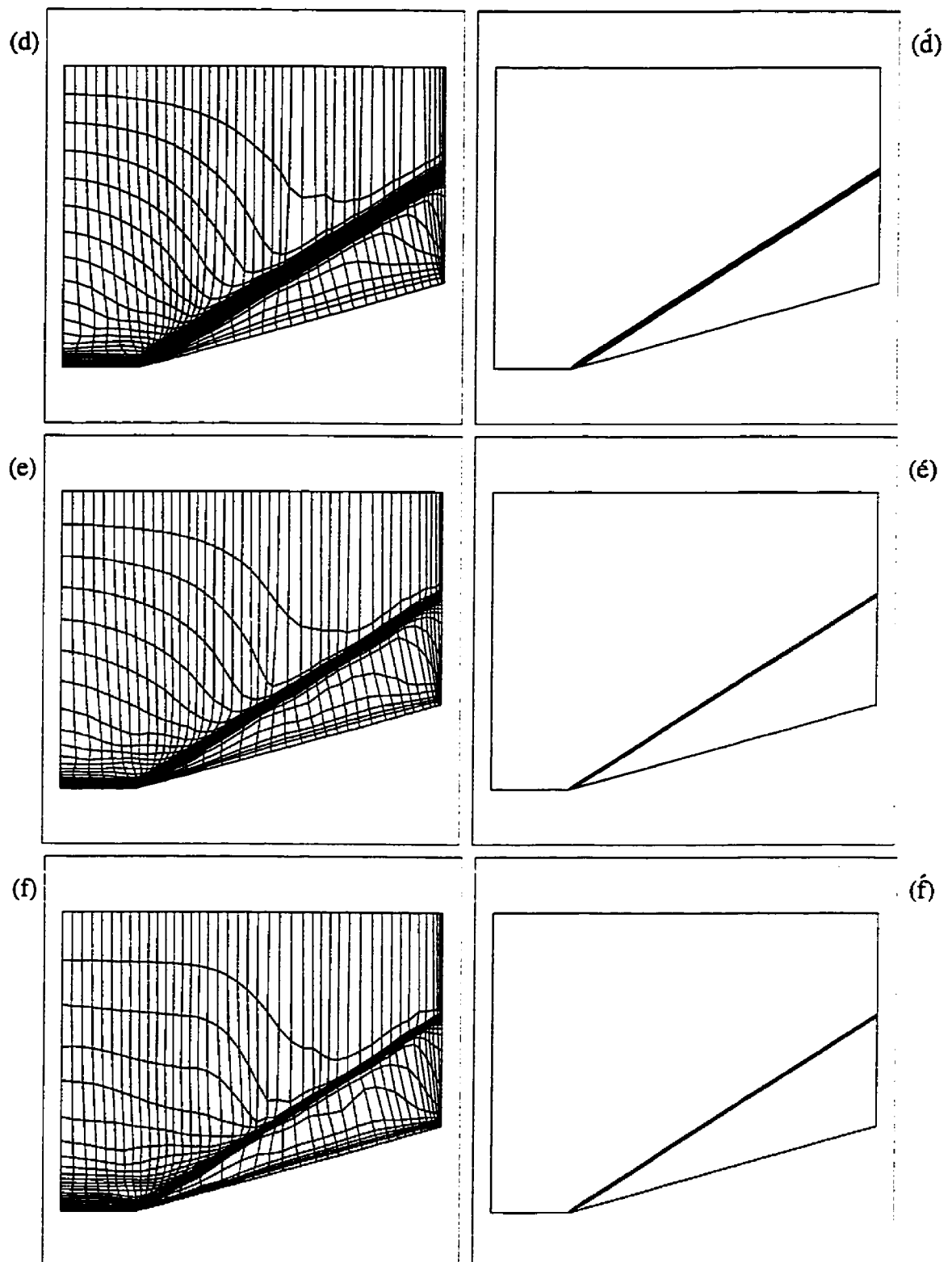


Figure 3.21: Adapted grids and the corresponding density contours for cycles (d-f)

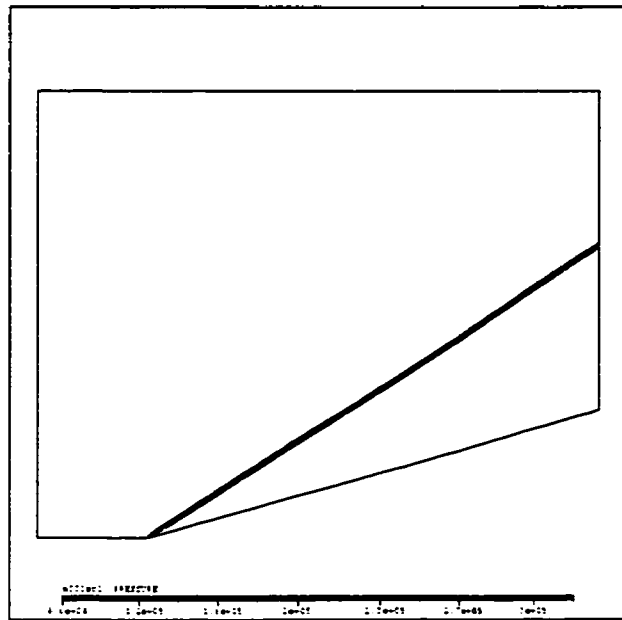


Figure 3.22: Pressure contours

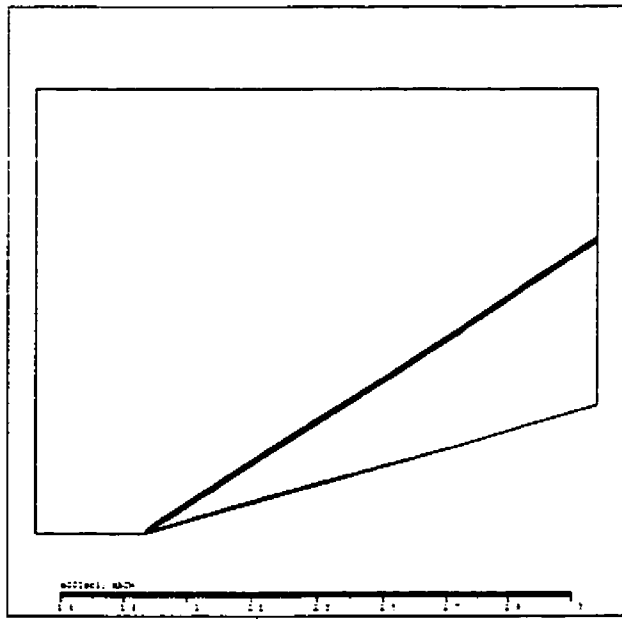


Figure 3.23: Mach number contours

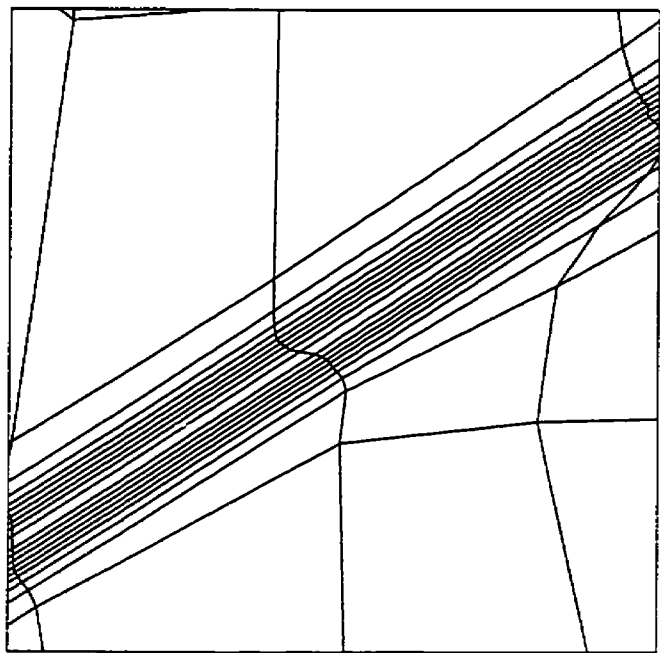


Figure 3.24: Magnification of the adapted grid in the shock region

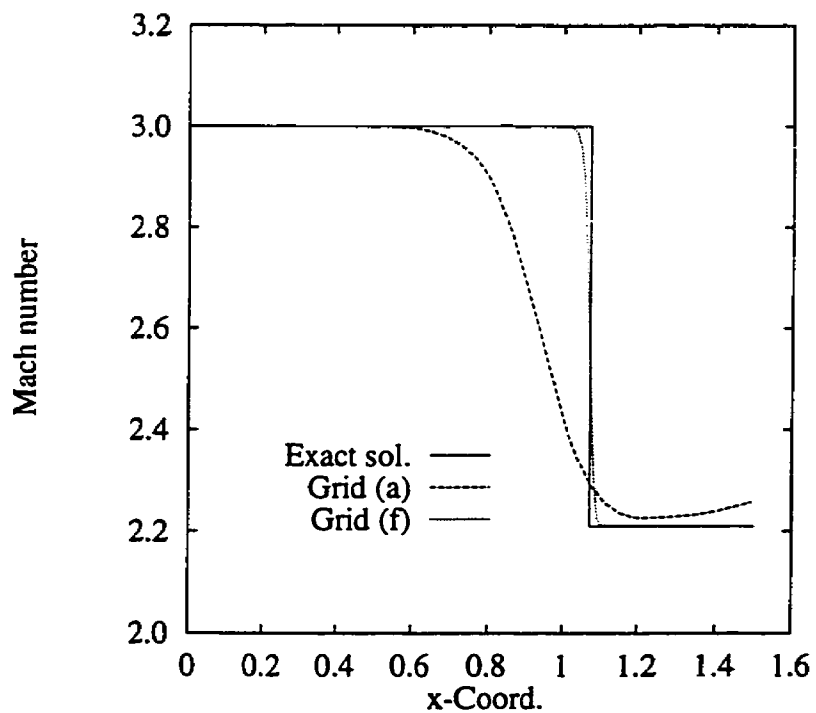


Figure 3.25: Distribution of the Mach number at  $y = 0.5$

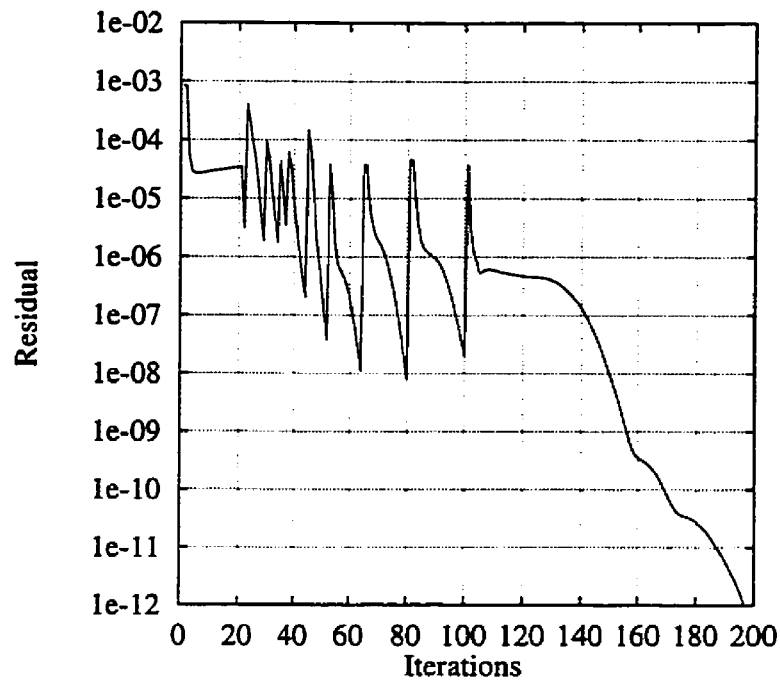


Figure 3.26: Convergence history of the flow solver

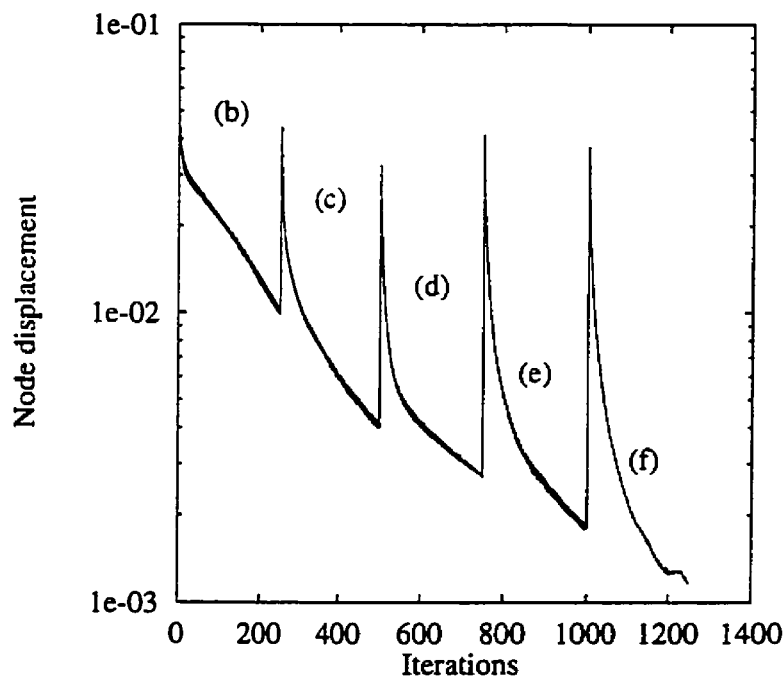


Figure 3.27: Convergence history of the adaptation procedure

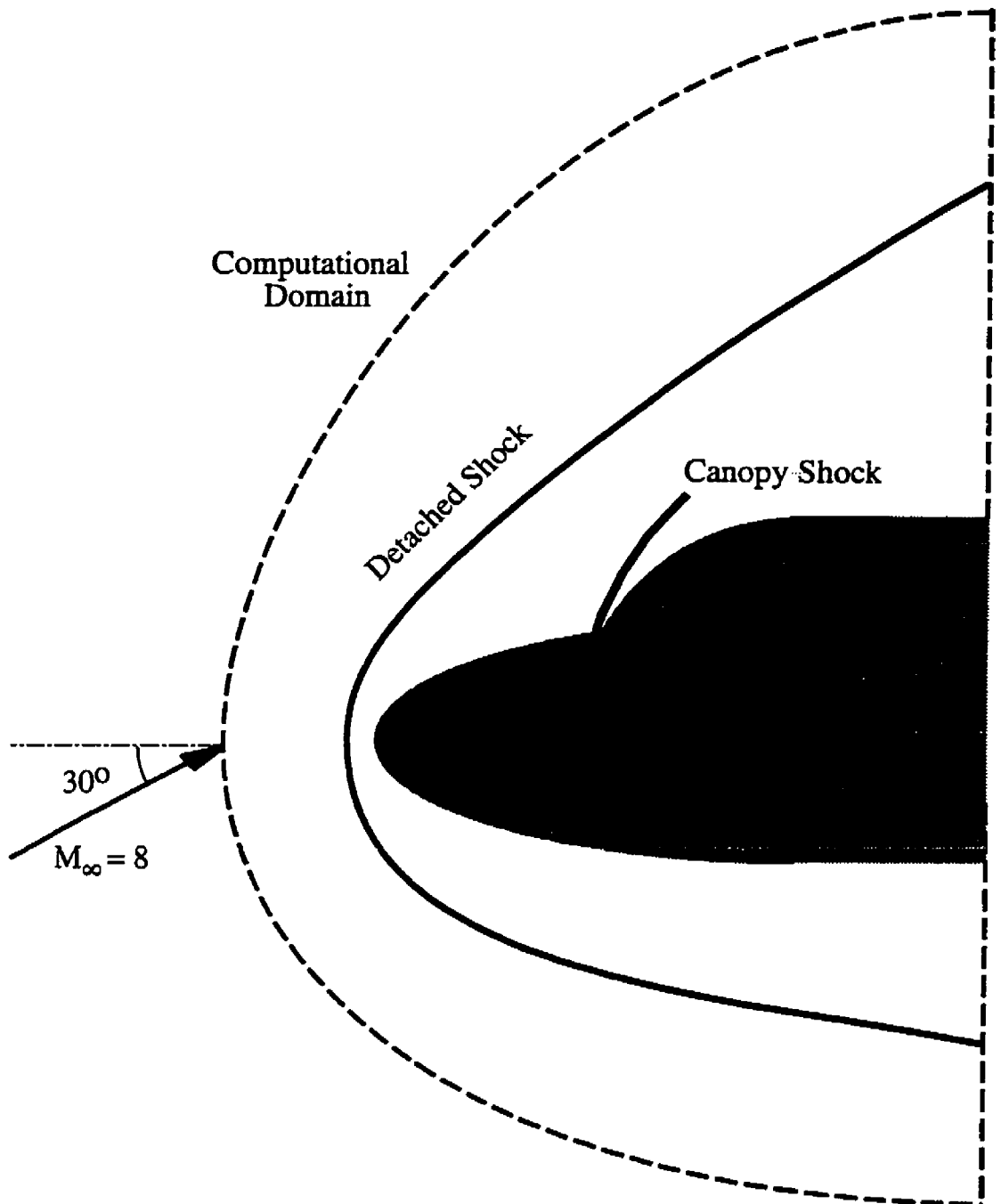


Figure 3.28: Definition of Mach 8 flow over a double ellipse test case

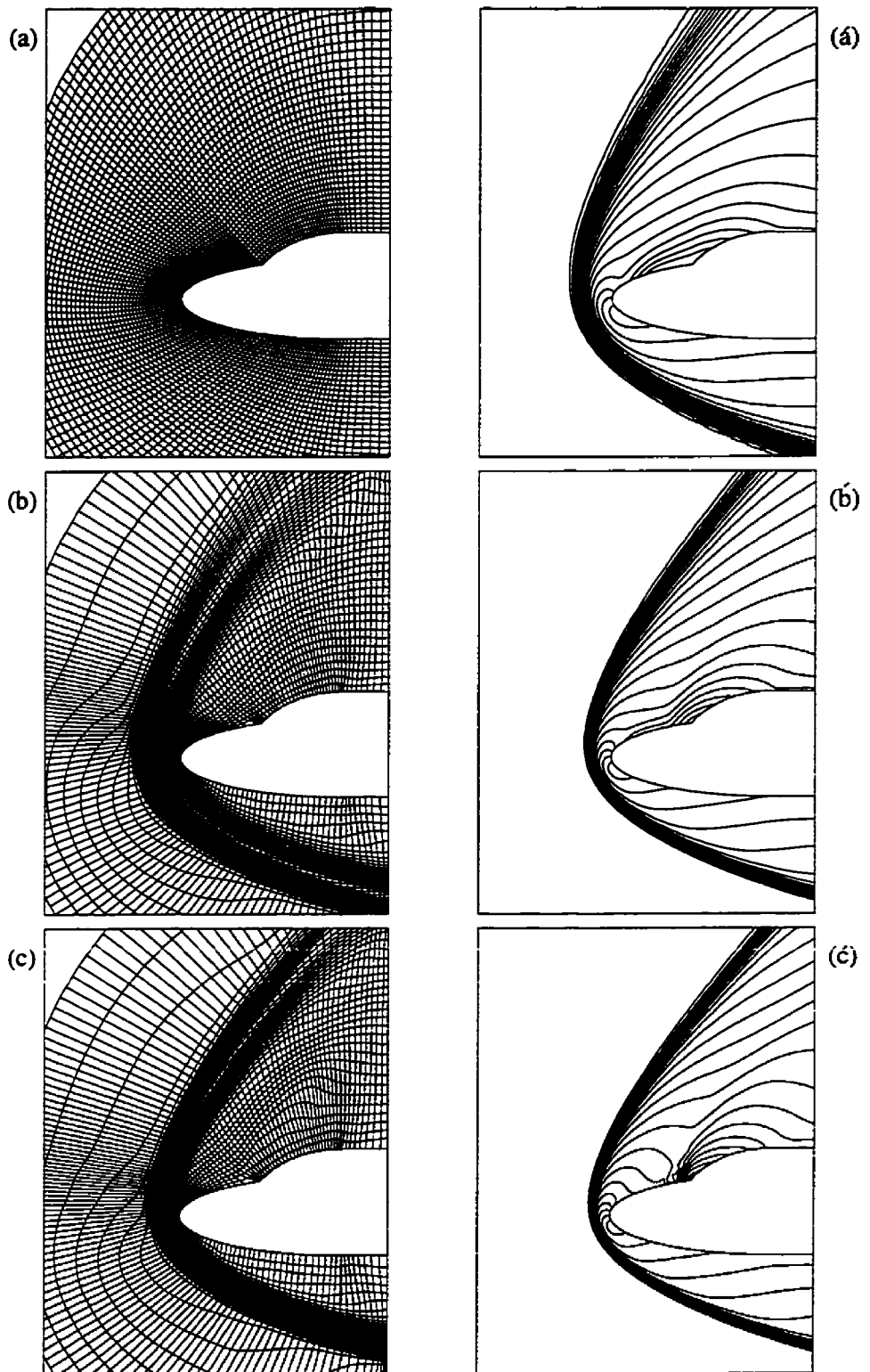


Figure 3.29: Adapted grids and the corresponding Mach number contours for cycles (a-c)

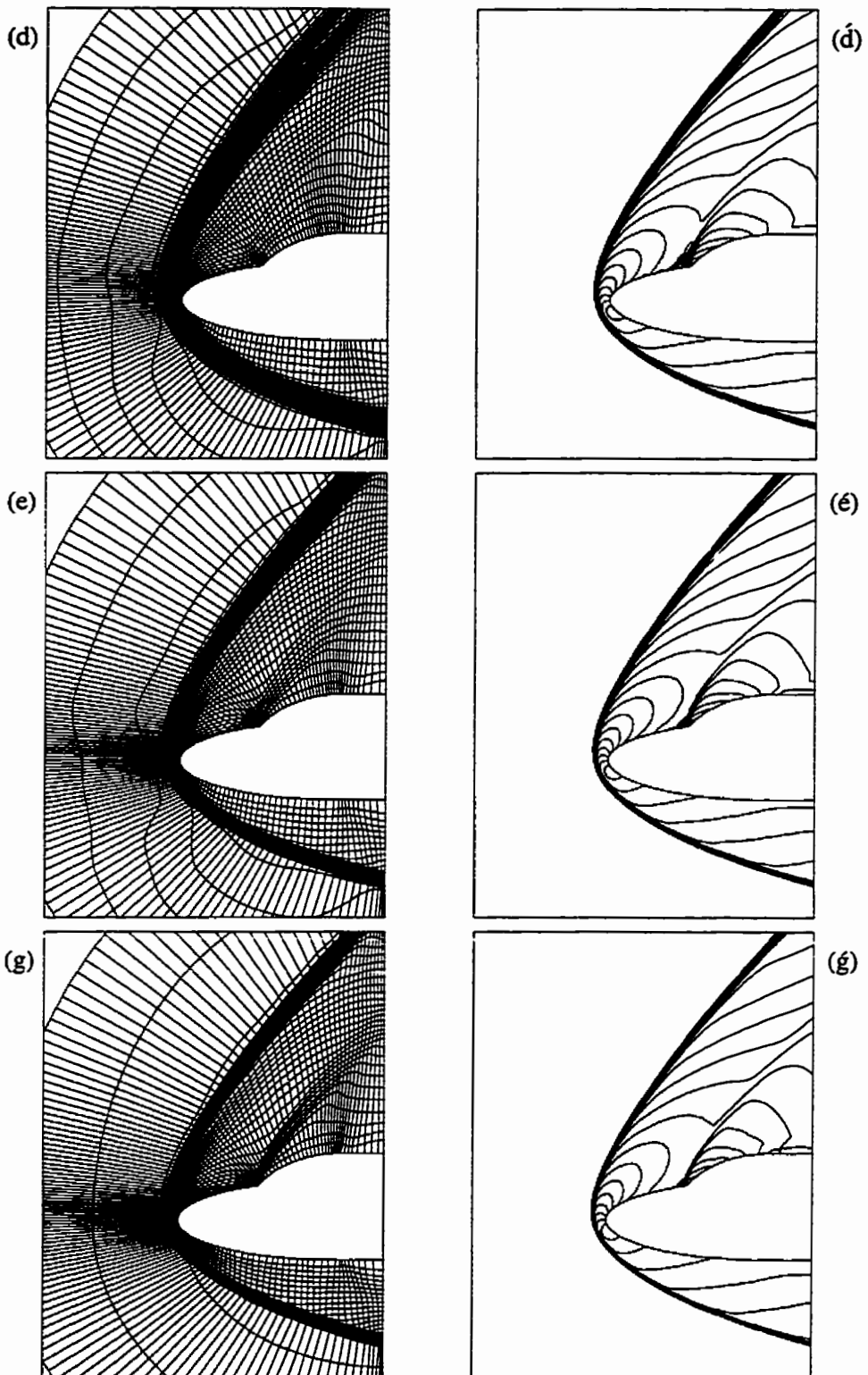


Figure 3.30: Adapted grids and the corresponding Mach number contours for cycles (d-f)

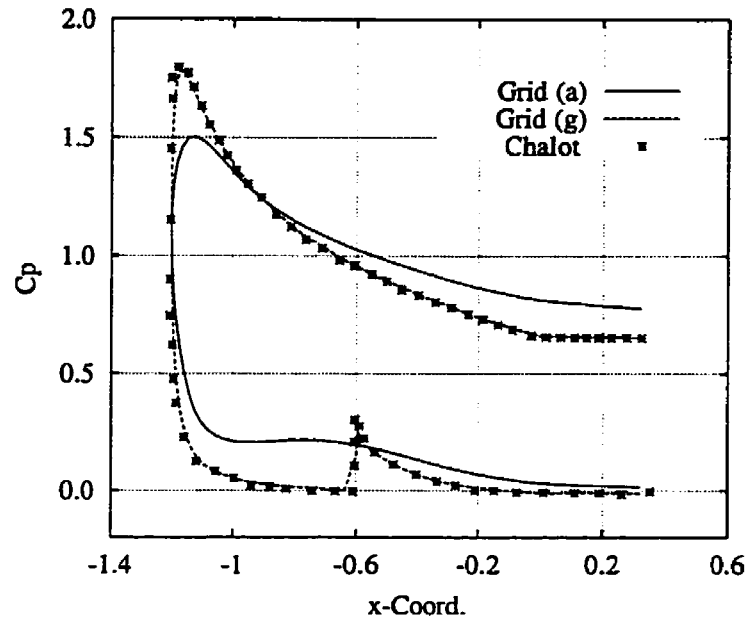


Figure 3.31: Enhancement of the  $C_p$  distribution on the wall with grid adaptation cycles

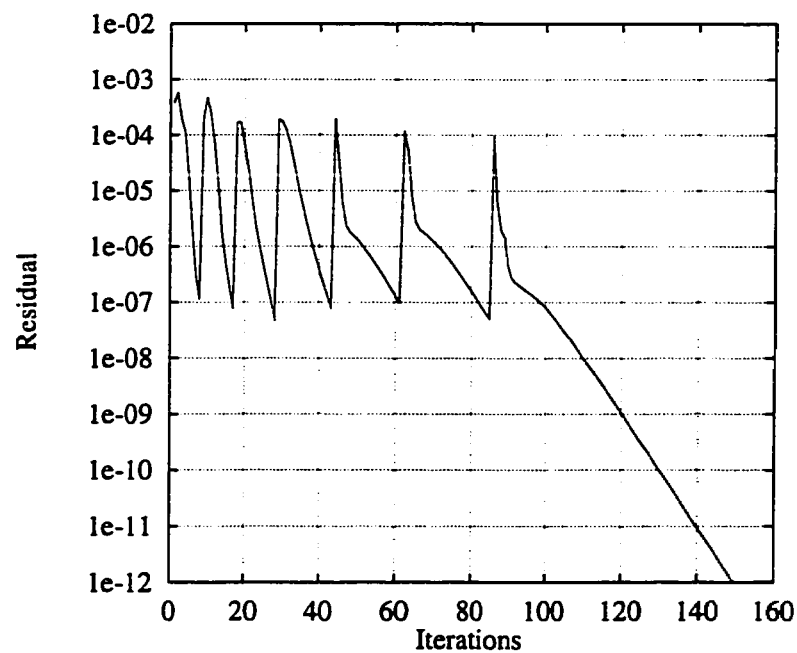


Figure 3.32: Convergence history of the flow solver

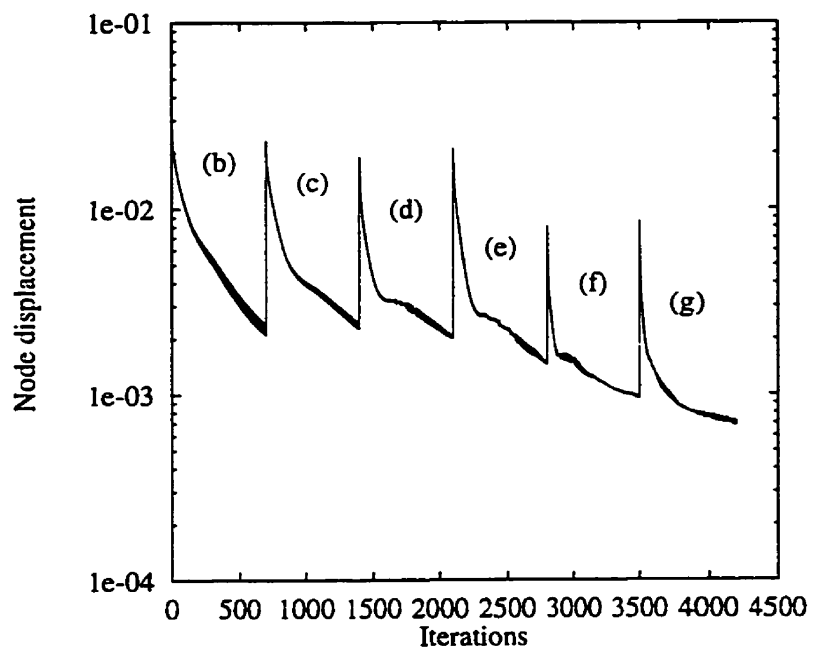


Figure 3.33: Convergence history of the adaptation procedure

# Chapter 4

## Governing Equations for Thermo-Chemical Nonequilibrium Flows

### 4.1 Introduction

This chapter is devoted to the derivation of the set of partial differential equations that governs the dynamics of inviscid *thermo-chemical nonequilibrium* flows. In addition to the Euler equations, a system of species transport equations and vibrational energy equations is required to model a gas mixture that is vibrationally excited and chemically reacting. The models describing species production rates and vibrational relaxation rates are also derived. This is followed by the development of an equation of state and a total internal energy expression for the gas considered. The last section presents some modeling simplifications, as well as the resulting governing equations.

The thermo-chemical nonequilibrium flow fields that are considered here are assumed to conform to the particular criteria outlined below. First of all, the Knudsen number for the flow problems at hand is assumed to be much lower than 0.1 and, therefore, the flow fields may be accurately described by a continuum. It is also assumed that there are a sufficient

number of collisions of gas molecules with walls so that no velocity or temperature slip exists at the wall.

If ionization phenomena of air are neglected, there remains only five neutral species to be considered, namely O, N, NO, N<sub>2</sub> and O<sub>2</sub>. This assumption is valid for reacting flows with a temperature below 9000 K. Although this condition is not strictly respected in this work, neglecting the ionization phenomena remains a reasonable assumption for practical problems of interest. These five species are identified by the subscript *s* which varies from 1 through 5, respectively.

We assume all energy modes are separable and consequently can be described by separate temperatures. We also assume that for all species the rotational mode is in equilibrium with the translational mode, and thus, can be characterized by a single temperature *T*. This last assumption is reasonable under conditions within the continuum regime where for air species the rotational equilibration with the translation needs few collisions due to the low characteristic of the rotational temperature. Thus the equilibration between the two modes is quickly reached.

## 4.2 Mass Conservation Equations

The conservation equation of mass for the chemical species *s* may be written in the form

$$\frac{\partial \rho_s}{\partial t} + \frac{\partial}{\partial x_i} (\rho_s v_{si}) = S_s^c, \quad (4.1)$$

as suggested in many references [9, 76, 122]. Here,  $v_{si}$  denotes the species velocity components and  $S_s^c$  is the chemical rate of production of the species *s*.

The above equation can be expressed as a function of the mass-averaged velocity,  $v$ , by introducing species diffusion velocities  $v_s^d$ . The diffusion velocity of any species is defined

as the difference between the species velocity and the mass-averaged velocity

$$v_s^d = v_s - \bar{v}, \quad (4.2)$$

where the mass-averaged velocity is expressed as

$$\bar{v} = \sum_{s=1}^{N_s} \frac{\rho_s}{\rho} v_s. \quad (4.3)$$

Substituting these new velocities in equation (4.1) and noting that  $\rho = \sum_s \rho_s$ , the species mass conservation equation is transformed to

$$\frac{\partial \rho_s}{\partial t} + \frac{\partial}{\partial x_i} (\rho_s v_i) = -\frac{\partial}{\partial x_i} (\rho_s v_{si}^d) + S_s^c. \quad (4.4)$$

For an inviscid flow the diffusion contribution is neglected and the species equation simplifies to

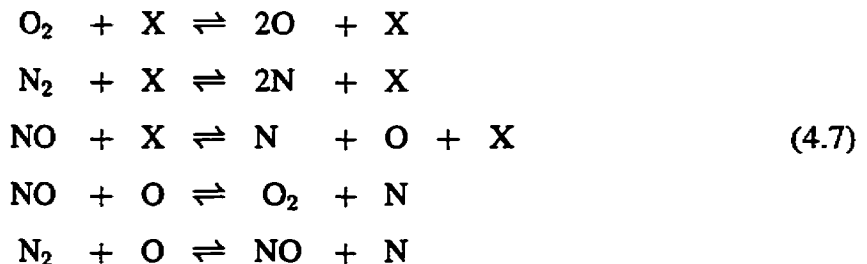
$$\frac{\partial \rho_s}{\partial t} + \frac{\partial}{\partial x_i} (\rho_s v_i) = S_s^c. \quad (4.5)$$

Recall that the total mass conservation (i.e. continuity) equation may be recovered by summing the equation (4.4) over all species and noting that the overall mass production rate and the overall mass flux owing to diffusion are zero, that is

$$\frac{\partial \rho}{\partial t} + \frac{\partial}{\partial x_i} (\rho v_i) = 0. \quad (4.6)$$

## 4.3 Chemical Source Terms

The most important chemical reactions among the five neutral species: O, N, NO, O<sub>2</sub> and N<sub>2</sub> that compose a dissociated air are written in a compact form as



where X represent any species that acts as a collision partner in the reaction and is not altered, giving a total of 17 reactions. The first three reactions are called *dissociation* reactions and the last two are *shuffle* reactions.

It should be noted that the direct formation reaction for the nitrogen monoxide,



introduced in early models is now usually discarded as it can be obtained as a combination of dissociation and shuffle reactions.

At high temperatures, chemical reactions will occur in gas flows resulting in changes in the amount of mass of each chemical species. This is represented by the term  $S_s^c$  on the right-hand-side of species mass conservation equations (4.5). In a general mixture of  $N_s$  species there will be  $N_r$  reactions taking place which can be expressed as

$$\sum_{s=1}^{N_s} \nu'_{sr} Y_s \rightleftharpoons \sum_{s=1}^{N_s} \nu''_{sr} Y_s, \quad r = 1, \dots, N_r \tag{4.9}$$

where  $Y_s$  is any chemical species among the five neutral species listed above. The parameters  $\nu'_{sr}$  and  $\nu''_{sr}$  are the stoichiometric coefficients for reactants and products of species  $s$  in the  $r^{th}$  reaction, respectively.

The law of mass action is actually an empirical formulation confirmed by numerous experimental observations [122]. The law states that the rate of appearance or disappearance of chemical species is proportional to the products of the concentrations to a power

equal to the corresponding stoichiometric coefficient. The rate of change of any species concentration  $[Y_s]$  resulting from these elementary reactions is

$$S_s^c = \mathcal{M}_s \sum_{r=1}^{N_r} (\nu'_{sr} - \nu''_{sr})(R_{fr} - R_{br}), \quad (4.10)$$

where the forward rate of reaction is given by

$$R_{fr} = k_{fr}(T) \prod_{l=1}^{N_s} \left( \frac{\rho_l}{\mathcal{M}_l} \right)^{\nu'_{lr}}, \quad (4.11)$$

and similarly for the rate of the reverse chemical reaction,

$$R_{br} = k_{br}(T) \prod_{l=1}^{N_s} \left( \frac{\rho_l}{\mathcal{M}_l} \right)^{\nu''_{lr}}. \quad (4.12)$$

The symbol  $\prod_{l=1}^{N_s}$  denotes a product over all values of species set and,  $k_{fr}$  and  $k_{br}$  represent forward and backward reaction rate coefficients.

These chemical rate coefficients are generally measured experimentally. Although methods from kinetic theory exist for their theoretical estimation, such results are sometimes inaccurate by several order of magnitude [103]. Using the well-known *Arrhenius equation*, empirical results for many reactions can be correlated in the form

$$k_f(T) = C_f \exp \left( -\frac{E_a}{kT} \right), \quad (4.13)$$

where  $E_a$  is the activation energy,  $k$  the Boltzmann constant and  $C_f$  a constant. To cover a wider range of reactions, equation (4.13) has been improved by including a pre-exponential temperature factor, leading to

$$k_f(T) = C_f T^{\mu_f} \exp \left( -\frac{E_a}{kT} \right), \quad (4.14)$$

where all the parameters:  $C_f$ ,  $\mu_f$  and  $E_a$  are deduced from experimental data.

Equation (4.14) is usually rewritten in the following functional form

$$k_{fr}(T) = C_{fr} T^{\mu_{fr}} \exp\left(-\frac{\theta_{d,fr}}{T}\right), \quad (4.15)$$

where the rate constants  $C_{fr}$ ,  $\eta_{fr}$  and  $\theta_{d,fr}$  are given in Appendix A.

The backward rate coefficient is generally deduced from the equilibrium constant as

$$k_{br}(T) = \frac{k_{fr}(T)}{K_{eq,r}(T)}. \quad (4.16)$$

For a certain chemical reaction models, such as Dunn and Kang [71], the backward coefficient is, however, directly computed by a formula which possesses the same form as the forward coefficient equation (4.15).

In Park's reaction model (1985), the equilibrium constants  $K_{eq,r}$  for the chemical reactions are computed according to following expression:

$$K_{eq,r} = \exp(A_{1r} + A_{2r}Z + A_{3r}Z^2 + A_{4r}Z^3 + A_{5r}Z^4), \quad (4.17)$$

where  $Z = 10,000/T$  and the constants  $A_{lr}$ , with  $l = 1-5$ , are provided in Appendix A.

A few years later, the same author [105] presented a revised formula that is consistent with the two-temperature model,

$$K_{eq,r} = \exp(A_{1r}Z + A_{2r} + A_{3r} \ln(1/Z) + A_{4r}/Z + A_{5r}/Z^2), \quad (4.18)$$

where the constants  $A_{lr}$  are also given in Appendix A

## 4.4 Conservation Equation of Species Vibrational Energy

In high temperature flows, diatomic species of the gas mixture experience violent collisions that may result in the perturbation of their vibrational states. Then, they begin to seek their new equilibrium properties by relaxing toward the translational temperature of the flow. The aim of this section is to derive a set of equations that governs this thermal nonequilibrium rate process, also referred to as *vibrational relaxation*. This derivation is subject to the following principal assumptions:

- Diatomic molecules are assimilated to *harmonic oscillators*.
- Collisional *vibration-vibration* exchanges are neglected.
- Vibrational heat conduction is neglected.
- The energy of oscillators upon collision takes place only between adjacent states.

The last assumption is consistent with detailed quantum-mechanical studies of transition probabilities during weak interactions.

Upon these assumptions the conservation equation of the vibrational energy for diatomic species  $s$  may be expressed as [122]

$$\frac{\partial \psi_{vs}}{\partial t} + \frac{\partial}{\partial x_i} (\psi_{vs} v_{si}) = \frac{\psi_{vs}^*(T) - \psi_{vs}(T_{vs})}{\tau_{vs}}, \quad (4.19)$$

where  $\tau_{vs}$  represents the relaxation time,  $\psi_{vs}$  is the vibrational energy per particle  $s$  and  $\psi_{vs}^*$  is the vibrational energy that the gas would have if it were in equilibrium at the translational temperature  $T$ . This remarkably simple equation shows that the vibrational energy of the diatomic species will always tend toward the equilibrium value, as one might expect. It also shows that the rate at which it so tends is *linearly* proportional to the amount that it departs from equilibrium at that instant.

The vibrational energy per particle  $s$  is given by

$$\psi_{vs} = \frac{k\theta_{vs}}{\exp(\theta_{vs}/T_{vs}) - 1}, \quad (4.20)$$

where  $T_{vs}$  refers to the vibrational temperature of the molecular species  $s$ . The coefficients  $\theta_{vs}$  are the vibrational characteristic temperatures and are provided in Table A.3.

The vibrational energy per unit volume is related to the vibrational energy per particle by the relation

$$e_{vs} = \psi_{vs} \frac{\mathcal{N}}{\mathcal{M}_s}. \quad (4.21)$$

Knowing that  $\mathcal{N}k = \mathcal{R}$  and  $R_s = \mathcal{R}/\mathcal{M}_s$ , the above equation may be rewritten as

$$e_{vs} = \frac{R_s \theta_{vs}}{\exp(\theta_{vs}/T_{vs}) - 1} \quad (4.22)$$

and equation (4.19) becomes

$$\frac{\partial e_{vs}}{\partial t} + \frac{\partial}{\partial x_i}(e_{vs} v_{si}) = \frac{e_{vs}^*(T) - e_{vs}(T_{vs})}{\tau_{vs}}. \quad (4.23)$$

Instead of the non-conservative form given by the equation (4.23), we are more concerned, for numerical discretization purposes, with the conservative form. That is

$$\frac{d\rho_s e_{vs}}{dt} = \rho_s \frac{de_{vs}}{dt} + e_{vs} \frac{d\rho_s}{dt}, \quad (4.24)$$

where the first derivative term on the RHS is given by equation (4.23) and the last derivative term by the species equation (4.5). After these substitutions are carried out, the vibrational energy conservation equation may be expressed in the conservative form as

$$\frac{\partial \rho_s e_{vs}}{\partial t} + \frac{\partial}{\partial x_i}(\rho_s e_{vs} v_{si}) = q_{T-v,s} + e_{vs} S_s^c, \quad s = 3, \dots, N_s \quad (4.25)$$

where  $q_{T-v_s}$  denotes the vibrational rate due to translation-vibration energy exchanges and is given by

$$q_{T-v_s} = \rho_s \frac{e_{vs}^*(T) - e_{vs}(T_{vs})}{\tau_{vs}}. \quad (4.26)$$

The vibrational energy equation may be extended to include vibration-vibration energy exchanges by adding the corresponding rate,  $q_{v-v_s}$ , to the vibrational source term. This leads to

$$\frac{\partial \rho_s e_{vs}}{\partial t} + \frac{\partial}{\partial x_i} (\rho_s e_{vs} v_{si}) = q_{T-v_s} + q_{v-v_s} + e_{vs} S_s^c, \quad s = 3, \dots, N_s. \quad (4.27)$$

## 4.5 Vibrational Source Term

The vibrational source term, as derived in the previous section, is composed of three energy exchange rates: translation-vibration rate,  $q_{T-v_s}$ , vibration-vibration rate,  $q_{v-v_s}$  and chemical-vibration rate,  $e_{vs} S_s^c$ . Since the second source term cancels for the *two-temperature model* and the third term has been already derived in Section 4.3, this section is limited to the derivation of the translation-vibration rate.

The translation-vibration energy exchange rate is principally modeled by the Landau-Teller equation [103]. This equation is valid unconditionally at relatively low-temperatures, or conditionally at all temperatures immediately behind the shock wave. The extension of this equation to a gas mixture gives

$$q_{T-v_s} = \rho_s \frac{e_{vs}^*(T) - e_{vs}(T_{vs})}{\langle \tau_s^{L-T} \rangle}, \quad (4.28)$$

where  $\langle \tau_s^{L-T} \rangle$  represents the molar averaged Landau-Teller relaxation time and is given

by Lee [76] as

$$\langle \tau_s^{L-T} \rangle = \frac{\sum_{l=1}^{N_s} \chi_l}{\sum_{l=1}^{N_s} \chi_l / \tau_{sl}^{L-T}}. \quad (4.29)$$

The Landau-Teller inter-species relaxation time,  $\tau_{sl}^{L-T}$ , is correlated by Millikan and White's [87] semi-empirical formula as follows:

$$\begin{cases} \tau_{sl}^{L-T} &= \frac{101300}{p} \exp \left[ A_{sl} (T^{-1/3} - 0.015 \mu_{sl}^{1/4}) - 18.42 \right], \\ A_{sl} &= 1.16 \cdot 10^{-3} \mu_{sl}^{1/2} \theta_{vs}^{4/3}, \\ \mu_{sl} &= M_s M_l / (M_s + M_l). \end{cases} \quad (4.30)$$

For temperatures higher than 8000K, the Millikan and White formula, however, results in unrealistically small relaxation times due to an overprediction of the collision cross-section. In order to correct this inadequacy, Park [102] suggested to add a new relaxation time,  $\tau_s^P$ , to the previous Landau-Teller relaxation time as shown

$$\tau_s^{L-T} = \langle \tau_s^{L-T} \rangle + \tau_s^P, \quad (4.31)$$

where the collision limited relaxation time,  $\tau_s^P$ , is expressed as

$$\tau_s^P = \frac{1}{\xi_s \sigma_v X_s}. \quad (4.32)$$

Here,  $\xi_s = \sqrt{8RT/\pi M_s}$  represents the average molecular speed of species  $s$  and  $X_s$  is the number density of colliding particles. The limiting collision cross-section,  $\sigma_v$ , is approximated by the expression that was originally developed for nitrogen,

$$\sigma_v = 10^{-21} (50,000/T)^2. \quad (4.33)$$

Vibration-dissociation coupling is introduced through a rate controlling temperature  $T_a = \sqrt{T T_v}$ , which replaces the translational temperature in the computation of species rate of production, as proposed by Park [102].

## 4.6 Equation of State

In the low temperature range of aerodynamics, a gas mixture such as air is assumed to follow the perfect gas law, that is

$$p = \rho R T, \quad (4.34)$$

where the specific gas constant,  $R$ , have a value of  $287 \text{ m}^2/\text{s}^2\text{K}$  for air. This law implies that forces between the molecules are negligible.

At high temperatures, this relation still holds for any species of a gas mixture leading to the definition of the total pressure by Dalton's law

$$p = \sum_{s=1}^{N_s} p_s, \quad (4.35)$$

where  $p_s$  is the partial pressure contribution of the species  $s$ .

By applying the equation (4.34) to each species and substituting the result into equation (4.35), this yields

$$p = \rho \bar{R} T, \quad (4.36)$$

where the average gas constant is defined as  $\bar{R} = \sum_s c_s R_s$ .

## 4.7 Total Internal Energy Expression

The total internal energy by unit mass,  $e$ , of a gas mixture is composed of several mode contributions which may be written in the form

$$e = \sum_{s=1}^{N_s} c_s e_{ts} + \sum_{s=1}^{N_s} c_s e_{rs} + \sum_{s=1}^{N_s} c_s e_{os} + \sum_{s=1}^{N_s} c_s e_{vs} + \sum_{s=1}^{N_s} c_s e_{ks}. \quad (4.37)$$

The first energy term on the RHS of equation (4.37) represents the translation energy for species  $s$  and is defined by

$$e_{ts} = c_{vs}^t T, \quad (4.38)$$

where  $c_{vs}^t = \frac{3}{2}R_s$ , are the translation specific heats at constant volume. The rotational energy,  $e_{rs}$ , possesses a similar form as the equation (4.38), while the rotational specific heats at constant volume are given by

$$c_{vs}^r = \begin{cases} 0 & \text{for atoms } (s = 1, 3) \\ R_s & \text{for molecules } (s = 4, 5) \end{cases} \quad (4.39)$$

The term  $e_{os}$  represents the contribution of heat of formations and are expressed as

$$e_{os} = h_s^o, \quad (4.40)$$

where  $h_s^o$  denotes the enthalpy of formation of species  $s$  and is provided in Table A.3. We recall that the vibrational energy has the following form

$$e_{vs} = \frac{R_s \theta_{vs}}{\exp(\theta_{vs}/T_{vs}) - 1}. \quad (4.41)$$

The last contribution in equation (4.37) is due to the kinetic energy and is given by

$$e_{ks} = \frac{1}{2} v_i v_i. \quad (4.42)$$

## 4.8 Summary of the Governing Equations

The mass, momentum, total internal energy, species mass fractions and vibrational energy equations describing a 2-D thermo-chemical nonequilibrium flow may be summarized in the conservative form as

$$\mathbf{Q}_t + \mathbf{F}_{i,i} = \mathbf{S}, \quad (4.43)$$

where  $\mathbf{Q}$  represents the vector of the conservative variables,  $\mathbf{F}_i$  is the vector of convective fluxes and  $\mathbf{S}$  the vector of sources. For a gas-mixture with the five species: O, N, NO, O<sub>2</sub> and N<sub>2</sub>, the components of vectors  $\mathbf{Q}$ ,  $\mathbf{F}_i$  and  $\mathbf{S}$ , in 2-D problems, are

$$\mathbf{Q} = \begin{bmatrix} \rho \\ \rho v_1 \\ \rho v_2 \\ \rho e \\ \rho c_1 \\ \vdots \\ \rho c_4 \\ \rho c_3 e_{v3} \\ \vdots \\ \rho c_5 e_{v5} \end{bmatrix}, \quad \mathbf{F}_i = \begin{bmatrix} \rho v_i \\ \rho v_1 v_i + p \delta_{1i} \\ \rho v_2 v_i + p \delta_{2i} \\ (\rho e + p) v_i \\ \rho c_1 v_i \\ \vdots \\ \rho c_4 v_i \\ \rho c_3 e_{v3} v_i \\ \vdots \\ \rho c_5 e_{v5} v_i \end{bmatrix}, \quad \mathbf{S} = \begin{bmatrix} 0 \\ 0 \\ 0 \\ 0 \\ S_1^c \\ \vdots \\ S_4^c \\ q_{T-v3} + q_{v-v3} + S_3^c e_{v3} \\ \vdots \\ q_{T-v5} + q_{v-v5} + S_5^c e_{v5} \end{bmatrix}, \quad (4.44)$$

where  $c_s$  is the mass fraction of species  $s$  and is defined by

$$c_s = \rho_s / \rho. \quad (4.45)$$

In addition, the global mass conservations conditions dictates that:

$$\sum_{s=1}^{N_s} c_s = 1, \quad (4.46)$$

and the equation of state is given by

$$p = \rho \bar{R} T. \quad (4.47)$$

Finally, the total internal energy may be rewritten as

$$e = \bar{c}_v T + \sum_{s=1}^{N_s} c_s h_s^o + e_v + \frac{1}{2} v_i v_i, \quad (4.48)$$

where  $\bar{c}_v = \sum_s c_s (c_{vs}^t + c_{vs}^r)$ , represents the specific heats at constant volume for the air mixture.

## 4.9 Simplification of the Governing Equations

The great complication generated by the onset of chemical and vibrational equations poses a problem to numerical simulation efficiency. A realistic calculation of practical hypersonic flow problems remains an onerous task even on today's supercomputers. Extensive use of parallel and vector capabilities is necessary, but not sufficient for tackling such large scale CFD problems. Therefore, it is still important to perform some appropriate modeling simplifications which render the analysis feasible without impairing its usefulness.

The number of species transport equations may be reduced, in the case of inviscid flows, by replacing one of them by an algebraic equation for the conservation of elemental nitrogen to oxygen ratio in air. Assuming the molar concentration of oxygen and nitrogen in air to be 21% and 79%, respectively, the elemental conservation condition read as

$$\frac{c_1/\mathcal{M}_1 + c_3/\mathcal{M}_3 + 2c_4/\mathcal{M}_4}{c_2/\mathcal{M}_2 + c_3/\mathcal{M}_3 + 2c_5/\mathcal{M}_5} = \frac{21}{79}. \quad (4.49)$$

In the present study, the *two-temperature model* is used meaning that all molecular species are characterized by the same vibrational temperature  $T_v$ . This model requires the

solution of a single conservation equation for the total vibrational energy that is defined by

$$e_v = \sum_{s=3}^{N_3} c_s e_{vs}. \quad (4.50)$$

The vibrational energy equations of the system (4.43) are thus replaced by a single vibrational energy equation, resulting from their summation.

Substituting these modeling simplifications into system (4.43) leads to

$$\dot{\mathbf{Q}}_i + \mathbf{F}_{i,i} = \mathbf{S}, \quad (4.51)$$

where the components of vectors  $\dot{\mathbf{Q}}$ ,  $\mathbf{F}_i$  and  $\mathbf{S}$  are given by

$$\dot{\mathbf{Q}} = \begin{bmatrix} \rho \\ \rho v_1 \\ \rho v_2 \\ \rho e \\ \rho c_1 \\ \rho c_2 \\ \rho c_3 \\ \rho e_v \end{bmatrix}, \quad \mathbf{F}_i = \begin{bmatrix} \rho v_i \\ \rho v_1 v_i + p\delta_{1i} \\ \rho v_2 v_i + p\delta_{2i} \\ (\rho e + p)v_i \\ \rho c_1 v_i \\ \rho c_2 v_i \\ \rho c_3 v_i \\ \rho e_v v_i \end{bmatrix}, \quad \mathbf{S} = \begin{bmatrix} 0 \\ 0 \\ 0 \\ 0 \\ S_1^c \\ S_2^c \\ S_3^c \\ \sum_{s=3}^{N_3} q_{T-v,s} + \sum_{s=3}^{N_3} S_s^c e_{vs} \end{bmatrix}. \quad (4.52)$$

# Chapter 5

## Numerical Simulation of Thermo-Chemical Nonequilibrium Flows

### 5.1 Introduction

This chapter describes the numerical discretization of a set of a coupled partial differential equations that governs thermo-chemical nonequilibrium flows. Using a loosely coupled approach, the governing equations decouples into three physical systems, namely, a gasdynamic, chemical and vibrational systems. As discussed in Section 1.7, this segregated approach presents several advantages and leads to highly efficient and flexible code. Each system is integrated by an implicit time-marching technique, while a Galerkin-finite element method is used for spatial discretization. The flow solver is coupled to the mesh adaptation procedure that was presented in Chapter 3, within an artificial dissipation loop. The accuracy and efficiency of the overall methodology is then investigated on nitrogen and air hypersonic benchmarks.

Although, the numerical decoupling of the governing equations to three physical systems is a pure mathematical technique to solve a large system of PDEs, the physical in-

terpretation of this decoupling may help to devise an efficient numerical schemes for CFD problems with multitude time scales. For instance, the species concentrations and the vibrational energies are kept constant during the solution of the gasdynamic system and therefore a pseudo thermo-chemical equilibrium can be assumed in the derivation of the gasdynamic Jacobians, by casting the equation of state into the divariant gas form. This yields

$$p = \rho (\bar{\gamma} - 1) (\varepsilon - C) \quad (5.1)$$

where  $C = (\sum_s c_s h_s^o + e_v)$  is a constant.

The present method may be viewed as an extension to thermo-chemical *nonequilibrium* flows of the scheme that was already developed in Chapter 2 for *equilibrium* flows. Although the two formulations based on the exact<sup>1</sup> and approximate<sup>2</sup> flux Jacobians are still valid within the context of a segregated method, only the second formulation (*equivalent- $\bar{\gamma}$* ) is considered in the current computations. This choice is mainly justified by the minor modifications that are needed to an existing gasdynamic code to accommodate the calculations of thermo-chemical nonequilibrium flows.

## 5.2 Numerical Scheme

The governing equations (4.51) are decoupled into three systems of equations:  
a *gasdynamic system*,

$$\mathbf{Q}_t^g + \mathbf{F}_{i,i}^g = \mathbf{S}^g, \\ \mathbf{Q}^g = \begin{bmatrix} \rho \\ \rho v_1 \\ \rho v_2 \\ \rho e \end{bmatrix}, \quad \mathbf{F}_i^g = \begin{bmatrix} \rho v_i \\ \rho v_1 v_i + p \delta_{1i} \\ \rho v_2 v_i + p \delta_{2i} \\ (\rho e + p) v_i \end{bmatrix}, \quad \mathbf{S}^g = \begin{bmatrix} 0 \\ 0 \\ 0 \\ 0 \end{bmatrix}, \quad (5.2)$$

---

<sup>1</sup>This formulation is based on a general equation of state for divariant gases.

<sup>2</sup>This formulation used *equivalent- $\bar{\gamma}$*  technique.

a *chemical system*,

$$\mathbf{Q}_{,t}^c + \mathbf{F}_{i,i}^c = \mathbf{S}^c,$$

$$\mathbf{Q}^c = \begin{bmatrix} \rho c_1 \\ \rho c_2 \\ \rho c_3 \end{bmatrix}, \quad \mathbf{F}_i^c = \begin{bmatrix} \rho c_1 v_i \\ \rho c_2 v_i \\ \rho c_3 v_i \end{bmatrix}, \quad \mathbf{S}^c = \begin{bmatrix} S_1^c \\ S_2^c \\ S_3^c \end{bmatrix}, \quad (5.3)$$

and a *vibrational system*,

$$\mathbf{Q}_{,t}^v + \mathbf{F}_{i,i}^v = \mathbf{S}^v,$$

$$\mathbf{Q}^v = [ \rho e_v ], \quad \mathbf{F}_i^v = [ \rho e_v v_i ], \quad \mathbf{S}^v = \left[ \sum_{s=3}^{N_s} q_{T-v,s} + \sum_{s=3}^{N_s} S_s^c e_{vs} \right], \quad (5.4)$$

and solved in a time-lagged manner.

For the sake of simplicity, the numerical discretization will be demonstrated on one representative system, namely,

$$\mathbf{Q}_{,t} + \mathbf{F}_{i,i} = \mathbf{S} + \mathbf{G}_{i,i}. \quad (5.5)$$

where  $\mathbf{G}_i$  are the dissipation fluxes that are needed for eliminating numerical oscillations.

The definition of the flux vector  $\mathbf{G}_i$  for the three systems is given by

$$\mathbf{G}_i = \begin{cases} \epsilon \bar{\mathbf{Q}}_{,i}^g & \text{for the gasdynamic system} \\ \epsilon \mathbf{Q}_{,i}^c & \text{for the chemical system} \\ \epsilon \mathbf{Q}_{,i}^v & \text{for the vibrational system} \end{cases} \quad (5.6)$$

where the vector  $\bar{\mathbf{Q}}^g$  results from substituting the total internal energy by the total enthalpy in  $\mathbf{Q}^g$ .

The discretization of each system is carried out by an implicit formulation in time and

a Galerkin-FEM in space. The present numerical method is described in more details for the Euler equations in Chapter 2 and leads to the following algebraic system of equations:

$$(\bar{\mathbf{M}} + \bar{\mathbf{K}}) \Delta \hat{\mathbf{U}} = -\bar{\mathbf{R}}, \quad (5.7)$$

where the RHS matrices  $\bar{\mathbf{M}}$  and  $\bar{\mathbf{K}}$ , and the residual vector  $\bar{\mathbf{R}}$  are given by

$$\left\{ \begin{array}{l} \bar{\mathbf{M}}_{IJ} = \int_{\Omega} \frac{1}{\Delta t} L \Phi_I \Phi_J d\Omega, \\ \bar{\mathbf{K}}_{IJ} = \int_{\Gamma} \mathbf{A}_i n_i \Phi_I \Phi_J d\Gamma - \int_{\Omega} (\mathbf{A}_i \Phi_{I,i} + \mathbf{B} \Phi_I) \Phi_J d\Omega \\ \quad - \int_{\Gamma} (\mathbf{C}_i \Phi_J + \mathbf{D}_{ij} \Phi_{J,i}) n_i \Phi_I d\Gamma + \int_{\Omega} (\mathbf{C}_i \Phi_J + \mathbf{D}_{ij} \Phi_{J,i}) \Phi_{I,j} d\Omega, \\ \bar{\mathbf{R}}_I = \int_{\Gamma} (\mathbf{F}_i - \mathbf{G}_i) n_i \Phi_I d\Gamma - \int_{\Omega} (\mathbf{F}_i - \mathbf{G}_i) \Phi_{I,i} d\Omega - \int_{\Omega} \mathbf{S} \Phi_I d\Omega. \end{array} \right. \quad (5.8)$$

We recall that the Jacobians matrices are defined by

$$\mathbf{L} = \frac{\partial \mathbf{Q}}{\partial \mathbf{U}}, \quad \mathbf{A}_i = \frac{\partial \mathbf{F}_i}{\partial \mathbf{U}}, \quad \mathbf{B} = \frac{\partial \mathbf{S}}{\partial \mathbf{U}}, \quad \mathbf{C}_i = \frac{\partial \mathbf{G}_i}{\partial \mathbf{U}}, \quad \mathbf{D}_{ij} = \frac{\partial \mathbf{G}_i}{\partial \mathbf{U}_j}, \quad (5.9)$$

where the vector  $\mathbf{U} = [\mathbf{U}^g, \mathbf{U}^c, \mathbf{U}^v]$  refers to any primitive variable vector of the solved systems and it is approximated by bilinear shape functions.

For the gasdynamic system (5.2), all the above Jacobian matrices are derived using the *equivalent- $\tilde{\gamma}$*  technique to include the thermo-chemical nonequilibrium effects. This formulation permits the reuse the Euler solver that was developed in Chapter 2 for frozen and thermo-chemical equilibrium flows. The value of  $\tilde{\gamma}$  is computed from the following formula,

$$\tilde{\gamma} = 1 + \frac{p}{\rho \epsilon}, \quad (5.10)$$

so the value of the pressure matches the one given by the Dalton's law (4.47).

For both chemical and vibrational systems, the Jacobians  $\mathbf{L}$ ,  $\mathbf{A}_i$ ,  $\mathbf{C}_i$  and  $\mathbf{D}_{ij}$  are derived

to be

$$\begin{aligned}\mathbf{L} &= \rho \mathbf{I}, \\ \mathbf{A}_i &= \rho v_i \mathbf{I}, \\ \mathbf{C}_i &= \epsilon \rho_{,i} \mathbf{I}, \\ \mathbf{D}_{ij} &= \epsilon \rho \delta_{ij} \mathbf{I},\end{aligned}\tag{5.11}$$

where  $\mathbf{I}$  refers to the identity matrix.

The nonlinearity of the chemical and vibrational source terms makes the derivation of their Jacobians a tedious task which is further complicated by the use of a controlling rate temperature in the case of a two-temperature model. These Jacobians are intimately linked to the thermo-chemical state of the flow which leads to consider a separate Jacobian matrix for each regime. The derivation details of the Jacobian  $\mathbf{B}^c$  for the chemical source terms are presented in Appendix B, in the case of chemical nonequilibrium and *thermal equilibrium* flows. For thermo-chemical nonequilibrium flows, the Jacobians  $\mathbf{B}^c$  and  $\mathbf{B}^v$  are described in Appendix C.

### 5.3 Relaxation of Chemical Source Terms

In order to prevent unrealistic species mass fractions (i.e.  $c_s \notin [0, 1]$ ) that may result in the first Newton iterations, the chemical source terms are relaxed according to the following formula:

$$\tilde{S}_s^c = \frac{S_s^c - |S_s^c|}{2 \max(\epsilon, c_s)} c_s + \frac{S_s^c + |S_s^c|}{2 \max(\epsilon, 1 - c_s)} (1 - c_s),\tag{5.12}$$

where  $\epsilon$  refers to a small constant of order of  $10^{-10}$ .

For an endothermic reaction ( $S_s^c > 0$ ), the first term on the RHS of the equation (5.12) vanishes and the source term expression becomes

$$\tilde{S}_s^c = \begin{cases} S_s^c & \text{if } c_s \leq (1 - \epsilon) \\ S_s^c (1 - c_s)/\epsilon & \text{otherwise} \end{cases}\tag{5.13}$$

Therefore, the source term is only corrected by a factor of  $(1 - c_s)/\epsilon$  in the case when the product concentration,  $c_s$ , approaches unity (i.e.  $c_s \geq (1 - \epsilon)$ ).

For an exothermic reaction ( $S_s^c < 0$ ), the second term on the RHS of the equation (5.12) vanishes and the source term may be rewritten as

$$\bar{S}_s^c = \begin{cases} S_s^c & \text{if } c_s \geq \epsilon \\ S_s^c c_s / \epsilon & \text{otherwise} \end{cases} \quad (5.14)$$

In this case, the source term is only corrected by a factor of  $c_s/\epsilon$  when the reactant concentration,  $c_s$ , approaches zero (i.e.  $c_s \leq \epsilon$ ).

## 5.4 Solution Procedure

In summary, a set of *eight PDEs* –gasdynamic system (4 Eqs.) (5.2), chemical system (3 Eqs.) (5.3) and vibrational system (1 Eq.) (5.4)– and *five algebraic equations* –global mass conservation (4.45), conservation of elemental nitrogen to oxygen ratio (4.49), total vibrational energy formula (4.50), total internal energy formula (4.48) and the equation of state (4.47)– are solved for the thirteen primitive variables  $-\rho, v_1, v_2, e, c_1, c_2, c_3, c_4, c_5, e_v, T_v, T, p-$ .

The primitive variable vector  $\mathbf{U}^g = [\rho, v_1, v_2, e]$  is first advanced in time by solving the gasdynamic system (5.2) and then the chemical system (5.3) is solved for the species mass fraction vector  $\mathbf{U}^c = [c_1, c_2, c_3]$ , using the updated velocity field and density solutions. The remaining mass fractions,  $c_4$  and  $c_5$ , are deduced from the two algebraic equations (4.45) and (4.49) that can be rewritten as:

$$\begin{cases} c_4 = \frac{24}{103} - c_1 - \frac{8}{15}c_3, \\ c_5 = \frac{79}{103} - c_2 - \frac{7}{15}c_3. \end{cases} \quad (5.15)$$

The total vibrational energy,  $\mathbf{U}^v = [e_v]$ , is then calculated by integrating the vibrational system (5.4). The vibrational temperature  $T_v$  is computed from the total vibrational energy

equation (4.50) that may be rewritten in the form

$$f(T_v) = e_v - \sum_{s=3}^{N_s} c_s \frac{R_s \theta_{vs}}{\exp(\theta_{vs}/T_v) - 1} = 0. \quad (5.16)$$

Because the vibrational characteristic temperature,  $\theta_{vs}$ , varies for different molecular species, the nonlinear equation (5.16) needs to be solved by an iterative method such as a Newton's method. This procedure is applied for all grid nodes and at every time step and therefore may be computationally expensive.

Since the three neutral molecules ( $\text{NO}$ ,  $\text{O}_2$ ,  $\text{N}_2$ ) in air have close values of vibrational characteristic temperatures (2817, 2239, 3395), a good initial estimate of the vibrational temperature could be obtained by assuming that all these molecules have the same average vibrational characteristic temperature,  $\bar{\theta}_v$ , defined by

$$\bar{\theta}_v = \frac{\sum_{s=3}^{N_s} c_s \theta_{vs}}{\sum_{s=3}^{N_s} c_s}. \quad (5.17)$$

An initial estimate  $T_v^0$  can then be computed by substituting the value of  $\bar{\theta}_v$  in the equation (5.16), yielding

$$T_v^0 = \frac{\bar{\theta}_v}{\ln \left( 1 + (\bar{\theta}_v/e_v) \sum_{s=3}^{N_s} c_s R_s \right)}. \quad (5.18)$$

This iterative method is very efficient and usually does not need more than two Newton iterations per node to converge toward the final solution.

The translational-rotational temperature  $T$  is then deduced from the internal energy

formula (4.48), that is

$$T = \frac{1}{\bar{c}_v} (e - \sum_{s=1}^{N_s} c_s h_s^o - e_v - \frac{1}{2} v_i v_i). \quad (5.19)$$

Finally, if one assumes each individual species behaves as a perfect gas, the pressure of the mixture may be calculated according to Dalton's law (4.47).

It must be pointed out that the computation of chemical nonequilibrium flows (with thermal equilibrium,  $T = T_v$ ) can be easily carried out by only eliminating the vibrational system from the flow solver loop. In fact, the segregated approach permits to recover the thermal equilibrium flows without solving additional equations and modifying the vibrational relaxation times, as it is usually done in the coupled approach. In this case, the translational temperature is computed by a Newton method from the equation (4.48).

## 5.5 Numerical Results

All reacting flow computations are carried out using Park's reaction model (1985)<sup>3</sup> unless another reaction model is stated.

### 5.5.1 Hypersonic Nitrogen Flow over a Cylinder

The present numerical approach is first validated on a Mach 6 partially-dissociated nitrogen flow over a half-cylinder with 1 inch radius. This flow problem, that is illustrated in Fig. 5.1, has been investigated experimentally by Hornung [60] and numerically by numerous authors [21, 69, 104]. The freestream monatomic nitrogen mass fraction, temperature, density and velocity are 0.073, 1833 K,  $5.349 \cdot 10^{-3} \text{ kg/m}^3$  and 5,590 m/sec, respectively.

The numerical simulation of the current problem is performed using a five-species model by setting the mass fraction of oxygen to be  $10^{-10}$  in the freestream conditions. The chemical source terms are evaluated according to Park's reaction model (1992). In

---

<sup>3</sup>Rate reaction coefficients are provided in Appendix A

the current problem, the gas-mixture contains only one molecular species and hence, the multi-temperature model becomes equivalent to the two-temperature model.

The calculation is initiated on a coarse grid (see Fig. 5.2-(a)) with 33x53 nodes distributed uniformly in both directions. The corresponding Mach number contours of the flow are shown in Fig. 5.2-(a), with a very smeared shock. The adapted grid, depicted in Fig. 5.2-(f), required five cycles of adaptation and the corresponding solution, Fig. 5.2-(f), demonstrates the benefits of the grid adaptation in resolving a detached bow shock.

In Fig. 5.3, the iso-density contours of the numerical solution is compared with the fringe pattern of the flow field [60], which represents the gradient of the density. Although the accurate prediction of the fringe pattern cannot be verified, one may observe that the experimental standoff distance is well reproduced.

Fig. 5.4 shows the enhancement of the predicted Mach number distribution along the stagnation line with the grid adaptation cycles. In fact, the use of an appropriate grid allows a reduction of the artificial dissipation coefficient by a factor of 5.

Additional calculations are performed under two different assumptions: frozen perfect gas and chemical nonequilibrium (thermal equilibrium) of a mixture of perfect gases. All the calculations are made using the same initial uniform grid that is depicted in Fig. 5.2-(a). Temperature profiles along the stagnation line resulting from these two assumptions are compared in Fig. 5.5 to the thermo-chemical nonequilibrium case.

A comparison of these temperature profiles with the experimental shock position shows that the standoff distance is 85% larger in the case of a frozen flow. It may also be observed that a better prediction of the standoff distance is achieved by the chemical nonequilibrium or the thermo-chemical nonequilibrium assumption. As it was expected, the chemical nonequilibrium model leads to a shorter standoff distance compared with the thermo-chemical nonequilibrium case.

Aside from the perfect gas case which leads to unrealistically high temperatures in the shock layer, the peak of the translational temperature behind the shock is largest in the thermo-chemical nonequilibrium case ( $\approx 12,000K$ ). This peak, theoretically, should approach the perfect gas value [63]. However, because the computed shock thickness is of the same order as the characteristic length of vibrational relaxation, the computed translational temperature peak is relatively smaller.

The plot of the mass fractions of monatomic and diatomic nitrogen along the stagnation line in Fig. 5.6 shows that the flow field is dominated by a high degree of reaction. It may be observed that 30% of the present diatomic nitrogen is dissociated despite, the fact that the corresponding reactions have a large activation energy. It should be noted that this plot is obtained for the thermo-chemical nonequilibrium case, chemical nonequilibrium calculation, however, results in similar distributions. This is mainly due to the fact that their translational temperature profiles are identical, except in the vibrational relaxation region where the use of a rate controlling temperature ( $T_a = \sqrt{TT_v}$ ) tends to minimize the difference between these two temperature profiles.

In all these cases, a subsonic uniform flow is assumed as an initial solution for the flow solver and a relaxation factor of 0.6 is used in the mesh movement algorithm. Specifically for the thermo-chemical nonequilibrium case, the convergence history of both flow solver and adaptation grid procedures are presented in Figs. 5.7 and 5.8, where the jumps in the curves represent the beginning of each new cycle. Similarly to the frozen flow computations in Chapter 3, at each adaptation cycle<sup>4</sup>, the  $L_2$  norm of the residual vector for each solved system is lowered by three orders of magnitude and then the mesh nodes are displaced 250 times.

The solution times are of the order of 4.0, 2.9, 0.7 seconds per iteration for the gas-

---

<sup>4</sup>An adaptation cycle is equivalent to one unload artificial dissipation cycle.

dynamic, chemical and vibrational solvers, respectively, on two processors of a Silicon Graphics Power Challenge computer with four 75 MHZ, MIPS R8000 processors. The mesh adaptation requires 0.4 seconds per iteration on one processor of the same computer. It is worth noting that only the Gauss elimination method [17] was parallelized in the flow solver and no significant efforts were made to optimize the assembling routines in the flow solver code as well as the error estimate and mesh movement routines in the mesh adaptation code.

### 5.5.2 Hypersonic Air Flow over a Cylinder

In this example, the current methodology is applied to a hypersonic air flow over a half-cylinder with 0.05 m radius (see Fig. 5.9). The freestream conditions are:  $Ma_\infty = 12.7$ ,  $T_\infty = 196 K$  and  $\rho_\infty = 0.16 \cdot 10^{-2} kg/m^3$ . This test case was proposed in the workshop on Hypersonic Flows for Reentry Problems (HFRP) [1] and experimental results were obtained by Vetter *et al.* [121] for the same freestream conditions over a sphere.

The use of an adaptive procedure allows us to start the computation on the same grid as in the previous test case, Fig. 5.10-(a), although the physics of the two flows are completely different. The final adapted grid and the corresponding temperature contours are shown in Fig. 5.10, for a thermo-chemical nonequilibrium calculation.

A second calculation is performed using a chemical equilibrium assumption. The temperature profiles resulting from the two previous calculations are compared along the stagnation line in Fig. 5.11. The same behavior of the thermo-chemical models, as in the first benchmark, can be observed with a translational temperature peak of nearly 5800 K in the thermo-chemical nonequilibrium case.

Mass fraction plots of the five species are depicted in Fig. 5.12 along the stagnation line. It may be seen that nearly 40% of O<sub>2</sub> is dissociated, while the N<sub>2</sub> concentration remains almost constant.

Computed pressure coefficient distributions, using thermo-chemical nonequilibrium, chemical nonequilibrium and frozen assumptions, are compared to experimental results in Fig. 5.13 showing a fairly good agreement. This plot also demonstrates the invariance of the  $C_p$  values with respect to chemical and vibrational relaxation phenomena.

Similar to the first example, the present computation is initiated with a subsonic uniform solution with a relaxation factor of 0.5 for the adaptation procedure. The steady-state solution is obtained by marching in time with different time steps for the gasdynamic, chemical and vibrational systems. The solver's convergence is displayed in Fig. 5.14 and was obtained by using the following chemical and vibrational time steps:  $\Delta t^c = 0.4 \Delta t^g$  and  $\Delta t^v = 0.1 \Delta t^g$ . Here,  $\Delta t^g$  represents a local time step for the gasdynamic system and is computed according to a CFL number of 40. The convergence history of the adaptation procedure is shown in Fig. 5.15 where a decrease of nearly 2 orders of magnitude in node displacement is achieved after 6 adaptation cycles with 350 iterations by cycle.

### 5.5.3 Hypersonic Air Flow over a Double Ellipse

For this last example, a double ellipse profile is placed into a Mach 12.7 flow and zero angle of attack. This benchmark was proposed in the HFRP workshop [1] and its flow field includes a strong detached shock wave, followed by a moderate canopy shock and shock-shock interaction. Therefore, the application of mesh adaptation is highly suitable for efficiently resolving all these different strength shocks.

The thermo-chemical nonequilibrium calculation is carried out on a 45x124 (5580) grid, Fig. 5.16-(a), yielding a very dissipative solution which is displayed as temperature contours in Fig. 5.16-(á). The final adapted grid, shown in Fig. 5.16-(g), is obtained after 6 adaptation levels. The final adapted solution is presented in Fig. 5.16-(g) and it can be clearly seen that all the main features of the flow field are well resolved.

The iso-contours of monatomic oxygen concentration are displayed in Fig. 5.17. One

may observe that the  $O_2$  is only partially dissociated due the moderate temperatures in the flow field. The distributions of the translational and vibrational temperatures along the stagnation line are presented in Fig. 5.18, revealing that thermal equilibrium state is not reached at the stagnation point. This result could be explained by the short distance between the bow shock and the nose of the double ellipse.

The pressure coefficient on the body surface is displayed in Fig. 5.19 for the initial and final adapted grids. It can be clearly seen that the adapted mesh permits a much better capturing of the canopy shock, as well as the stagnation properties.

The residual convergence for the gasdynamic, chemical and vibrational solvers is presented in Fig. 5.20. The steady solution is obtained by advancing the chemical and vibrational solutions with time steps of  $\Delta t^c = 0.3 \Delta t^g$  and  $\Delta t^v = 0.1 \Delta t^g$ . The node displacement convergence history is depicted in Fig. 5.21 for a relaxation factor of 0.45 and 700 iterations by cycle.

## **FIGURES**

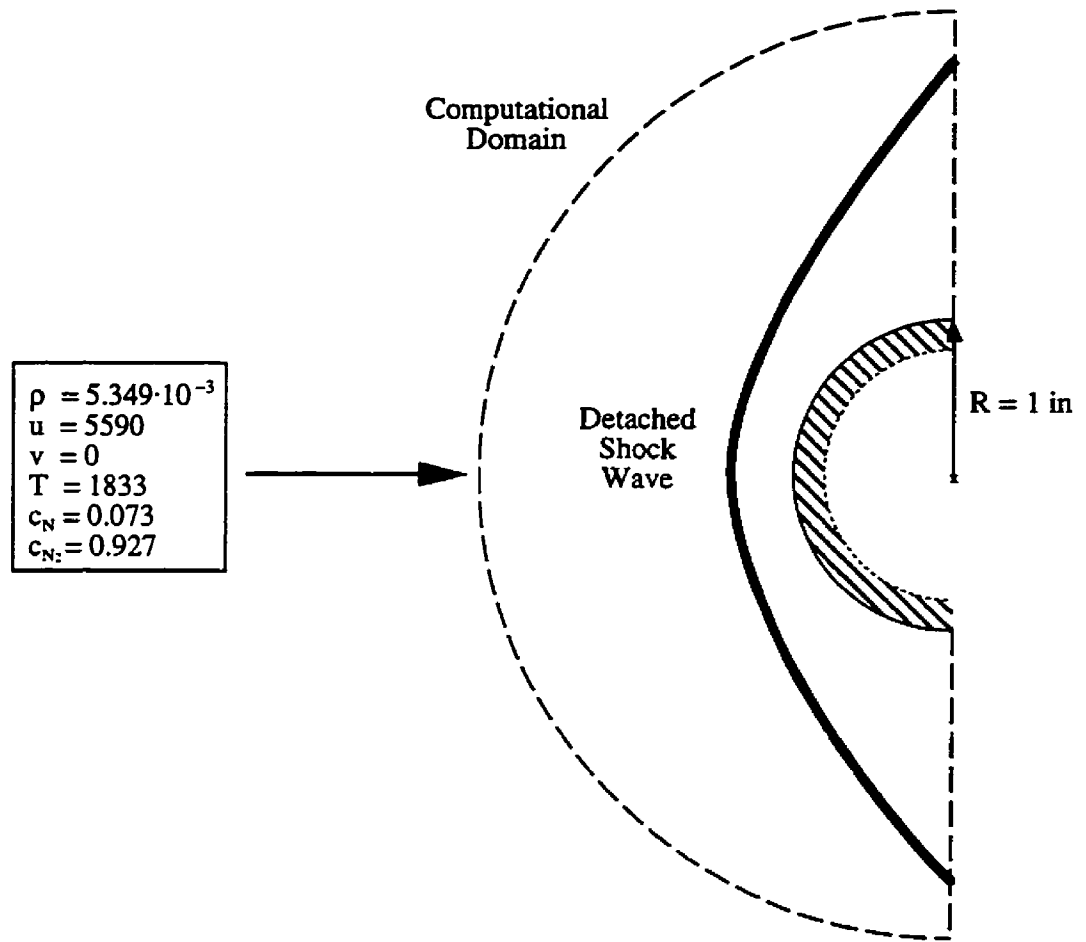


Figure 5.1: Definition of a Mach 6 partially-dissociated nitrogen flow over a half cylinder test case.

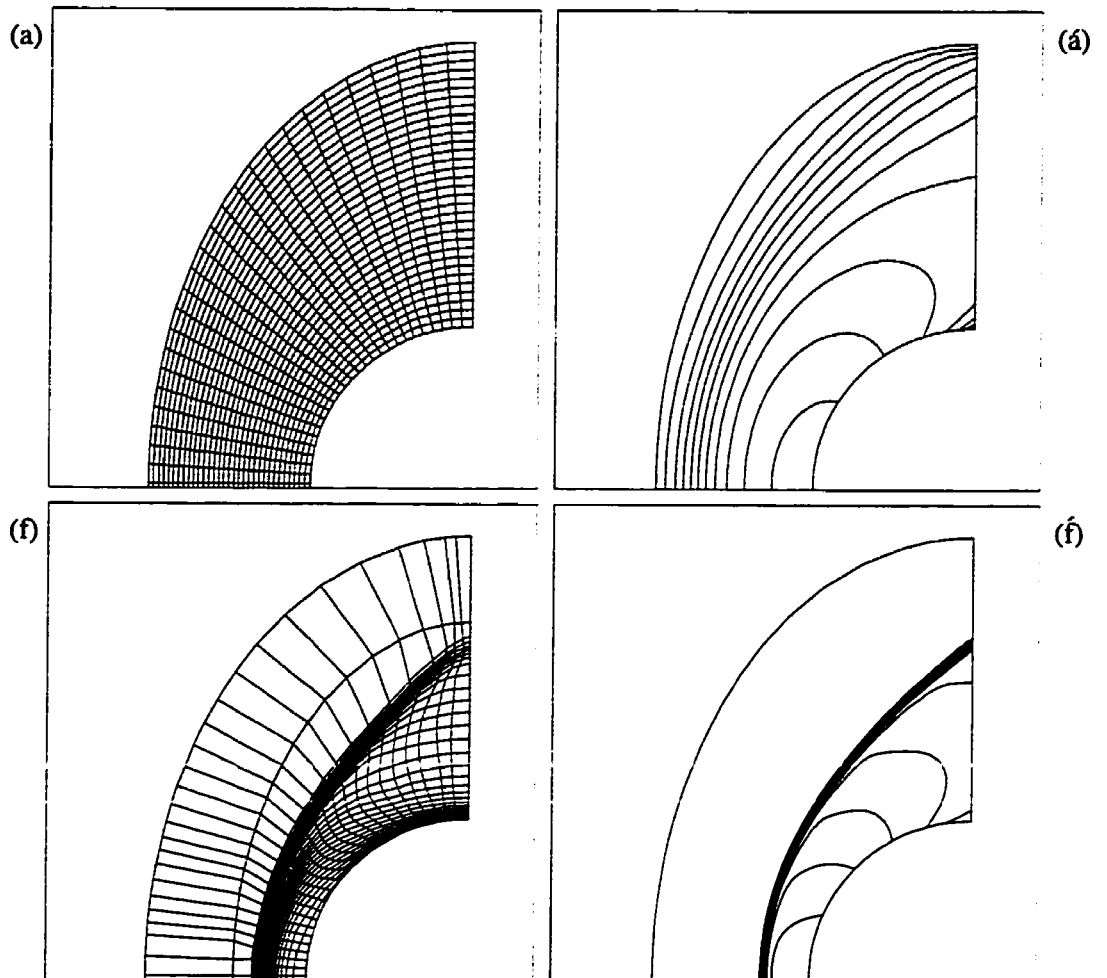


Figure 5.2: Initial and final adapted grids with the corresponding Mach number contours.

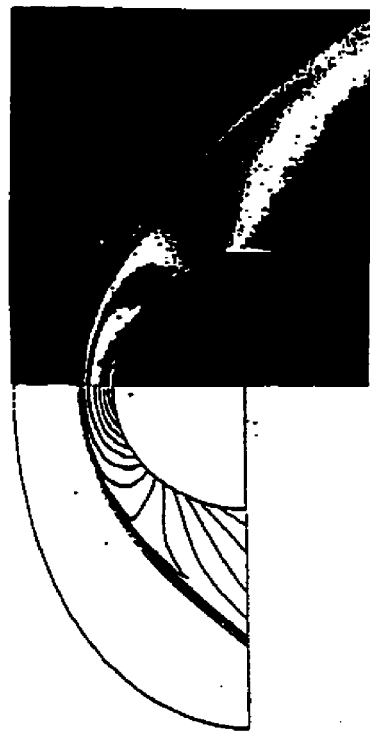


Figure 5.3: Comparison between the interferogram of the flow field (top) and the computed density contours (bottom).

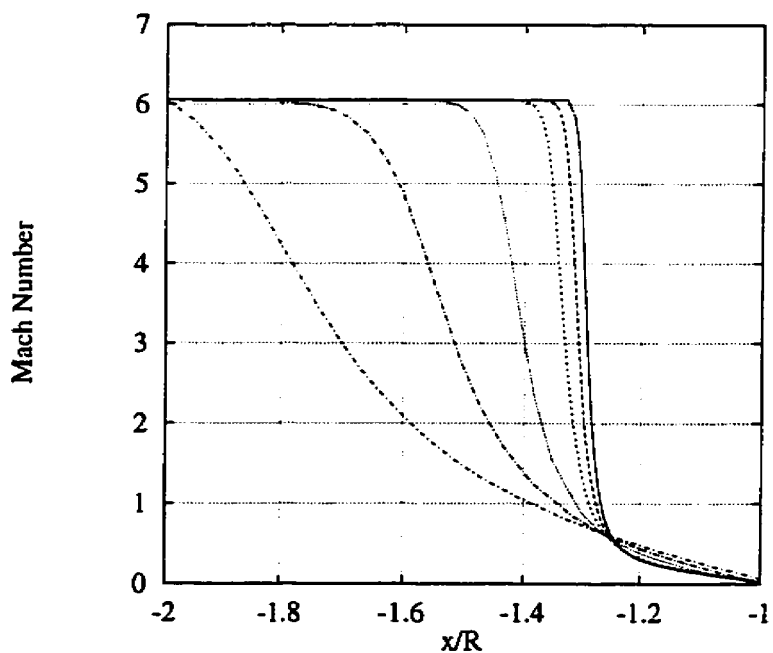


Figure 5.4: Enhancement of the Mach number distribution, along the stagnation line, with grid adaptation cycles.

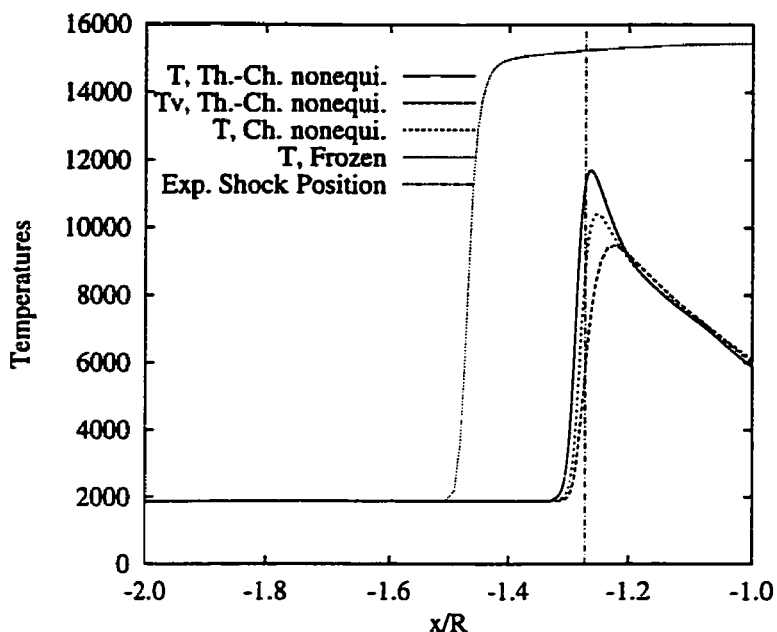


Figure 5.5: Temperature distributions along the stagnation line (Ch. refers to chemical and Th. to thermal).

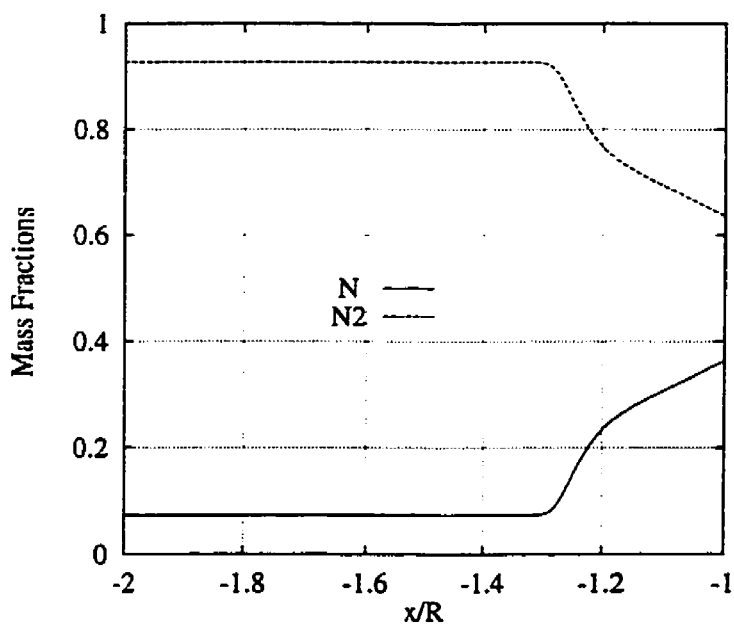


Figure 5.6: Species mass fraction distributions along the stagnation line.

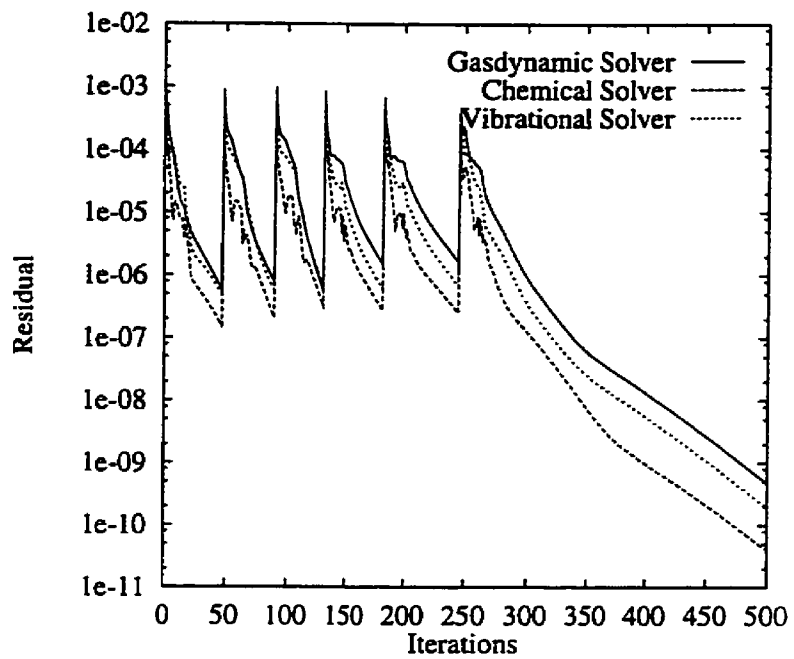


Figure 5.7: Convergence history of the flow solver.

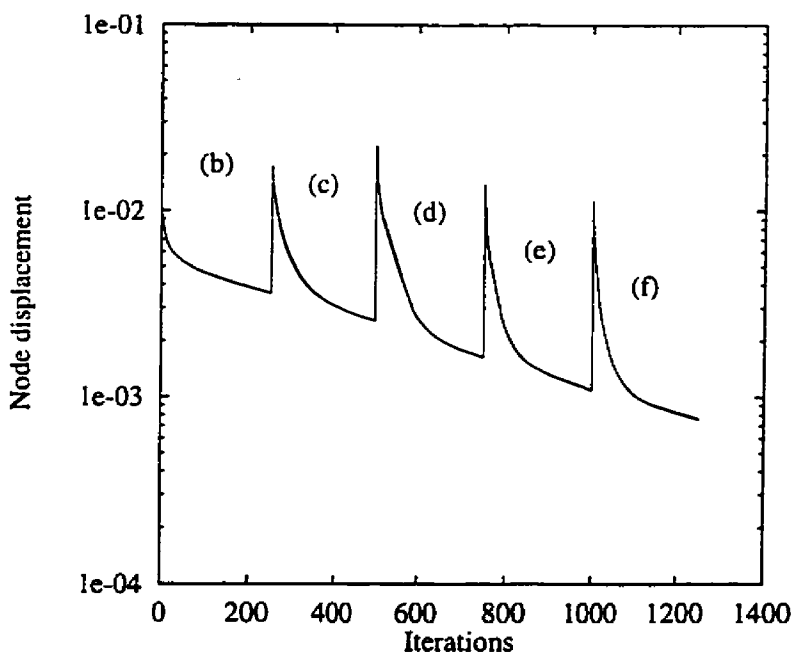


Figure 5.8: Convergence history of the mesh adaptation.

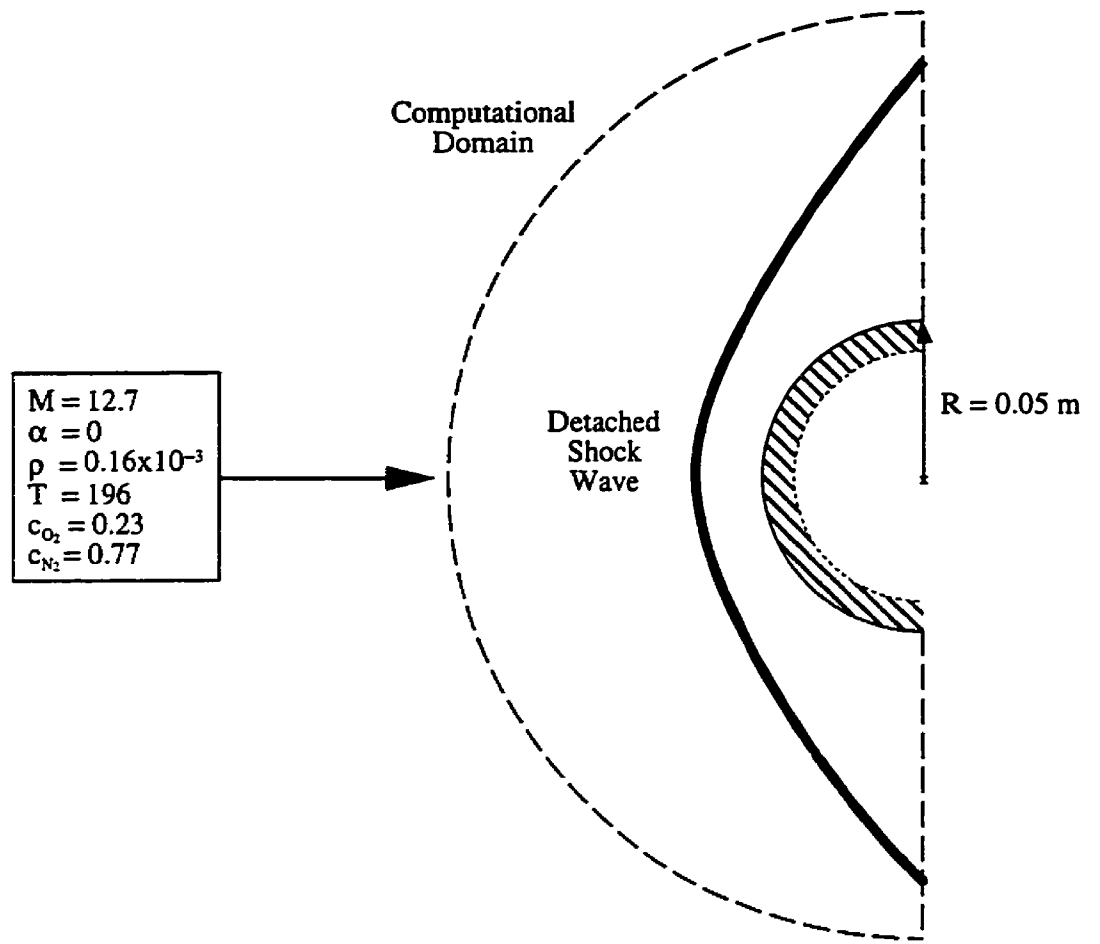


Figure 5.9: Definition of a Mach 12.7 air flow over a half-cylinder test case.

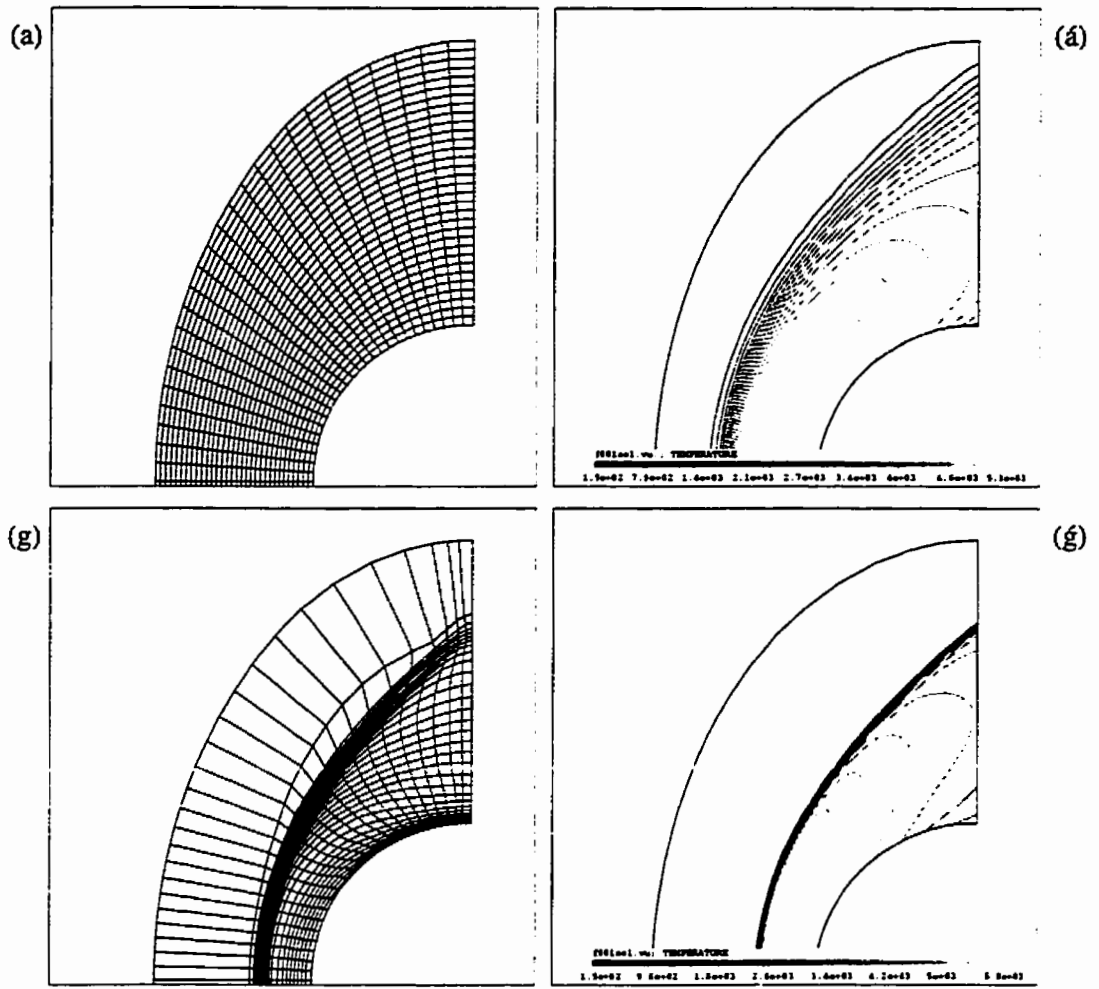


Figure 5.10: Initial and final adapted grid with the corresponding temperature contours.

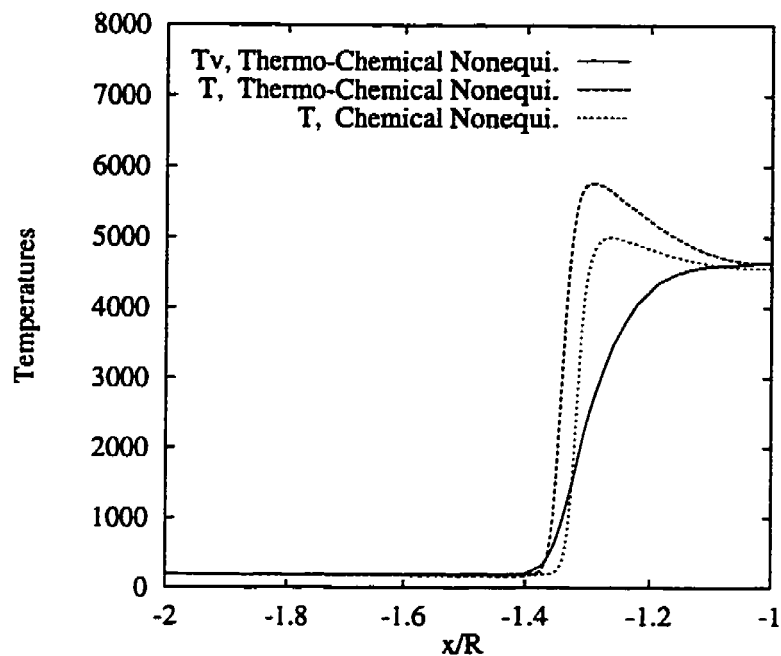


Figure 5.11: Temperature distributions along the stagnation line.

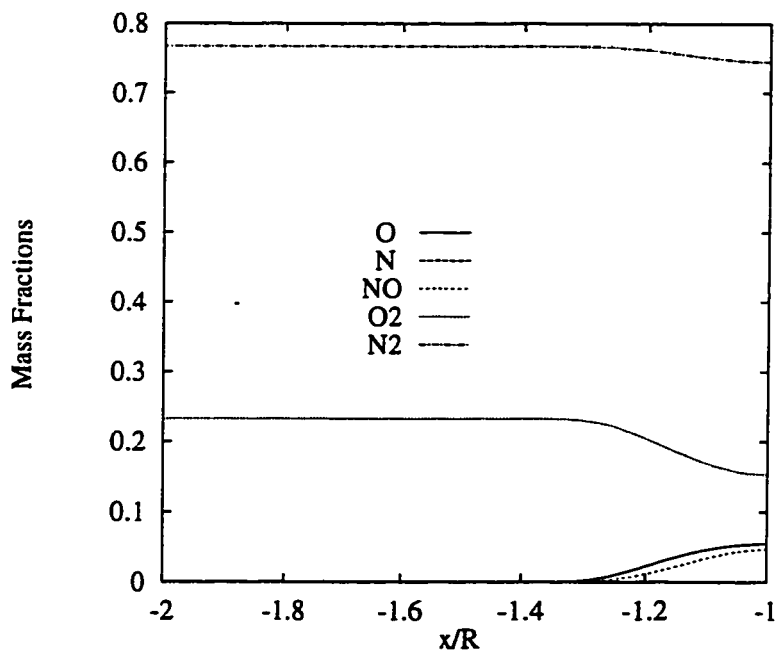


Figure 5.12: Species mass fraction distributions along the stagnation line.

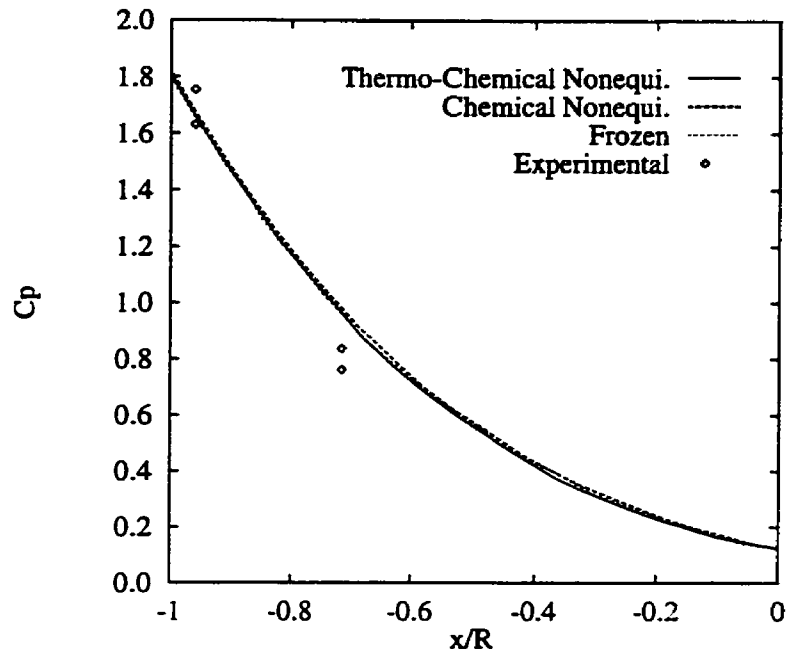


Figure 5.13: Pressure coefficient distribution on the cylinder.

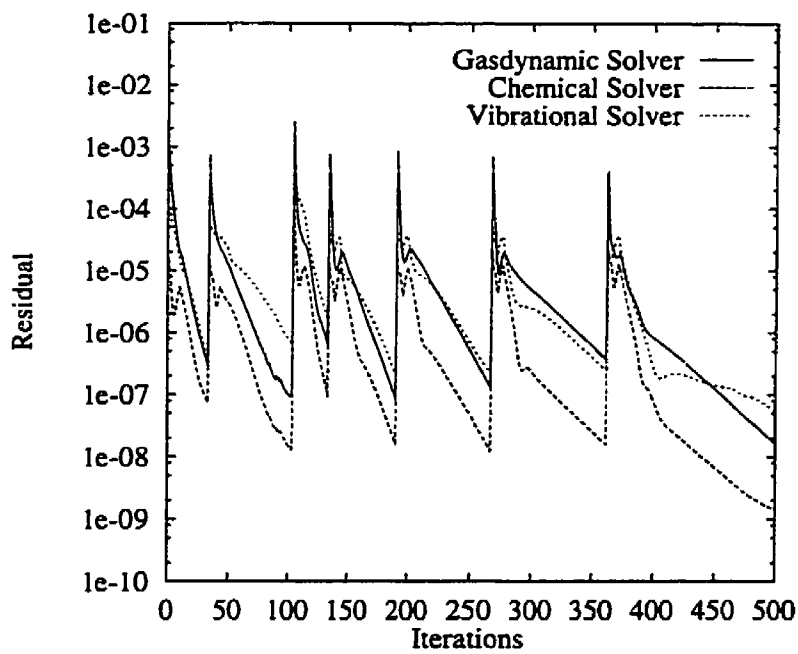


Figure 5.14: Convergence history of the flow solver.

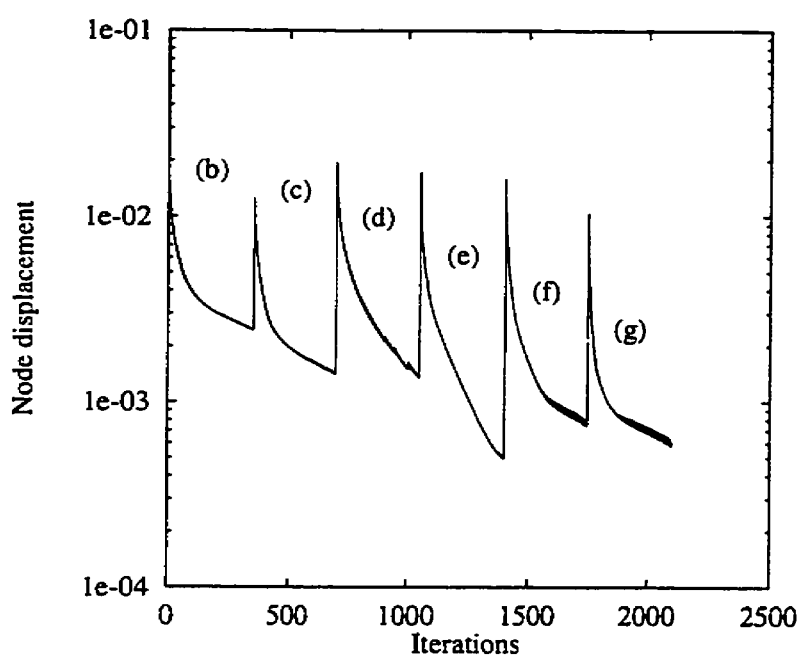


Figure 5.15: Convergence history of the mesh adaptation.

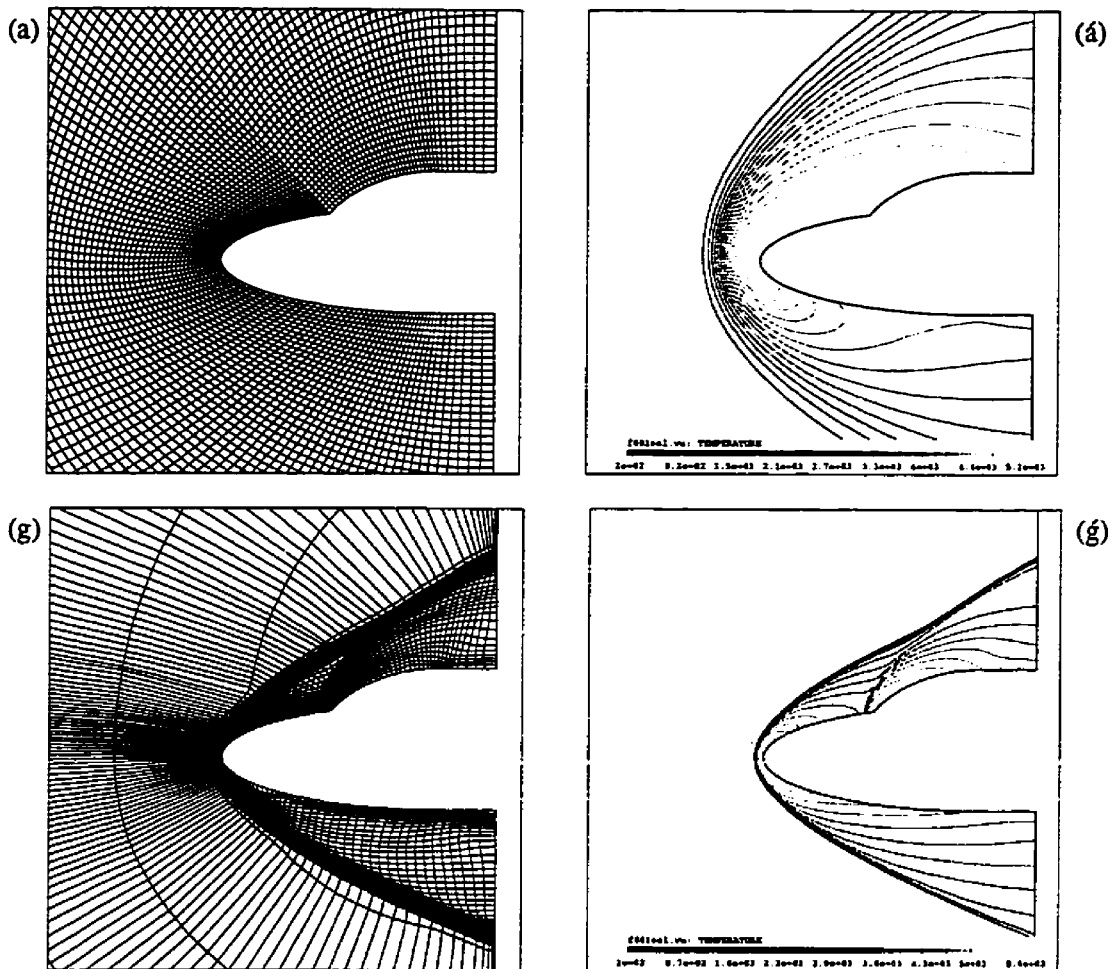


Figure 5.16: Initial and final adapted grids with the corresponding temperature contours.

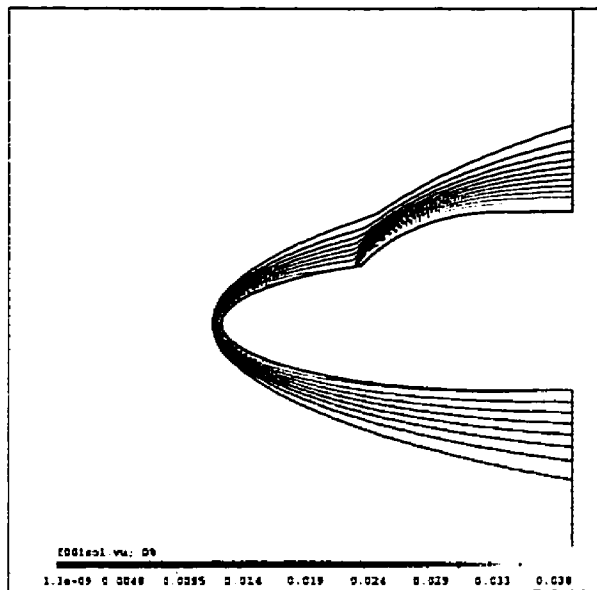


Figure 5.17: Monatomic oxygen mass-fraction contours.

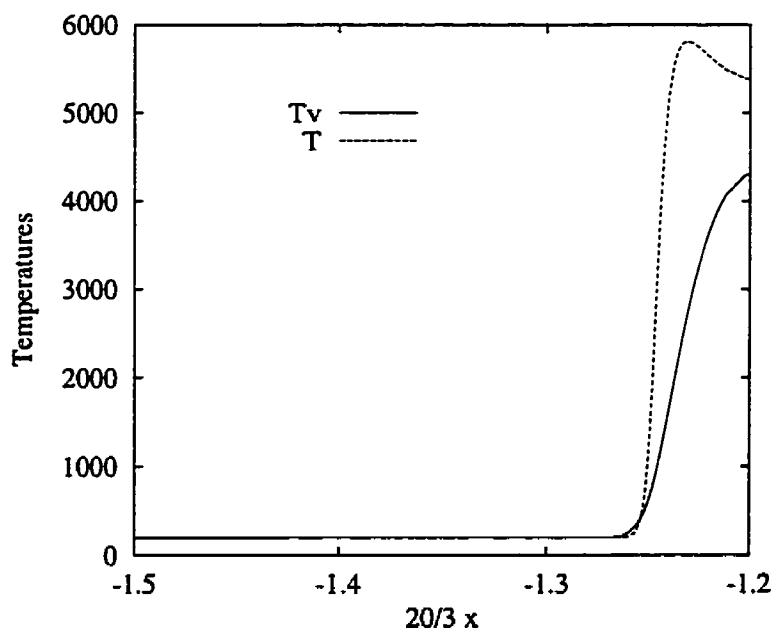


Figure 5.18: Temperature distributions along the stagnation line.

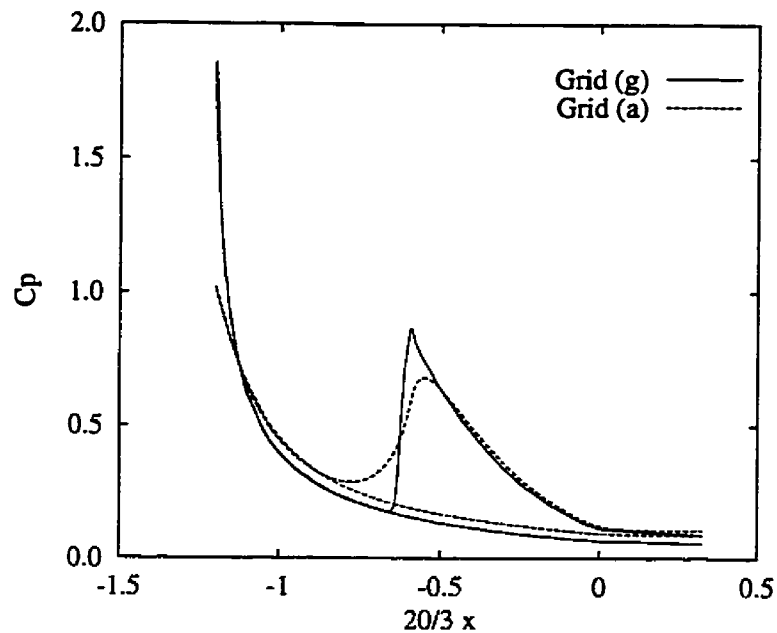


Figure 5.19: Pressure coefficient on the body surface.

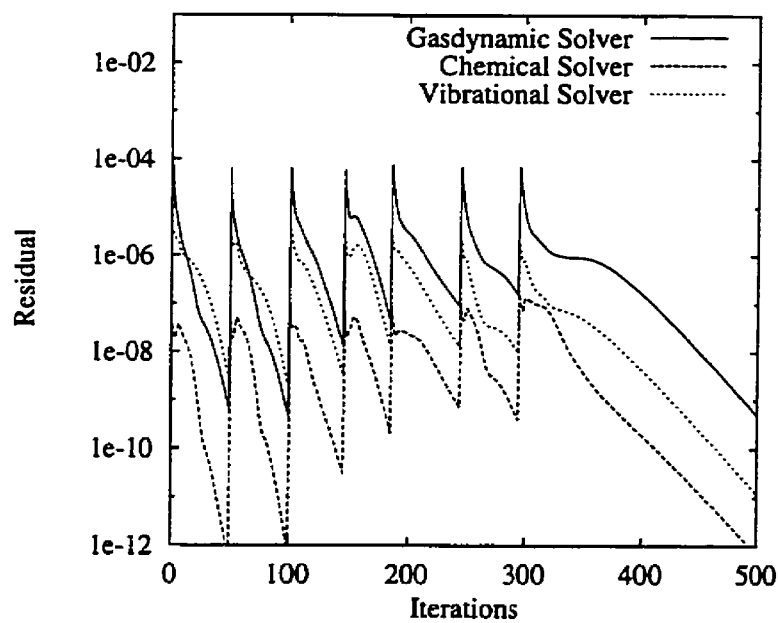


Figure 5.20: Convergence history of the flow solver.

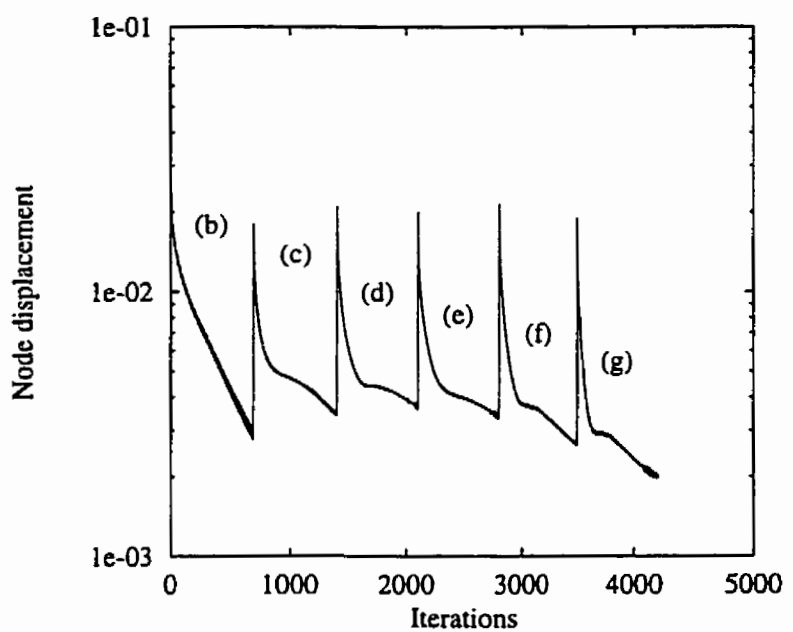


Figure 5.21: Convergence history of the mesh adaptation.

# **Chapter 6**

## **Conclusions and Future Research**

### **6.1 Summary and Conclusions**

In this dissertation, a loosely coupled, finite element method has been described for the numerical simulation of two-dimensional, thermo-chemical equilibrium and nonequilibrium hypersonic flows. An anisotropic mesh adaptation procedure is also presented for resolving directional flow features on quadrilateral grids. The ultimate goal of this work is to produce a flexible numerical tool capable of reproducing accurately a large variety of compressible flow problems ranging from subsonic to hypersonic speeds in a cost-effective manner.

A finite element, weak-Galerkin formulation was first presented for the solution of the Euler equations within the context of divariant gases, wherein two different approaches were suggested in the derivation of the flux Jacobian matrices. The first approach utilizes a general equation of state for a divariant gas and yields an exact form of the Jacobian matrices, while the second alternative uses the perfect gas law, but with an *equivalent ratio of specific heats* to approximate the Jacobian matrices. An artificial dissipation mechanism, that permits the recovery of isoenthalpic flow solutions when needed, is added to the governing equations for damping numerical oscillations that may appear in the solution,

particularly in shock regions.

The shock waves were efficiently resolved by coupling the flow solver with a mesh adaptive procedure. The interpolation error of the numerical solution is measured by its Hessian tensor which is then modified to be a positive definite matrix (metric) and then projected on mesh edges to define a directional estimate of the error. An improved mesh movement scheme is then introduced to equidistribute this error over the edges of the mesh. The optimal mesh may therefore be interpreted as the uniform one in the metric space.

The effectiveness of the adaptive procedure to equidistribute the error on mesh edges was proven on an analytical test case, where a nearly Gaussian distribution of the error is obtained. This example also shows that the current mesh movement scheme is convergent, but there is an inherent threshold below which the error cannot be further reduced. The Euler flow solver, combined with the proposed grid adaptation method is then validated on a supersonic compression corner, capturing the oblique shock with high resolution and the correct angle. This is achieved by aligning and stretching the mesh elements along the oblique shock. The methodology is also tested on hypersonic frozen flows and numerical results using other schemes were correctly reproduced but on coarser meshes.

The Euler solver combined with the mesh adaptation were then extended to thermochemical nonequilibrium flows. Such flows involve gases that are chemically reacting and vibrationally excited and were principally represented by five neutral species: O, N, NO, O<sub>2</sub> and N<sub>2</sub> and a two-temperature thermal model. Following a loosely coupled approach, the governing equations were decoupled to three systems of PDEs –gasdynamic, chemical and vibrational– and marched to steady-state using an implicit technique. This segregated approach has the advantage of reducing reacting flow solutions to a manageable level and offers the possibility of integrating each system of PDEs with the most appropriate time step that produces the best global convergence.

The thermo-chemical equilibrium/nonequilibrium solver is validated on hypersonic, partially-dissociated, nitrogen flow where the shock position is correctly reproduced on a coarse adapted mesh. In addition, the methodology was tested for hypersonic air flows and the prediction of the main flow features required only coarse grids. These test cases also show that the use of a mesh adaptation procedure relieves the user from the tedious task of constructing an appropriate mesh and leads to a nearly optimal mesh that substantially reduces the amount of artificial dissipation needed in the flow solver. In summary, inclusion of the high-temperature effects in a hypersonic flow calculation results in higher density ratio, lower shock layer temperatures and smaller standoff distance, than the perfect gas model. However, its influence on the surface pressure is negligible, as might be expected.

## 6.2 Future Research

It is evident that new horizons for technology advancements in the aerothermal field are becoming more reachable for the aerospace community. With the steady advancement in computer resources, more physical modeling assumptions are eliminated leading to more realistic simulations of high-temperature effects. But before sufficient confidence is achieved in these newly developed technologies to become a full part of the design process, much more studies should be carried out for hypersonic flows. Specifically, several improvements and extensions of the present work are proposed in the following major areas: *physical modeling and numerical techniques*.

Physical modeling extensions are essentially made to enlarge the range of applicability of the present numerical simulation tool. For instance, the hypersonic flow field over a double ellipse is much more complicated than it was described in Section 5.5.3. In fact, the shock layer is highly dominated by viscous effects that may induce strong shock-boundary layer interactions and even flow separation in the canopy shock region. These viscous effects have a great influence on the aerothermal performances of such profiles and should

be accounted for by including the viscous terms into the governing equations.

Another extension of the current thermo-chemical nonequilibrium model could be achieved by considering the ionization phenomena. Those phenomena are present in hypersonic flows with temperatures higher than  $9000\text{ K}$  and should be taken into account for a better prediction of related performance parameters. For example, the formation of an ionized shock layer around a space vehicle may inhibit its communication link with satellites or earth stations, during a crucial part of its reentry trajectory. Therefore, a numerical analysis of such a plasma would allow a characterization of the flow field and be a factor in reducing this black-out communication period.

The present mesh adaptation was used with great success in efficiently resolving directionally flow features on structured and unstructured<sup>1</sup> meshes and it is currently being extended jointly by the CFD Lab at Concordia University, GIREF at Laval University and Pratt & Whitney Canada [115] to 3-D structured hexahedral and unstructured tetrahedral grids. For 2-D problems however, this anisotropic mesh adaptation procedure may further be enhanced by adding quadrilateral refinement/coarsening techniques to the current mesh movement scheme. This improvement will eliminate the dependence of the final adapted solution on the choice of an initial mesh as well as the existence of a threshold error value.

Although, the segregated approach drastically reduced the memory requirements, the use of an implicit integration in time, however, leads to large system of equations which are quite demanding in terms of memory storage. One alternative to overcome this drawback consists of replacing the Gauss elimination method by an iterative solver such as GMRES (Generalized Minimal RESidual) [112]. The iterative solvers have the advantage of storing only the non-zero coefficients and use several preconditioners, such as block diagonal incomplete factorization (ILU0) and successive overrelaxation (SOR) method, that are highly

---

<sup>1</sup>See references [32, 41].

parallelizable [35, 36].

In the current numerical method, the chemical and vibrational time steps are defined in a heuristic manner as

$$\begin{cases} \Delta t^c = \alpha^c \Delta t^g & \text{with } \alpha^c \in [0, 0.5] \\ \Delta t^v = \alpha^v \Delta t^g & \text{with } \alpha^v \in [0, 0.2] \end{cases}$$

Other authors also used heuristic approaches to compute the permissible chemical time step for reacting flow problems. For instance

$$\begin{cases} \Delta t^c \leq \frac{0.1}{|S_s^c|} & \text{by [78]} \\ \Delta t^v \leq 0.1 \left( \min \left| \frac{\rho c_s}{S_s^c} \right| \right) & \text{by [9]} \end{cases}$$

The above time steps are usually very restrictive and may lead to poor convergences that are computationally intensive. The solver convergence may considerably be enhanced by employing more accurate permissible chemical and vibrational time steps that result from applying stability analysis techniques to the chemical and vibrational systems. A good estimate of those time steps may be derived from applying von Neumann stability method to the 1-D linearized chemical and vibrational systems.

# Appendix A

## Chemical Models

### 1.1 Park Reaction Model (1985)

- Forward reaction rate coefficients

$$k_{fr}(T_a) = C_{fr} T_a^{\eta_{fr}} \exp\left(-\frac{\theta_{d,fr}}{T_a}\right) \quad (\text{A.1})$$

where  $T_a = \sqrt{T T_v}$  and the rate constants  $C_{fr}$ ,  $\eta_{fr}$  and  $\theta_{d,fr}$  are given in Table A.1

- Backward reaction rate coefficients

$$k_{br}(T) = \frac{k_{fr}(T)}{k_{eq,r}(T)} \quad (\text{A.2})$$

- Equilibrium constants

$$K_{eq,r} = \exp(A_{1r} + A_{2r}Z + A_{3r}Z^2 + A_{4r}Z^3 + A_{5r}Z^4) \quad (\text{A.3})$$

where  $Z = 10,000/T$  and the constants  $A_{lr}$  are given in Table A.2.

$r$	Reaction	$C_{fr}$	$\eta_{fr}$	$\theta_{d,fr}$
1	$O_2 + O \rightleftharpoons 2O + O$	$8.25 \cdot 10^{16}$	-1.00	59500
2	$O_2 + N \rightleftharpoons 2O + N$	$8.25 \cdot 10^{16}$	-1.00	59500
3	$O_2 + NO \rightleftharpoons 2O + NO$	$2.75 \cdot 10^{16}$	-1.00	59500
4	$O_2 + O_2 \rightleftharpoons 2O + O_2$	$2.75 \cdot 10^{16}$	-1.00	59500
5	$O_2 + N_2 \rightleftharpoons 2O + N_2$	$2.75 \cdot 10^{16}$	-1.00	59500
6	$N_2 + O \rightleftharpoons 2N + O$	$1.11 \cdot 10^{19}$	-1.60	113200
7	$N_2 + N \rightleftharpoons 2N + N$	$1.11 \cdot 10^{19}$	-1.60	113200
8	$N_2 + NO \rightleftharpoons 2N + NO$	$3.70 \cdot 10^{18}$	-1.60	113200
9	$N_2 + O_2 \rightleftharpoons 2N + O_2$	$3.70 \cdot 10^{18}$	-1.60	113200
10	$N_2 + N_2 \rightleftharpoons 2N + N_2$	$3.70 \cdot 10^{18}$	-1.60	113200
11	$NO + O \rightleftharpoons N + O + O$	$4.60 \cdot 10^{14}$	0.50	75500
12	$NO + N \rightleftharpoons N + O + N$	$4.60 \cdot 10^{14}$	0.50	75500
13	$NO + NO \rightleftharpoons N + O + NO$	$2.30 \cdot 10^{14}$	0.50	75500
14	$NO + O_2 \rightleftharpoons N + O + O_2$	$2.30 \cdot 10^{14}$	0.50	75500
15	$NO + N_2 \rightleftharpoons N + O + N_2$	$2.30 \cdot 10^{14}$	0.50	75500
16	$NO + O \rightleftharpoons O_2 + N$	$2.16 \cdot 10^5$	1.29	19200
17	$N_2 + O \rightleftharpoons NO + N$	$3.18 \cdot 10^{10}$	0.10	37700

Table A.1: Arrhenius coefficients for forward rate coefficients.

$r$	$A_{1r}$	$A_{2r}$	$A_{3r}$	$A_{4r}$	$A_{5r}$
1-5	1.335	-4.127	-0.616	0.093	-0.005
6-10	3.898	-12.611	0.683	-0.118	0.006
11-15	1.549	-7.784	0.228	-0.043	0.002
16	0.215	-3.657	0.843	-0.136	0.007
17	2.349	-4.828	0.455	-0.075	0.004

Table A.2: Constants for computing equilibrium reaction constants

## 1.2 Park Reaction Model (1992)

### • Forward reaction rate coefficients

$$k_{fr}(T_a) = C_{fr} T_a^{\eta_{fr}} \exp\left(-\frac{\theta_{d,fr}}{T_a}\right) \quad (\text{A.4})$$

where  $T_a = \sqrt{T T_v}$  and the rate constants  $C_{fr}$ ,  $\eta_{fr}$  and  $\theta_{d,fr}$  are given in Table A.4

### • Backward reaction rate coefficients

$$k_{br}(T_a) = \frac{k_{fr}(T_a)}{k_{eq,r}(T_a)} \quad (\text{A.5})$$

Species	O	N	NO	O <sub>2</sub>	N <sub>2</sub>
$\theta_{us}$	—	—	2817	2239	3395
$h_s^o$	$1.543119 \cdot 10^7$	$3.362161 \cdot 10^7$	$2.996123 \cdot 10^6$	0	0

Table A.3: Characteristic vibrational temperatures and heats of formation.

### • Equilibrium constants

$$K_{eq,r} = \exp(A_{1r}Z + A_{2r} + A_{3r} \ln(1/Z) + A_{4r}/Z + A_{5r}/Z^2). \quad (\text{A.6})$$

where  $Z = 10,000/T_a$  and the constants  $A_{lr}$  are given in Table A.5.

$r$	Reaction					$C_{fr}$	$\eta_{fr}$	$\theta_{d,fr}$
1	O <sub>2</sub>	+	O	$\rightleftharpoons$	2O	+	O	$1.00 \cdot 10^{19}$
2	O <sub>2</sub>	+	N	$\rightleftharpoons$	2O	+	N	$1.00 \cdot 10^{19}$
3	O <sub>2</sub>	+	NO	$\rightleftharpoons$	2O	+	NO	$2.00 \cdot 10^{18}$
4	O <sub>2</sub>	+	O <sub>2</sub>	$\rightleftharpoons$	2O	+	O <sub>2</sub>	$2.00 \cdot 10^{18}$
5	O <sub>2</sub>	+	N <sub>2</sub>	$\rightleftharpoons$	2O	+	N <sub>2</sub>	$2.00 \cdot 10^{18}$
6	N <sub>2</sub>	+	O	$\rightleftharpoons$	2N	+	O	$3.00 \cdot 10^{19}$
7	N <sub>2</sub>	+	N	$\rightleftharpoons$	2N	+	N	$3.00 \cdot 10^{19}$
8	N <sub>2</sub>	+	NO	$\rightleftharpoons$	2N	+	NO	$7.00 \cdot 10^{18}$
9	N <sub>2</sub>	+	O <sub>2</sub>	$\rightleftharpoons$	2N	+	O <sub>2</sub>	$7.00 \cdot 10^{18}$
10	N <sub>2</sub>	+	N <sub>2</sub>	$\rightleftharpoons$	2N	+	N <sub>2</sub>	$7.00 \cdot 10^{18}$
11	NO	+	O	$\rightleftharpoons$	O <sub>2</sub>	+	N	$2.20 \cdot 10^6$
12	N <sub>2</sub>	+	O	$\rightleftharpoons$	NO	+	N	$1.80 \cdot 10^{11}$

Table A.4: Arrhenius coefficients for forward rate coefficients.

$r$	$A_{1r}$	$A_{2r}$	$A_{3r}$	$A_{4r}$	$A_{5r}$
1-5	0.553880	16.27551	1.77630	-6.57200	0.031445
6-10	1.535100	15.42160	1.29930	-11.4940	-0.006980
11	0.004815	-1.74430	-1.22270	-0.95824	-0.045545
12	0.976460	0.89043	0.74572	-3.96420	0.007123

Table A.5: Constants for computing equilibrium reaction constants

Species	O	N	NO	O <sub>2</sub>	N <sub>2</sub>
$\theta_{vs}$	—	—	2740	2273	3393
$h_v^o$	$1.5425625 \cdot 10^7$	$3.3609425 \cdot 10^7$	$2.992501 \cdot 10^6$	0	0

Table A.6: Characteristic vibrational temperatures and heats of formation.

## Appendix B

# Jacobian Matrices for Chemical Nonequilibrium Flow Solver

In the case of chemical nonequilibrium flows, the two systems of PDEs –gasdynamics and chemical– are solved in a decoupled manner for the following primitive variables:

$$\mathbf{U} = \{\mathbf{U}^g, \mathbf{U}^c\}$$

or

$$\mathbf{U} = \{[\rho, v_i (i = 1, 2), e], [c_s (s = 1, 3)]\}$$

The translational-rotational temperature  $T$  is deduced from the total internal energy  $e$  and the pressure  $p$  is given by the Dalton's law.

The remaining mass fractions,  $c_4$  and  $c_5$ , are computed from the following two algebraic

equations:

$$\begin{cases} c_4 &= \frac{24}{103} - c_1 - \frac{8}{15}c_3, \\ c_5 &= \frac{79}{103} - c_2 - \frac{7}{15}c_3. \end{cases} \quad (\text{B.1})$$

## 2.1 Jacobian Matrix of the Chemical Source Vector

We recall that for the species  $s$ , the chemical rate of production is given by

$$S_s(\mathcal{C}, T) = \mathcal{M}_s \sum_{r=1}^{N_r} (\nu_{sr}'' - \nu_{sr}') R_r(\mathcal{C}, T) \quad (\text{B.2})$$

where

$$\mathcal{C} = \{[\rho, v_i (i = 1, 2), e], [c_s (s = 1, 3)], [c_s (s = 4, 5)]\}, \quad (\text{B.3})$$

$$R_r(\mathcal{C}, T) = R_{fr}(\mathcal{C}, T) - R_{br}(\mathcal{C}, T), \quad (\text{B.4})$$

and

$$\begin{cases} R_{fr}(\mathcal{C}, T) &= k_{fr}(T) \prod_{l=1}^{N_s} \left( \frac{\rho c_l}{\mathcal{M}_l} \right)^{\nu_{lr}'} \\ R_{br}(\mathcal{C}, T) &= k_{br}(T) \prod_{l=1}^{N_s} \left( \frac{\rho c_l}{\mathcal{M}_l} \right)^{\nu_{lr}''} \end{cases} \quad (\text{B.5})$$

The Jacobian matrix of the chemical source vector is defined as

$$\mathbf{B}^c = \frac{\partial \mathbf{S}^c}{\partial \mathbf{U}^c} \quad (\text{B.6})$$

or

$$\frac{\partial S_s^c}{\partial c_i} = \mathcal{M}_s \sum_{r=1}^{N_r} (\nu_{sr}'' - \nu_{sr}') \frac{\partial R_r}{\partial c_i} \quad \text{with } i = 1, 3 \quad (\text{B.7})$$

Using the chain rule for partial derivatives, we have

$$\begin{aligned} \left[ \frac{\partial R_r}{\partial c_i} \right]_{U_{c_s \neq c_i}} &= \left[ \frac{\partial R_r}{\partial c_i} \right]_{U_{c_s \neq c_i, c_4, c_5, T}} + \left[ \frac{\partial R_r}{\partial c_4} \right]_{U_{c_s \neq c_i, c_5, T}} \left[ \frac{\partial c_4}{\partial c_i} \right]_{U_{c_s \neq c_i, c_5, T}} \\ &\quad + \left[ \frac{\partial R_r}{\partial c_5} \right]_{U_{c_4, T}} \left[ \frac{\partial c_5}{\partial c_i} \right]_{U_{c_s \neq c_i, c_4, T}} \\ &\quad + \left[ \frac{\partial R_r}{\partial T} \right]_{U_{c_4, c_5}} \left[ \frac{\partial T}{\partial c_i} \right]_{U_{c_s \neq c_i, c_4, c_5}} \end{aligned} \quad (\text{B.8})$$

The above equation can also be rewritten in a more compact form as

$$\begin{aligned} \left[ \frac{\partial R_r}{\partial c_i} \right]_{U_{c_s \neq c_i}} &= \sum_{j=1}^{N_s} \left[ \frac{\partial R_r}{\partial c_j} \right]_{C_{c_s \neq c_j, T}} \left[ \frac{\partial c_j}{\partial c_i} \right]_{C_{c_s \neq c_i, T}} \\ &\quad + \left[ \frac{\partial R_r}{\partial T} \right]_C \left[ \frac{\partial T}{\partial c_i} \right]_{C_{c_s \neq c_i}} \end{aligned} \quad (\text{B.9})$$

**Derivation of  $\left[ \frac{\partial R_r}{\partial c_j} \right]_{C_{c_s \neq c_j, T}}$**

$$\left[ \frac{\partial R_r}{\partial c_j} \right]_{C_{c_s \neq c_j, T}} = k_{fr} \frac{\partial}{\partial c_j} \left[ \prod_{l=1}^{N_s} \left( \frac{\rho c_l}{M_l} \right)^{\nu'_{lr}} \right] - k_{br} \frac{\partial}{\partial c_j} \left[ \prod_{l=1}^{N_s} \left( \frac{\rho c_l}{M_l} \right)^{\nu''_{lr}} \right] \quad (\text{B.10})$$

After simplifications, we obtain

$$\left[ \frac{\partial R_r}{\partial c_j} \right]_{C_{c_s \neq c_j, T}} = \frac{1}{c_j} (\nu'_{jr} R_{fr} - \nu''_{jr} R_{br}) \quad (\text{B.11})$$

**Derivation of  $\left[ \frac{\partial c_j}{\partial c_i} \right]_{C_{c_s \neq c_i, T}}$**

For  $j = N_s$  and  $i = 1, 3$ , the equations (B.1) gives

$$\frac{\partial c_j}{\partial c_i} = \begin{bmatrix} 1 & 0 & 0 \\ 0 & 1 & 0 \\ 0 & 0 & 1 \\ -1 & 0 & -8/15 \\ 0 & -1 & -7/15 \end{bmatrix} \quad (\text{B.12})$$

If the dependence between the mass fractions variables,  $c_s$ , is neglected, i.e.

$$\frac{\partial c_j}{\partial c_i} = \delta_{ij}, \quad (\text{B.13})$$

the first term of the RHS of the equation (B.9) reduces to

$$\sum_{j=1}^{N_s} \left[ \frac{\partial R_r}{\partial c_j} \right]_{C_{c_s \neq c_j, T}} \left[ \frac{\partial c_j}{\partial c_i} \right]_{C_{c_s \neq c_i, T}} = \frac{1}{c_i} (\nu'_{ir} R_{fr} - \nu''_{ir} R_{br}). \quad (\text{B.14})$$

**Derivation of  $\left[ \frac{\partial R_r}{\partial T} \right]_C$**

In the following derivations, some subscripts will be omitted for simplicity. Using the equation (B.4), one obtains

$$\left[ \frac{\partial R_r}{\partial T} \right] = \frac{\partial k_{fr}}{\partial T} \prod_{l=1}^{N_s} \left( \frac{\rho c_l}{M_l} \right)^{\nu'_{lr}} - \frac{\partial k_{br}}{\partial T} \prod_{l=1}^{N_s} \left( \frac{\rho c_l}{M_l} \right)^{\nu''_{lr}} \quad (\text{B.15})$$

where the forward rate of reaction is given by:

$$k_{fr}(T) = C_{fr} T^{\eta_{fr}} \exp \left( -\frac{\theta_{d,fr}}{T} \right), \quad (\text{B.16})$$

and therefore

$$\frac{\partial k_{fr}}{\partial T} = k_{fr} \left( \frac{\eta_{fr}}{T} + \frac{\theta_{d,fr}}{T^2} \right). \quad (\text{B.17})$$

The backward rate of reaction is given by

$$k_{br}(T) = \frac{k_{fr}(T)}{k_{eqr}(T)}, \quad (\text{B.18})$$

and therefore

$$\frac{\partial k_{br}}{\partial T} = \frac{1}{K_{eqr}} \left( \frac{\partial k_{fr}}{\partial T} - k_{br} \frac{\partial K_{eqr}}{\partial T} \right). \quad (\text{B.19})$$

For instance, the equilibrium constant for Park's reaction model (1985) is given by

$$K_{eq,r}(Z) = \exp(A_{1r} + A_{2r}Z + A_{3r}Z^2 + A_{4r}Z^3 + A_{5r}Z^4), \quad (B.20)$$

where  $Z = 10,000/T$ .

The derivative of  $K_{eq,r}$  with respect to  $T$  may be expressed as

$$\frac{\partial K_{eq,r}}{\partial T} = \frac{\partial K_{eq,r}}{\partial Z} \frac{\partial Z}{\partial T}, \quad (B.21)$$

with

$$\begin{cases} \frac{\partial K_{eq,r}}{\partial Z} &= (A_{2r} + 2A_{3r}Z + 3A_{4r}Z^2 + 4A_{5r}Z^3) K_{eq,r} \\ \frac{\partial Z}{\partial T} &= -\frac{Z^2}{10,000} \end{cases} \quad (B.22)$$

Equation (B.21) becomes

$$\frac{\partial K_{eq,r}}{\partial T} = -10^{-4}(A_{2r}Z^2 + 2A_{3r}Z^3 + 3A_{4r}Z^4 + 4A_{5r}Z^5) K_{eq,r}. \quad (B.23)$$

After substituting equations (B.17) and (B.23) into (B.19), one obtains

$$\frac{\partial K_{br}}{\partial T} = k_{br} \left( \frac{\eta_{fr}}{T} + \frac{\theta_{d,fr}}{T^2} + 10^{-4}(A_{2r}Z^2 + 2A_{3r}Z^3 + 3A_{4r}Z^4 + 4A_{5r}Z^5) \right), \quad (B.24)$$

and finally

$$\left[ \frac{\partial R_r}{\partial T} \right]_C = \left( \frac{\eta_{fr}}{T} + \frac{\theta_{d,fr}}{T^2} \right) R_r - 10^{-4}(A_{2r}Z^2 + 2A_{3r}Z^3 + 3A_{4r}Z^4 + 4A_{5r}Z^5) R_{br}. \quad (B.25)$$

$$\text{Derivation of } \left[ \frac{\partial T}{\partial c_i} \right]_{C_{c_s \neq c_i}}$$

Recall that the total internal energy of a gas mixture is given by

$$e = \sum_{j=1}^{N_s} c_j c_{v,j} T + \sum_{j=1}^{N_s} c_j h_j^o + \sum_{j=3}^{N_s} c_j e_{v,j} + \frac{1}{2} v^2, \quad (\text{B.26})$$

where

$$e_{v,j} = \frac{R_j \theta_{v,j}}{\exp(\theta_{v,j}/T) - 1} \quad (\text{B.27})$$

By taking the derivative of equation (B.26) with respect to  $T$  and solve for  $\frac{\partial T}{\partial c_i}$ , we obtain

$$\left[ \frac{\partial T}{\partial c_i} \right] = - \frac{\sum_{j=1}^{N_s} \left( \frac{\partial c_j}{\partial c_i} \right) c_{v,j} T + \sum_{j=1}^{N_s} \left( \frac{\partial c_j}{\partial c_i} \right) h_j^o + \sum_{j=3}^{N_s} \left( \frac{\partial c_j}{\partial c_i} \right) e_{v,j}}{\bar{c}_v + \sum_{j=3}^{N_s} \frac{c_j \exp(\theta_{v,j}/T)}{R_j T^2} e_{v,j}^2} \quad (\text{B.28})$$

If  $\partial c_j / \partial c_i = \delta_{ij}$  is assumed, the equation (B.28) simplifies to

$$\left[ \frac{\partial T}{\partial c_i} \right] = - \frac{c_{vi} T + h_i^o + e_{vi}}{\bar{c}_v + \sum_{j=3}^{N_s} \frac{c_j \exp(\theta_{v,j}/T)}{R_j T^2} e_{v,j}^2}. \quad (\text{B.29})$$

## Appendix C

# Jacobian Matrices for Thermo-Chemical Nonequilibrium Flow Solver

Recalling that for thermo-chemical nonequilibrium flows, three systems of PDEs – gasdynamics, chemical and vibrational– are solved in a segregated fashion for the three primitive vectors,

$$\mathbf{U} = \{\mathbf{U}^g, \mathbf{U}^c, \mathbf{U}^v\}$$

or

$$\mathbf{U} = \{[\rho, v_i(i=1, 2), e], [c_s(s=1, 3)], [e_v]\}.$$

The vibrational temperature  $T_v$  is deduced from the vibrational energy of the mixture  $e_v$ , the translational-rotational temperature  $T$  from the total internal energy  $e$  and the pressure  $p$  is given by the Dalton's law.

The mass fractions,  $c_4$  and  $c_5$ , are given by the two algebraic equations:

$$\begin{cases} c_4 = \frac{24}{103} - c_1 - \frac{8}{15}c_3, \\ c_5 = \frac{79}{103} - c_2 - \frac{7}{15}c_3. \end{cases} \quad (\text{C.1})$$

### 3.1 Jacobian Matrix of the Chemical Source Vector

We recall that for the species  $s$ , the chemical rate of production is given by

$$S_s^c(\mathbf{C}, T_a) = \mathcal{M}_s \sum_{r=1}^{N_r} (\nu_{sr}'' - \nu_{sr}') R_r(\mathbf{C}, T_a) \quad (\text{C.2})$$

where

$$\begin{cases} \mathbf{C} &= \{[\rho, v_i (i = 1, 2), e], [c_s (s = 1, 3)], [e_v], [c_s (s = 4, 5)]\}, \\ T_a &= \sqrt{T T_v}, \end{cases} \quad (\text{C.3})$$

$$R_r(\mathbf{C}, T_a) = R_{fr}(\mathbf{C}, T_a) - R_{br}(\mathbf{C}, T_a), \quad (\text{C.4})$$

and

$$\begin{cases} R_{fr}(\mathbf{C}, T_a) &= k_{fr}(T_a) \prod_{l=1}^{N_s} \left( \frac{\rho c_l}{\mathcal{M}_l} \right)^{\nu_{lr}'} \\ R_{br}(\mathbf{C}, T_a) &= k_{br}(T_a) \prod_{l=1}^{N_s} \left( \frac{\rho c_l}{\mathcal{M}_l} \right)^{\nu_{lr}''} \end{cases} \quad (\text{C.5})$$

The Jacobian matrix of the chemical source vector is defined as

$$\mathbf{B}^c = \frac{\partial S^c}{\partial \mathbf{U}^c} \quad (\text{C.6})$$

or

$$\frac{\partial S_s^c}{\partial c_i} = \mathcal{M}_s \sum_{r=1}^{N_r} (\nu_{sr}'' - \nu_{sr}') \frac{\partial R_r}{\partial c_i} \quad \text{with } i = 1, 3 \quad (\text{C.7})$$

Using the chain rule for partial derivatives, we have

$$\left[ \frac{\partial R_r}{\partial c_i} \right]_{U_{c_s \neq c_i}} = \left[ \frac{\partial R_r}{\partial c_i} \right]_{U_{c_s \neq c_i, c_4, c_5, T_a}} + \left[ \frac{\partial R_r}{\partial c_4} \right]_{U_{c_s, c_5, T_a}} \left[ \frac{\partial c_4}{\partial c_i} \right]_{U_{c_s \neq c_i, c_5, T_a}} \\ + \left[ \frac{\partial R_r}{\partial c_5} \right]_{U_{c_4, T_a}} \left[ \frac{\partial c_5}{\partial c_i} \right]_{U_{c_s \neq c_i, c_4, T_a}} \\ + \left[ \frac{\partial R_r}{\partial T_a} \right]_{U_{c_4, c_5}} \left[ \frac{\partial T_a}{\partial c_i} \right]_{U_{c_s \neq c_i, c_4, c_5}} \quad (C.8)$$

The above equation can also be written in the form

$$\left[ \frac{\partial R_r}{\partial c_i} \right]_{U_{c_s \neq c_i}} = \sum_{j=1}^{N_s} \left[ \frac{\partial R_r}{\partial c_j} \right]_{C_{c_s \neq c_j, T_a}} \left[ \frac{\partial c_j}{\partial c_i} \right]_{C_{c_s \neq c_i, T_a}} \\ + \left[ \frac{\partial R_r}{\partial T_a} \right]_C \left[ \frac{\partial T_a}{\partial c_i} \right]_{C_{c_s \neq c_i}} \quad (C.9)$$

All terms that appeared in the RHS of the equation (C.9), except  $\left[ \frac{\partial T_a}{\partial c_i} \right]$ , were already derived in Appendix B, where the translational-rotational temperature  $T$  should be replaced by the rate controlling temperature  $T_a$ .

The chain rule for partial derivatives gives

$$\left[ \frac{\partial T_a}{\partial c_i} \right] = \left( \frac{\partial T_a}{\partial T} \right) \left( \frac{\partial T}{\partial c_i} \right) + \left( \frac{\partial T_a}{\partial T_v} \right) \left( \frac{\partial T_v}{\partial c_i} \right), \quad (C.10)$$

where

$$\begin{cases} \left( \frac{\partial T_a}{\partial T} \right) = \frac{T_a}{2T} \\ \left( \frac{\partial T_a}{\partial T_v} \right) = \frac{T}{2T_a} \end{cases} \quad (C.11)$$

**Derivation of  $\left(\frac{\partial T}{\partial c_i}\right)$**

Recall that the total internal energy of a mixture is given by,

$$e = \sum_{j=1}^{N_s} c_j c_{v,j} T + \sum_{j=1}^{N_s} c_j h_j^0 + e_v + \frac{1}{2} v^2 \quad (\text{C.12})$$

By taking the derivative of equation (C.12) with respect to  $T$  and solving for  $\left(\frac{\partial T}{\partial c_i}\right)$ , one obtains

$$\frac{\partial T}{\partial c_i} = -\frac{1}{\bar{c}_v} \sum_{j=1}^{N_s} (c_{v,j} T + h_j^0) \frac{\partial c_j}{\partial c_i}. \quad (\text{C.13})$$

**Derivation of  $\left(\frac{\partial T_v}{\partial c_i}\right)$**

The vibrational energy for a gas mixture is expressed by

$$\begin{aligned} e_v &= \sum_{j=3}^{N_s} c_j e_{v,j} \\ &= \sum_{j=3}^{N_s} \frac{c_j R_j \theta_{v,j}}{\exp(\theta_{v,j}/T_v) - 1} \end{aligned} \quad (\text{C.14})$$

Taking the derivative of the equation (C.14) with respect to  $T_v$  and solving for  $\left(\frac{\partial T_v}{\partial c_i}\right)$  yields to

$$\frac{\partial T_v}{\partial c_i} = - \frac{\sum_{j=3}^{N_s} \left(\frac{\partial c_j}{\partial c_i}\right) e_{v,j}}{\sum_{j=3}^{N_s} \frac{c_j \exp(\theta_{v,j}/T_v)}{R_j T_v^2} e_{v,j}^2}. \quad (\text{C.15})$$

## 3.2 Jacobian Matrix of the Vibrational Source Term

The source term of the conservation equation for the vibrational energy of a mixture is given by

$$S^v(\mathcal{C}, T, T_v, p) = S_{T-v}(\mathcal{C}, T, T_v, p) + S_{c-v}(\mathcal{C}, T, T_v) \quad (\text{C.16})$$

where

$$\begin{cases} S_{T-v}(\mathbf{C}, T, Tv, p) &= \sum_{s=3}^{N_s} Q_{T-v,s}(\mathbf{C}, T, Tv, p) \\ S_{c-v}(\mathbf{C}, T, Tv) &= \sum_{s=3}^{N_s} S_s^c(\mathbf{C}, T, Tv) e_{vs}(Tv) \end{cases} \quad (\text{C.17})$$

The Jacobian matrix of the vibrational source term is defined as

$$\mathbf{B}^c = \frac{\partial \mathbf{S}^v}{\partial \mathbf{U}^v} \quad (\text{C.18})$$

or

$$\left[ \frac{\partial S^v}{\partial e_v} \right]_{\mathbf{U}^v, \mathbf{C}} = \left[ \frac{\partial S_{T-v}}{\partial e_v} \right]_{\mathbf{U}^v, \mathbf{C}} + \left[ \frac{\partial S_{c-v}}{\partial e_v} \right]_{\mathbf{U}^v, \mathbf{C}} \quad (\text{C.19})$$

### 3.2.1 Translational-Vibrational Exchange Contribution

$$\left[ \frac{\partial S_{T-v}}{\partial e_v} \right]_{\mathbf{U}^v, \mathbf{C}} = \sum_{s=3}^{N_s} \left[ \frac{\partial Q_{T-v,s}}{\partial e_v} \right]_{\mathbf{U}^v, \mathbf{C}} \quad (\text{C.20})$$

where

$$Q_{T-v,s}(\mathbf{C}, T, Tv, p) = \rho c_s \frac{e_{vs}^*(T) - e_{vs}(Tv)}{\tau_{vs}}, \quad (\text{C.21})$$

and  $\tau_{vs} = \langle \tau_s^{L-T} \rangle + \tau_s^P$ .

Using the chain rule for partial derivatives leads to

$$\begin{aligned} \left[ \frac{\partial Q_{T-v,s}}{\partial e_v} \right]_{\mathbf{U}^v, \mathbf{C}} &= \left[ \frac{\partial Q_{T-v,s}}{\partial e_v} \right]_{\mathbf{U}^v, \mathbf{C}, T, Tv, p} + \left[ \frac{\partial Q_{T-v,s}}{\partial T} \right]_{\mathbf{U}^v, \mathbf{C}, T, p} \left[ \frac{\partial T}{\partial e_v} \right]_{\mathbf{U}^v, \mathbf{C}} \\ &\quad + \left[ \frac{\partial Q_{T-v,s}}{\partial T_v} \right]_{\mathbf{U}^v, \mathbf{C}, T, p} \left[ \frac{\partial T_v}{\partial e_v} \right]_{\mathbf{U}^v, \mathbf{C}} \\ &\quad + \left[ \frac{\partial Q_{T-v,s}}{\partial p} \right]_{\mathbf{U}^v, \mathbf{C}, T, p} \left[ \frac{\partial p}{\partial e_v} \right]_{\mathbf{U}^v, \mathbf{C}} \end{aligned} \quad (\text{C.22})$$

$$\text{Derivation of } \left[ \frac{\partial Q_{T-v_s}}{\partial e_v} \right]_{U^g, c, T, T_v, p}$$

From equation (C.21), one may deduce that

$$\left[ \frac{\partial Q_{T-v_s}}{\partial e_v} \right] = 0. \quad (\text{C.23})$$

$$\text{Derivation of } \left[ \frac{\partial Q_{T-v_s}}{\partial T} \right]_{U^g, c, T_v, p}$$

$$\left[ \frac{\partial Q_{T-v_s}}{\partial T} \right] = \frac{\rho c_s}{\tau_{vs}^2} \left\{ \tau_{vs} \left( \frac{\partial e_{vs}^*}{\partial T} \right) - (e_{vs}^* - e_{vs}) \left( \frac{\partial \tau_{vs}}{\partial T} \right) \right\} \quad (\text{C.24})$$

where

$$\left( \frac{\partial e_{vs}^*}{\partial T} \right) = \frac{e_{vs}^{*2} \exp(\theta_{vs}/T)}{R_s T^2} \quad (\text{C.25})$$

Knowing that

$$\begin{cases} < \tau_s^{L-T} > = \frac{\sum_l \chi_l}{\sum_l \chi_l \tau_{sl}^{L-T}} \\ \tau_{sl}^{L-T} = \frac{101300}{p} \exp(A_{sl}(T^{-1/3} - 0.015\mu_{sl}^{1/4}) - 18.42) \end{cases} \quad (\text{C.26})$$

and

$$\begin{cases} \tau_s^P = \frac{1}{\xi_s \sigma_v X_s} \\ \xi_s = \sqrt{8RT/\pi M_s} \\ \sigma_v = 10^{-21}(50,000/T)^2 \end{cases} \quad (\text{C.27})$$

It results in

$$\begin{cases} \left( \frac{\partial \tau_{vs}}{\partial T} \right) = -\frac{\bar{A}_{sl} T^{-4/3}}{3} < \tau_s^{L-T} > + \frac{3}{2T} \tau_s^P \\ \bar{A}_{sl} = \frac{\sum_l \chi_l A_{sl}}{\sum_l \chi_l} \end{cases} \quad (\text{C.28})$$

Substituting the equations (C.25) and (C.28) into the equation (C.24) yields to

$$\left[ \frac{\partial Q_{T-v,s}}{\partial T} \right] = \frac{\rho c_s e_{vs}^2 \exp(\theta_{vs}/T)}{R_s T \tau_{vs}} + \left( \frac{\bar{A}_{si} T^{-4/3}}{3} < \tau_s^{L-T} > - \frac{3}{2T} \tau_s^P \right) \frac{Q_{T-v,s}}{\tau_{vs}} \quad (\text{C.29})$$

**Derivation of  $\left[ \frac{\partial T}{\partial e_v} \right]_{U^s, c}$**

Recall that the total internal energy may be written as

$$e = \bar{c}_v T + \sum_{l=1}^{N_s} c_l h_l^o + e_v + \frac{1}{2} \mathbf{v}^2. \quad (\text{C.30})$$

By taking the derivative with respect to  $e_v$ , one obtains

$$\left[ \frac{\partial T}{\partial e_v} \right] = - \frac{1}{\bar{c}_v}. \quad (\text{C.31})$$

**Derivation of  $\left[ \frac{\partial Q_{T-v,s}}{\partial T_v} \right]_{U^s, c, T, p}$**

$$\left[ \frac{\partial Q_{T-v,s}}{\partial T_v} \right] = - \frac{\rho c_s}{\tau_{vs}} \left( \frac{\partial e_{vs}}{\partial T_v} \right), \quad (\text{C.32})$$

and therefore

$$\left[ \frac{\partial Q_{T-v,s}}{\partial T_v} \right] = - \frac{\rho c_s e_{vs}^2 \exp(\theta_{vs}/T_v)}{\tau_{vs} R_s T_v^2}. \quad (\text{C.33})$$

**Derivation of  $\left[ \frac{\partial T_v}{\partial e_v} \right]_{U^s, c}$**

The vibrational energy for a gas mixture is defined as

$$\begin{aligned} e_v &= \sum_{l=3}^{N_s} c_l e_{vl} \\ &= \sum_{l=3}^{N_s} c_l \frac{R_l \theta_{vl}}{\exp(\theta_{vl}/T_v) - 1} \end{aligned} \quad (\text{C.34})$$

By taking the derivative with respect to  $T_v$  of the above equation, one finds

$$\left[ \frac{\partial T_v}{\partial e_v} \right] = \left\{ \sum_{l=3}^{N_s} \frac{c_l e_{vl}^2 \exp(\theta_{vl}/T_v)}{R_l T_v^2} \right\}^{-1} \quad (\text{C.35})$$

**Derivation of**  $\left[ \frac{\partial Q_{T-v,s}}{\partial p} \right]_{U^s, c, T, T_v}$

$$\left[ \frac{\partial Q_{T-v,s}}{\partial p} \right] = -\frac{Q_{T-v,s}}{\tau_{vs}} \left( \frac{\partial \tau_s^{L-T}}{\partial p} \right). \quad (\text{C.36})$$

From the equation (C.26), we have

$$\left( \frac{\partial \tau_s^{L-T}}{\partial p} \right) = -\frac{\langle \tau_s^{L-T} \rangle}{p}, \quad (\text{C.37})$$

and the equation (C.36) becomes

$$\left[ \frac{\partial Q_{T-v,s}}{\partial p} \right] = \frac{\langle \tau_s^{L-T} \rangle}{p \tau_{vs}} Q_{T-v,s}. \quad (\text{C.38})$$

**Derivation of**  $\left[ \frac{\partial p}{\partial e_v} \right]_{U^s, c}$

Writing the total internal energy in terms of the pressure variable results in

$$e = (\gamma - 1) \frac{p}{\rho} + \sum_{l=1}^{N_s} c_l h_l^o + e_v + \frac{1}{2} \mathbf{v}^2. \quad (\text{C.39})$$

Then differentiating this expression for  $p$  with respect to  $e_v$  yields

$$\left[ \frac{\partial p}{\partial e_v} \right] = -(\gamma - 1) \rho. \quad (\text{C.40})$$

### 3.2.2 Chemical-Vibrational Exchange Contribution

$$\left[ \frac{\partial S_{c-v}}{\partial e_v} \right]_{U^s, c} = \sum_{s=3}^{N_s} \left[ \frac{\partial S_{c-v,s}}{\partial e_v} \right]_{U^s, c}, \quad (\text{C.41})$$

where

$$\begin{cases} S_{c-v,s}(\mathcal{C}, T, T_v, p) &= S_s^c(\mathcal{C}, T, T_v) e_{vs}(T_v) \\ S_s^c(\mathcal{C}, T, T_v) &= \mathcal{M}_s \sum_{r=1}^{N_r} (\nu_{sr}'' - \nu_{sr}') R_r(\mathcal{C}, T, T_v) \end{cases} \quad (C.42)$$

Using the chain rule for partial derivatives, one may write

$$\begin{aligned} \left[ \frac{\partial S_{c-v,s}}{\partial e_v} \right]_{U^s, \mathcal{C}} &= \left[ \frac{\partial S_{c-v,s}}{\partial e_v} \right]_{U^s, \mathcal{C}, T, T_v} + \left[ \frac{\partial S_{c-v,s}}{\partial T} \right]_{U^s, \mathcal{C}, T_v} \left[ \frac{\partial T}{\partial e_v} \right]_{U^s, \mathcal{C}} \\ &\quad + \left[ \frac{\partial S_{c-v,s}}{\partial T_v} \right]_{U^s, \mathcal{C}, T} \left[ \frac{\partial T_v}{\partial e_v} \right]_{U^s, \mathcal{C}} \end{aligned} \quad (C.43)$$

**Derivation of**  $\left[ \frac{\partial S_{c-v,s}}{\partial e_v} \right]_{U^s, \mathcal{C}, T, T_v}$

From the equation (C.42), we deduce that

$$\left[ \frac{\partial S_{c-v,s}}{\partial e_v} \right] = 0. \quad (C.44)$$

**Derivation of**  $\left[ \frac{\partial S_{c-v,s}}{\partial T} \right]_{U^s, \mathcal{C}, T_v}$

Introducing the derivative with respect to the rate controlling temperature  $T_a$  as an intermediate step gives

$$\left[ \frac{\partial S_{c-v,s}}{\partial T} \right] = e_{vs} \left( \frac{\partial S_s^c}{\partial T_a} \right) \left( \frac{\partial T_a}{\partial T} \right), \quad (C.45)$$

where all partial derivatives of the RHS were already derived in Section 3.1.

**Derivation of**  $\left[ \frac{\partial S_{c-v,s}}{\partial T_v} \right]_{U^s, \mathcal{C}, T}$

Using the same approach as in the previous derivation yields to

$$\left[ \frac{\partial S_{c-v,s}}{\partial T_v} \right] = e_{vs} \left( \frac{\partial S_s^c}{\partial T_a} \right) \left( \frac{\partial T_a}{\partial T_v} \right) + S_s^c \left( \frac{\partial e_{vs}}{\partial T_v} \right), \quad (C.46)$$

where the first two-derivatives of the RHS were already derived in Section 3.1 and the third derivative  $(\partial e_{vs}/\partial T_v)$  is given by the equation (C.33).

# Bibliography

- [1] R. Abgrall, J.-A. Désidéri, R. Glowinski, M. Mallet, and J. Péraux, editors. *Hypersonic Flows for Reentry Problems*, volume 3. Springer-Verlag, 1991.
- [2] D. Ait-Ali-Yahia and W. G. Habashi. A directionally-adaptive finite element method for hypersonic thermo-chemical nonequilibrium flows. In *15th International Conference on Numerical Methods in Fluid Dynamics*, Monterey, CA, USA, 1996.
- [3] D. Ait-Ali-Yahia and W. G. Habashi. A segregated finite element method for thermo-chemical nonequilibrium hypersonic flows on adaptive grids. *AIAA Paper 97-0981*, 1997.
- [4] D. Ait-Ali-Yahia, W. G. Habashi, and G. S. Baruzzi. A finite element method for hypersonic reacting flows. In Dhaubhadel, Habashi, and Engelman, editors, *Advances in Finite Element Analysis in Fluid Dynamics, FED-Vol. 200*, pages 11–19. ASME, 1994.
- [5] D. Ait-Ali-Yahia, W. G. Habashi, A. Tam, M.-G. Vallet, and M. Fortin. A directionally adaptive methodology using an edge-based error estimate on quadrilateral grids. *Int. J. Num. Meths. Fluids*, 23:673–690, 1996.

- [6] D. Ait-Ali-Yahia, W. G. Habashi, A. Tam, M.-G. Vallet, and M. Fortin. A directionally-adaptive finite element method for high-speed flows. *AIAA Paper 96-2553*, 1996.
- [7] D. Ait-Ali-Yahia, A. Tam, W. G. Habashi, M.-G. Vallet, and M. Fortin. An adaptive moving-node scheme for compressible flows on structured meshes. In *6th International Symposium on Computational Fluid Dynamics*, Lake Tahoe, USA, September 1995.
- [8] P. Alavilli, C. Lacor, and C. Hirsch. New high-order semi-implicit Runge-Kutta for computing transient nonequilibrium hypersonic flow. *AIAA Paper 95-2007*, 1995.
- [9] J. D. Anderson. *Hypersonic and High Temperature Gas Dynamics*. McGraw-Hill Series in Aeronautical and Aerospace Engineering, New York, 1989.
- [10] A. Arnone. Multigrid methods for turbomachinery Navier-Stokes calculations. In W. Habashi, editor, *Solution Techniques for Large-Scale CFD Problems*, pages 294–332, 1995.
- [11] B. Aupoix. An introduction to real gas effects. In *Special Course on Aerothermodynamics of Hypersonic Vehicles*, number AGARD-R-761, pages 3–1–3–56, 1990.
- [12] I. Babuška and A. Miller. The post-processing approach in the finite element method - Part 1: Calculation of displacements, stresses and other high derivatives of the displacements. *Int. J. Num. Meth. Engng*, 20:1085–1109, 1984.
- [13] I. Babuška and A. Miller. The post-processing approach in the finite element method - Part 2: The calculation of stress intensity factors. *Int. J. Num. Meth. Engng*, 20:1111–1129, 1984.

- [14] I. Babuška and A. Miller. The post-processing approach in the finite element method - Part 3: A posteriori error estimates and adaptive mesh selection. *Int. J. Num. Meth. Engng*, 20:2311–2324, 1984.
- [15] I. Babuška, O. C. Zienkiewicz, J. Gago, and A. de Oliveira, editors. *Accuracy Estimates and Adaptive Refinements in Finite Element Computations*, London, 1986. John Wiley & Sons.
- [16] R. E. Bank and A. Weiser. Some a posteriori error estimator for elliptic partial differential equations. *Math. of Comp.*, 44:283–301, 1985.
- [17] G. S. Baruzzi, W. G. Habashi, G. Guèvremont, and M. M. Hafez. A second order finite element method for the solution of the transonic Euler and Navier-Stokes equations. *Int. J. Num. Meths. Fluids*, 20(8/9):671–693, 1995.
- [18] A. L. Brooks and T. J. R. Hughes. Streamline upwind Petrov-Galerkin formulations for convection dominated flows with particular emphasis on the incompressible Navier-Stokes equations. *Comp. Meth. Appl. Mech. and Engng*, 32:199–259, 1982.
- [19] T. R. A. Bussing and E. M. Murman. Finite volume method for the calculation of compressible chemically reacting flows. *AIAA Paper 85-0331*, 1985.
- [20] G. V. Candler. *The Computation of Weakly Ionized Hypersonic Flows in Thermo-Chemical Nonequilibrium*. PhD thesis, Department of Aeronautics and Astronautics, Stanford University, CA, USA, 1988.
- [21] G. V. Candler. On the computation of shock shapes in nonequilibrium hypersonic flows. *AIAA Paper 89-0312*, 1989.
- [22] G. V. Candler and R. W. MacCormack. The computation of hypersonic flows in chemical and thermal nonequilibrium. *AIAA Paper 88-0511*, 1988.

- [23] G. V. Candler and R. W. MacCormack. The computation of hypersonic flows in chemical and thermal nonequilibrium. In *The Third National Aero-Space Plane Technology Symposium*, NASA Ames, Moffet Field, Mountain View, CA, USA, 1988.
- [24] F. Chalot, T. J. R. Hughes, Z. Johan, and F. Shakib. 6.1-1 test case. In *Workshop on Hypersonic Flows for Reentry Problems*, 1990.
- [25] P. Cinnella. *Flux-Split for Flows with Non-Equilibrium Chemistry and Thermodynamics*. PhD thesis, Aerospace Engineering, Virginia Polytechnic Institute, Blacksburg, VA, USA, 1989.
- [26] P. Cinnella and B. Grossman. Upwind techniques for flows with multiple translational temperatures. *AIAA Paper 90-1660*, 1990.
- [27] P. Colella and P. M. Glaz. Efficient solution algorithms for the Riemann problems for real gases. *J. Comp. Phy.*, 59:264–289, 1985.
- [28] R. L. Davis and J. F. Dannenhoffer. 3-D adaptive grid-embedding Euler technique. *AIAA Paper 93-0330*, 1993.
- [29] L. Demkowicz, J. T. Oden, and W. Rachowicz. A new finite element method for solving compressible Navier-Stokes equations based on an operator splitting method and  $h-p$  adaptivity. *Comp. Meth. Appl. Mech. and Engng*, 84:257–326, 1990.
- [30] J. Désidéri. The computational over unstructured grids of inviscid hypersonic reactive flows by upwind finite-volume schemes. In T. K. S. Murthy, editor, *Computational Methods in Hypersonic Aerodynamics*, pages 387–446. Kluwer Academic Publishers, 1991.

- [31] J. Désidéri, N. Glinsky, E. Hettema, J. Périaux, and B. Stoufflet. Hypersonic reactive flow computations around space-shuttle-like geometries by 3-D upwind finite elements. *AIAA Paper 89-0657*, 1989.
- [32] J. Dompiere, M.-G. Vallet, M. Fortin, W. G. Habashi, D. Ait-Ali-Yahia, and S. Boivin. Edge based mesh adaptation for cfd. In *International Conference on Numerical Methods for the Euler and Navier-Stokes Equations*, 1995.
- [33] N. Drouin, F. Coron, D. L. H. Hollanders, and G. Moules. Calculations of non-equilibrium real gas flows with the finite-volume Euler/Navier-Stokes solver flu3neqv. *AIAA Paper 94-0761*, 1994.
- [34] B. Dubroca. An extension of Roe's Riemann solver applied to reactive viscous flows for the computation of laminar hypersonic wake. In C. Taylor, editor, *Numerical Methods in Laminar and Turbulent Flows*, pages 1168–1179, Swansea, UK, 1993.
- [35] L. C. Dutto, W. G. Habashi, M. P. Robichaud, and M. Fortin. A method for finite element parallel viscous compressible flow calculations. *Int. J. Num. Meths. Fluids*, 19:275–294, 1994.
- [36] L. C. Dutto, W. G. Habashi, M. P. Robichaud, and M. Fortin. Parallelizable block diagonal preconditioners for the compressible Navier-Stokes equations. *Comp. Meth. Appl. Mech. and Engng*, 117:15–47, 1994.
- [37] S. Eberhardt and K. Brown. A shock capturing technique for hypersonic, chemically relaxing flows. *AIAA Paper 86-0231*, 1986.
- [38] S. Eberhardt and S. Imlay. A diagonal implicit scheme for computing flows with finite-rate chemistry. *AIAA Paper 90-1577*, 1990.

- [39] J. R. Edwards. A diagonal implicit/nonlinear multigrid algorithm for computing hypersonic, chemically-reacting viscous flows. *AIAA Paper 94-0762*, 1994.
- [40] C. A. J. Fletcher. A primitive variable finite element formulation for inviscid compressible flow. *J. Comp. Phy.*, 33:301–312, 1979.
- [41] M. Fortin, W. G. Habashi, D. Ait-Ali-Yahia, S. Boivin, Y. Bourgault, J. Dompiere, and M.-G. Vallet. Anisotropic mesh optimization: Towards a solver-independent and mesh-independent cfd. In *Lecture Notes for VKI Short Course*, Montreal, August 1996.
- [42] M. Fortin, M.-G. Vallet, D. Poirier, and W. G. Habashi. Error estimation and directionally adaptive meshing. *AIAA Paper 94-2221*, 1994.
- [43] P. Glaister. An approximate linearised Riemann solver for the Euler equations for real gases. *J. Comp. Phy.*, 74:382–408, 1988.
- [44] N. Glinsky. *Simulation Numérique d'Écoulements Hypersoniques Réactifs Hors-Équilibre Chimique*. PhD thesis, Université de Nice-Sophia Antipolis, France, 1990.
- [45] A. P. Gnoffo. Hypersonic flows over biconics using a Variable-Effective-Gamma Parabolized-Navier-Stokes code. *AIAA Paper 83-1666*, 1983.
- [46] A. P. Gnoffo. Point-implicit relaxation strategies for viscous hypersonic flows. In T. K. S. Murthy, editor, *Computational Methods in Hypersonic Aerodynamics*, pages 115–152. Kluwer Academic Publishers, 1991.
- [47] P. A. Gnoffo. A finite-volume, adaptive grid algorithm applied to planetary entry flowfields. *AIAA J.*, 21(9):1249–1254, 1983.

- [48] S. Godunov. Finite-difference method for numerical computation of discontinuous solutions of the equations of fluid dynamics. *Matematika. Sbornik.*, 47(3):271–306, 1959.
- [49] T. Gokcen. *Computation of Hypersonic Low Density Flows with Thermo-Chemical Nonequilibrium*. PhD thesis, Department of Aeronautics and Astronautics, Stanford University, CA, USA, 1989.
- [50] B. Grossman and G. Moretti. Time-dependent computation of transonic flow. *AIAA Paper 70-1322*, 1970.
- [51] B. Grossman and R. Walters. Analysis of flux-split algorithms for Euler's equations with real gases. *AIAA J.*, 27(5):524–531, 1989.
- [52] W. Gui and I. Babuška. The  $h$ ,  $p$  and  $h-p$  version of the finite element method in one dimension. Part III: The adaptive  $h-p$  version. *Numerische Mathematik*, 48:658–683, 1986.
- [53] W. Gui and I. Babuška. The  $h$ ,  $p$  and  $h-p$  version of the finite element method in one dimension. Part I: The error analysis of the  $p$  version. *Numerische Mathematik*, 48:557–612, 1986.
- [54] W. Gui and I. Babuška. The  $h$ ,  $p$  and  $h-p$  version of the finite element method in one dimension. Part II: The error analysis of the  $h$  and  $h-p$  version. *Numerische Mathematik*, 48:613–657, 1986.
- [55] G. W. Habashi and M. Fortin. Anisotropic mesh adaptation: Towards a grid-independent, scheme-independent and user-independent cfd. In *Basel World CFD User Days 1996, Third World Conference in Applied Computational Fluid Dynamics*, pages 13.1–13.4, 1996.

- [56] J. Häuser, J. Muylaert, H. Wong, and W. Berry. Computational aerothermodynamics for 2D and 3D space vehicles. In T. K. S. Murthy, editor, *Computational Methods in Hypersonic Aerodynamics*, pages 447–490. Kluwer Academic Publishers, 1991.
- [57] D. F. Hawken, J. J. Gottlieb, and J. S. Hansen. Review of some adaptive node-movement techniques in finite-element and finite-difference solutions of partial differential equations. *J. Comp. Phy.*, 95(2):254–302, 1991.
- [58] W. D. Hayes and R. F. Probstein. *Hypersonic Flow Theory*. Academic Press, New York, 1959.
- [59] C. Hirsh. *Numerical Computation of Internal and External Flows. Volume 2: Computational Methods for Inviscid and Viscous Flows*. John Wiley & Sons, 1990.
- [60] H. G. Hornung. Non-equilibrium dissociating nitrogen flow over spheres and cylinders. *J. Fluid Mech.*, 53(1):149–176, 1972.
- [61] T. J. R. Hughes. Recent progress in the development and understanding of SUPG methods with special reference to the compressible euler and Navier-stokes equations. *Int. J. Num. Meths. Fluids*, 7:1261–1275, 1987.
- [62] T. J. R. Hughes and T. E. Tezduyar. Finite element method for first-order hyperbolic systems with particular emphasis on the compressible Euler equations. *Comp. Meth. Appl. Mech. and Engng*, 45:217–284, 1984.
- [63] S. T. Imlay, D. W. Roberts, M. Soertrisno, and S. Eberhardt. Nonequilibrium thermochemical calculations using a diagonal implicit scheme. *AIAA Paper 91-0468*, 1991.
- [64] A. Jameson. Solution of the Euler equations by a multi-grid method. *Appl. Math. Comp.*, 13:327–356, 1983.

- [65] A. Jameson. Artificial diffusion, upwind biasing, limiters and their effect on accuracy and multigrid convergence in transonic and hypersonic flows. *AIAA Paper*, 93-3359, 1993.
- [66] A. Jameson and D. Mavriplis. Finite volume solution of two-dimensional Euler equations on a regular triangular mesh. *AIAA J.*, 24(4):611–618, 1986.
- [67] A. Jameson, W. Schmidt, and E. Turkel. Numerical solution of the Euler equations by finite volume methods using Runge-Kutta time stepping schemes. *AIAA Paper* 81-1259, 1981.
- [68] B.-N. Jiang and G. F. Carey. Least-squares finite element methods for compressible euler equations. *Int. J. Num. Meths. Fluids*, 10:557–568, 1990.
- [69] S. Jonas, H.-H. Fruhauf, and O. Knab. Fully coupled approach to the calculation of nonequilibrium hypersonic flows using a Godunov-type method. In C. Hirsh, editor, *Computational Fluid Dynamics '92*, volume 1, pages 305–314, 1992.
- [70] Y. G. Kallinderis and J. R. Baron. Adaptation methods for a new Navier-Stokes algorithm. *AIAA J.*, 27(1):37–43, 1989.
- [71] S. W. Kang and M. G. Dunn. Theoretical and measured electron density distributions for the RAM vehicle at high altitudes. *AIAA Paper* 72-689, 1972.
- [72] O. Knab, T. H. Gogel, H.-H. Fruhauf, and E. W. Messerschmid. CVCV-model validation by means of radiative heating calculations. *AIAA Paper* 95-0623, 1995.
- [73] O. Knab and S. J. H.-H. Fruhauf. Multiple temperature descriptions of reaction rate constants with regard to consistent chemical-vibrational coupling. *AIAA Paper* 92-2947, 1992.

- [74] R. Körnhuber and R. Roitzsch. On adaptive grid refinement in the presence of internal or boundary layers. *Impact Comp. Sc. Engng*, 2:40–72, 1990.
- [75] M. H. Lallemand, H. Steve, and A. Dervieux. Unstructured multigriding by volume agglomeration: Current status. *Comp. and Fluids*, 21:397–433, 1992.
- [76] J. H. Lee. Basic governing equations for the flight regimes of aeroassisted orbital transfer vehicles. In *Thermal Design of Aeroassisted Orbital Transfer Vehicles*, volume 96, pages 3–53. Progress in Aeronautics and Astronautics, 1985.
- [77] D. Lefebvre and J. Peraire. Finite element least squares solution of the euler equations using linear and quadratic approximations. *Int. J. Comp. Fluid Dyn.*, 1:1–23, 1993.
- [78] C. P. Li. Time-dependent solutions of nonequilibrium dissociating flow past a blunt body. *J. Spacecraft and Rockets*, 8(7):812–814, 1971.
- [79] R. Löhner. An adaptive finite element scheme for transient problem in CFD. *Comp. Meth. Appl. Mech. and Engng*, 61:323–338, 1987.
- [80] R. Löhner. Adaptive remeshing for transient problems. *Comp. Meth. Appl. Mech. and Engng*, 75:195–214, 1989.
- [81] R. Löhner. Finite element methods in CFD: Grid generation, adaptivity and parallelization. Technical Report 787 NATO, AGARD, 1992.
- [82] R. Löhner, K. Morgan, and J. Peraire. A simple extension to multidimensional problems of the artificial viscosity due to Lapidus. *Comm. Appl. Numer. Meth.*, 1:141–147, 1985.
- [83] R. Löhner, K. Morgan, and O. C. Zienkiewicz. Adaptive grid refinement for the compressible Euler equation. In I. Babuška, O. C. Zienkiewicz, J. Gago, and A. Oliveira,

editors, *Accuracy Estimates and Adaptive Refinements in Finite Element Computation*. John Wiley & Sons, 1986.

- [84] R. W. MacCormack. Current status of the numerical solutions of the Navier-Stokes equations. *AIAA Paper 85-0032*, 1985.
- [85] R. Magnus and H. Yashihara. Inviscid transonic flow over airfoils. *AIAA J.*, 8:2157–2162, 1970.
- [86] D. J. Mavriplis. Three-dimensional unstructured multigrid for the Euler equations. *AIAA J.*, 30(7):1753–1761, 1992.
- [87] R. C. Millikan and D. R. White. Systematics of vibrational relaxation. *J. Chem. Phys.*, 39(12):3209–3213, 1963.
- [88] J. N. Moss and G. A. Bird. Direct simulation of transitional flow for hypersonic reentry conditions. *AIAA Paper 84-0233*, 1984.
- [89] K. Nakahashi and G. S. Deiwert. Self-adaptive grid method with application to airfoil flow. *AIAA J.*, 25(4):513–520, 1987.
- [90] R. H. Ni. A multiple-grid scheme for solving the Euler equations. *AIAA J.*, 20(11):1565–1571, 1982.
- [91] J. T. Oden and L. Demkowicz. A survey of adaptive finite element methods in computational mechanics. In A. K. Noor and J. T. Oden, editors, *State-of-the-Art Surveys on Computational Mechanics*, pages 441–467. ASME, 1989.
- [92] J. T. Oden and L. Demkowicz.  $h-p$  adaptive finite element methods in computational fluid dynamics. *Comp. Meth. Appl. Mech. and Engng*, 89:11–40, 1991.

- [93] J. T. Oden, L. Demkowicz, W. Rachowicz, and W. Westermann. Toward a universal  $h-p$  adaptive finite element strategy, Part 2. A posteriori error estimation. *Comp. Meth. Appl. Mech. and Engng*, 77:113–180, 1989.
- [94] J. T. Oden, T. Liszka, and W. Wu. An  $h-p$  adaptive finite element method for incompressible viscous flows. In *The Mathematics of Finite Elements and Applications VII*. Academic Press, 1991.
- [95] J. T. Oden, T. Strouboulis, and P. Devloo. Adaptive finite element methods for high-speed compressible flows. *Int. J. Num. Meths. Fluids*, 7:1211–1228, 1987.
- [96] J. T. Oden, T. Strouboulis, P. Devloo, and M. Howe. Recent advances in error estimation and adaptive improvement of finite element calculations. In I. Babuška, O. C. Zienkiewicz, J. Gago, and A. Oliveira, editors, *Accuracy Estimates and Adaptive Refinements in Finite Element Computation*. John Wiley & Sons, 1986.
- [97] J. T. Oden and W. Wu. An  $hp$  adaptive strategy for finite element approximations of the Navier-Stokes equations. *Int. J. Num. Meths. Fluids*, 7:831–851, 1995.
- [98] E. Onate, F. Quintana, and J. Miquel. Numerical simulation of hypersonic flow over a double ellipse using a Taylor-Galerkin finite element formulation with adaptive grids. In *Workshop on Hypersonic Flows for Reentry Problems*, volume 2, pages 635–653, 1990.
- [99] B. Palmerio. A two-dimensional FEM adaptive moving-node method for steady Euler flow simulation. *Comp. Meth. Appl. Mech. and Engng*, 71:315–340, 1988.
- [100] C. Park. On convergence of computation of chemically reacting flows. *AIAA Paper 85-0247*, 1985.

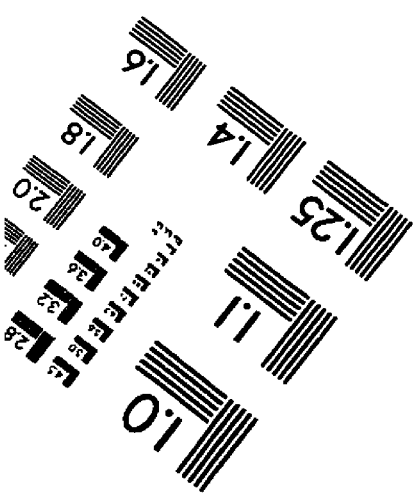
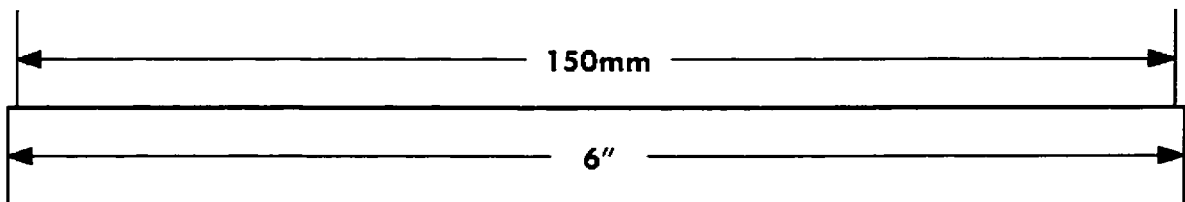
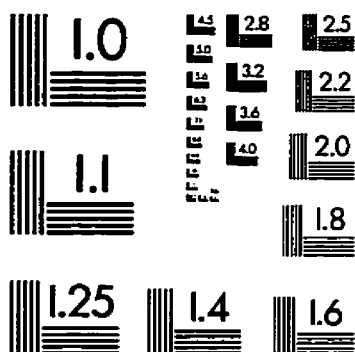
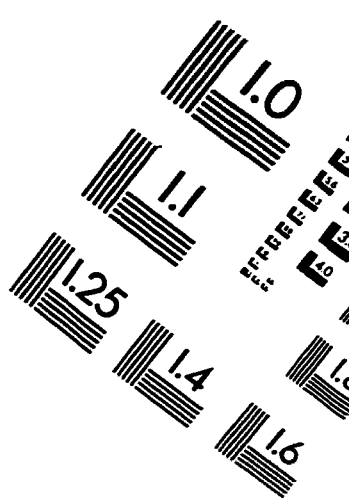
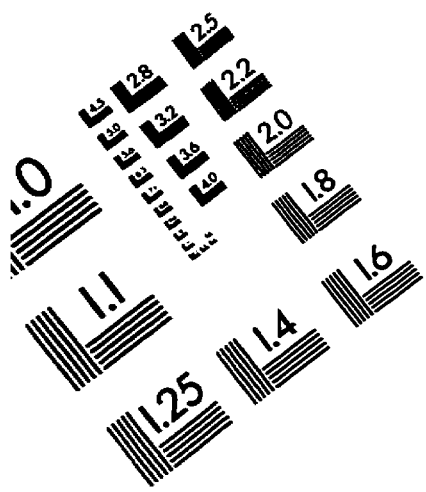
- [101] C. Park. Assessment of two-temperature kinetic model for dissociating and weakly-ionizing nitrogen. *J. Thermo. Heat Trans.*, 2(1):8–16, 1989.
- [102] C. Park. Assessment of two-temperature kinetic model for ionizing air. *J. Thermo. Heat Trans.*, 3(13):233–244, 1989.
- [103] C. Park. *Nonequilibrium Hypersonic Aerothermodynamics*. John Wiley & Sons, New York, 1990.
- [104] C. Park and S. Yoon. Fully coupled implicit method for thermo-chemical nonequilibrium air at suborbital flight speeds. *J. Spacecraft*, 28(1):31–39, 1991.
- [105] C. Park and S. Yoon. Calculations of real-gas effects on blunt-body trim angles. *AIAA J.*, 30(4):999–1007, 1992.
- [106] M. F. Peeters, W. G. Habashi, B. Q. Nguyen, and P. L. Kottiuga. Finite element solutions of the Navier-Stokes equations for compressible internal flows. *J. Prop. Power*, 8(1):192–198, 1992.
- [107] J. Peraire, J. Perió, and K. Morgan. Adaptive remeshing for three-dimensional compressible flow computations. *J. Comp. Phy.*, 103:269–285, 1992.
- [108] J. Peraire, M. Vahdati, K. Morgan, and O. C. Zienkiewicz. Adaptive remeshing for compressible flow computations. *J. Comp. Phy.*, 72:449–466, 1987.
- [109] W. Rachowicz, J. T. Oden, and L. Demkowicz. Toward a universal  $h-p$  adaptive finite element strategy, Part 3. Design of  $h-p$  meshes. *Comp. Meth. Appl. Mech. and Engng*, 77:181–212, 1989.
- [110] P. Roe. Approximated riemann solvers, parameter vectors and difference scheme. *J. Comp. Phy.*, 43:357–372, 1981.

- [111] P. L. Roe. Characteristic based schemes for the Euler equations. *Annual Review of Fluid Mechanics*, 18:337–365, 1986.
- [112] Y. Saad and M. H. Schultz. GMRES: A generalized minimal residual algorithm for solving nonsymmetric linear systems. *SIAM J. Sci. Stat. Comput.*, 7(3):856–869, 1986.
- [113] J. S. Shuen and S. Yoon. Numerical study of chemically reacting flows using an lu scheme. *AIAA Paper 88-0436*, 1988.
- [114] J. Steger and R. Warming. Flux-vector splitting of the inviscid gas dynamics equations with applications to finite difference methods. *J. Comp. Phy.*, 40:263–293, 1981.
- [115] A. Tam, W. G. Habashi, D. Ait-Ali-Yahia, M. Robichaud, and M.-G. Vallet. A 3-d adaptive finite element method for turbomachinery. *AIAA Paper 96-2659*, 1996.
- [116] J. L. Thomas, D. L. Dwoyer, and A. Kumar. computational fluid dynamics for hypersonic airbreathing aircraft. In J.-A. Désidéri, R. Glowinski, and J. Périaux, editors, *Hypersonic Flows for Reentry Problems*, volume 1, pages 55–71. Springer-Verlag, 1990.
- [117] H. S. Tsien. Similarity laws of hypersonic flows. *J. Math. and Phy.*, 25:247–251, 1946.
- [118] W. W. Tworzydlo, J. T. Oden, and E. A. Thornton. Adaptive implicit/explicit finite element method for compressible viscous flows. *Comp. Meth. Appl. Mech. and Engng*, 95:397–440, 1992.
- [119] M.-G. Vallet. *Génération de maillages éléments finis anisotropes et adaptatifs*. PhD thesis, Université Pierre et Marie Curie, Paris VI, 1992.

- [120] B. Van Leer. Flux-vector splitting for the Euler equations. *Lecture Notes in Physics*, 170, 1982.
- [121] M. Vetter, H. Olivier, and H. Grönig. Flow over double ellipsoid and sphere - Experimental results. In R. Abgrall, J.-A. Désidéri, R. Glowinski, M. Mallet, and J. Périaux, editors, *Hypersonic Flows for Reentry Problems*, volume 3, pages 489–500. Springer-Verlag, 1991.
- [122] W. G. Vincenti and C. H. Kruger. *Introduction to Physical Gas Dynamics*. Krieger Publishing Company, Malabar, FL, 1986.
- [123] M. Vinkour and Y. Liu. Equilibrium gas flow computations. II. An analysis of numerical formulations of conservation laws. *AIAA Paper 88-0127*, 1988.
- [124] Y. Wada, H. Kubota, S. Ogawa, and T. Ishiguro. A generalized Roe's approximate Riemann solver for chemically flows. *AIAA Paper 89-0202*, 1989.
- [125] Y. Wada and M. S. Liou. A flux-splitting scheme with high-resolution and robustness for discontinuities. *AIAA Paper 94-0083*, 1994.
- [126] G. D. Walberg. A review of aero-assisted orbit transfer. *AIAA Paper 82-1378*, 1982.
- [127] G. D. Walberg. Aero-assisted orbit transfer window opens on missions. volume 21, pages 36–43. Progress in Aeronautics and Astronautics, 1983.
- [128] R. W. Walters, P. Cinnella, D. C. Slack, and D. Halt. Characteristic-based algorithms for flows in thermo-chemical nonequilibrium. *AIAA J.*, 30(5):1304–1313, 1992.
- [129] R. M. Williams. National aero-space plane. *Aerospace America*, pages 18–22, November 1987.
- [130] S. Yoon and D. Kwak. Artificial dissipation models for hypersonic external flow. *AIAA Paper 88-3708*, 1988.

- [131] D. Zeitoun, E. Schall, Y. Burtschell, and M. C. Druguet. Vibration-dissociation coupling in nonequilibrium hypersonic viscous flows. *AIAA J.*, 33(1):79–84, 1995.
- [132] M. W. Zemansky and R. H. Dittman. *Heat and Thermodynamics*. McGraw-Hill Book Company, New York, 1979.
- [133] J. Z. Zhu and O. C. Zienkiewicz. Adaptive techniques in the finite element method. *Comm. Appl. Numer. Meth.*, 4:197–204, 1988.
- [134] O. C. Zienkiewicz, Y. C. LIU, and G. G. Huang. Error estimation and adaptivity in flow formulation for forming problems. *Int. J. Num. Meth. Engng*, 25:23–42, 1988.
- [135] O. C. Zienkiewicz and J. Z. Zhu. A simple error estimator and adaptive procedure for practical engineering analysis. *Int. J. Num. Meth. Engng*, 24:337–357, 1987.

IMAGE EVALUATION  
TEST TARGET (QA-3)



APPLIED IMAGE, Inc  
1653 East Main Street  
Rochester, NY 14609 USA  
Phone: 716/482-0300  
Fax: 716/288-5989

© 1993, Applied Image, Inc., All Rights Reserved

